Acoustic Imaging for Radiotherapy Dosimetry and Inflammatory Bowel Disease Assessment

by

Yaocai Huang

A dissertation submitted in partial fulfillment
of the requirements for the degree of
Doctor of Philosophy
(Biomedical Engineering)
in the University of Michigan
2026

Doctoral Committee:

Professor Xueding Wang, Co-Chair
Assistant Professor Guan Xu, Co-Chair
Clinical Professor Kyle C. Cuneo
Professor L. Jay Guo
Research Assistant Professor Wei Zhang

Yaocai Huang

hyaocai@umich.edu

ORCID iD: 0009-0002-8597-4834

© Yaocai Huang 2026

Acknowledgements

I would like to sincerely thank my advisors, Dr. Xueding Wang and Dr. Guan Xu, for their guidance and support throughout my PhD. Their insight and demanding standards accelerated my growth and development as a researcher.

I am especially grateful to Dr. Wei Zhang for his mentorship, from hands-on training in the lab to working through many experimental challenges together. I also thank Dr. Issam El Naqa, Dr. Paul L. Carson, and Dr. Peter Higgins for their collaboration and support on this work. My thanks as well to Laura Johnson, Dr. Dale Litzenberg, Dr. Lise Wei, Dr. Christopher Kehayias, Dr. Claire Zhang, and Dr. Ibrahim Oraiqat for their help with experiments and for coordinating resources related to the animal and human studies.

I am thankful to my lab members for the supportive environment and many helpful discussions along the way. Outside the lab, I am grateful to my friends for making these years enjoyable, whether through badminton, board games, skiing, or simply sharing meals together.

This work was supported by the National Cancer Institute (R37CA222215, R01CA266803, P30CA046592, R37CA222829) and the National Institute of Diabetes and Digestive and Kidney Diseases (R01DK125687).

Table of Contents

Acknowledgements ..... **ii**

List of Figures ..... **vi**

List of Tables ..... **xiv**

List of Acronyms ..... **xv**

Abstract ..... **xvii**

Chapter 1 Introduction **1**

1.1 Cancer **2**
1.1.1 Global Cancer Burden 2
1.1.2 Classification of Cancer 3
1.1.3 Approaches to Cancer Treatment 3

1.2 Radiotherapy **5**
1.2.1 Principles of Radiotherapy 6
1.2.2 Evolution of Radiotherapy Delivery Techniques 7
1.2.3 Image Guidance in Modern Radiotherapy 8
1.2.4 Limitations of Current Dosimetry 8

1.3 Ionizing Radiation Acoustic Imaging (iRAI) **9**
1.3.1 Principles of iRAI 9
1.3.2 Development and Current Progress 12
1.3.3 Challenges and Limitations 13
1.3.4 Significance 13

1.4 Photoacoustic Imaging for Assessment of Crohn's Disease **14**
1.4.1 Crohn's Disease 14
1.4.2 Current Diagnostic Limitations in CD 15
1.4.3 Principles of Photoacoustic Imaging 16
1.4.4 Evolution of PA Imaging for Intestinal Applications 18
1.4.5 Endoscopic PA–US Imaging Catheter for Crohn's Disease 19

1.5 Overview of Dissertation Scope **19**

Chapter 2 Volumetric iRAI–US Imaging for Dose-on-Anatomy Visualization **21**

2.1 Introduction **21**

2.2 Materials and Methods **21**
2.2.1 Dual-Modality iRAI–US Imaging System 21
2.2.2 Volumetric Acquisition and Synchronization 23

2.2.3 Characterization of Spatial Resolution....24
2.2.4 Estimation of Dose–anatomy Co-registration Error....24
2.2.5 Respiratory Motion–Mimicking Phantom Study....25
2.2.6 *In Vivo* Rabbit Study....28

2.3 Results....29
2.3.1 Spatial Resolution and Dose–Anatomy Co-Registration Error....29
2.3.2 Temporal Dose Visualization and Motion-Induced Dose–Anatomy Mismatch....30
2.3.3 Dose Accumulation Mapping with US-Guided Motion Correction....33
2.3.4 Quantitative Accuracy of Dose Mapping....35
2.3.5 *In Vivo* Dose-on-Anatomy Imaging in a Rabbit Liver Model....36

2.4 Discussion and Conclusions....37

Chapter 3 Towards Quantitative iRAI Using Transducer Sensitivity Compensation....39

3.1 Introduction....39

3.2 Materials and Methods....40
3.2.1 Transducer Detection Sensitivity Characterization....40
3.2.2 Radiation Beam Evaluation in a Homogeneous Phantom....42
3.2.3 Clinical Treatment Plan Evaluation....43
3.2.4 Data Processing and Quantification....44

3.3 Results....45
3.3.1 Transducer Detection Sensitivity and Correction Factors....45
3.3.2 Radiation Beam Quantification....46
3.3.3 Quantitative Evaluation of a C-Shaped Treatment Plan....48

3.4 Discussion and Conclusions....49

Chapter 4 Volumetric Dose Mapping in an Anthropomorphic Abdominal Phantom....51

4.1 Introduction....51

4.2 Materials and Methods....52
4.2.1 Abdominal Phantom and Experimental Configuration....52
4.2.2 Target Configurations and Treatment Planning....53
4.2.3 Volumetric iRAI Acquisition and Reconstruction....54
4.2.4 Quantitative Evaluation....55

4.3 Results....55
4.3.1 iRAI–CT Co-registered Images....55
4.3.2 Isodose Line Comparisons Between the Treatment Plan and iRAI....60
4.3.3 DVH Comparison Between iRAI and Treatment Plan....61

4.4 Discussion and Conclusions....64

Chapter 5 Translational Photoacoustic–Ultrasound Imaging Catheter for Crohn's Disease....66

5.1 Introduction....66

5.2 Materials and Methods....67
5.2.1 Imaging System Configuration....67
5.2.2 PA–US Balloon Catheter Design....68
5.2.3 Porcine APC-Induced Esophageal Fibrosis Model....70

5.2.4 Spectroscopic PA Imaging 71
5.2.5 *In Vivo* Imaging Protocol in Animal and Human Studies 71
5.2.6 Histological Processing and Evaluation 73
5.2.7 Data Processing 74

5.3 Results 74
5.3.1 Histological Inflammation and Fibrosis in the Pig APC Model 74
5.3.2 Measurement Stability and Reproducibility 75
5.3.3 Structural and Molecular Imaging of the Pig Esophagus Using US and PA 76
5.3.4 Quantitative Molecular Analysis 77
5.3.5 Feasibility of *In Vivo* Imaging in a Human Subject 78

5.4 Discussion and Conclusions 79

Chapter 6 Conclusions and Future Work 81

6.1 Key Findings in iRAI Studies 81
6.1.1 Volumetric iRAI–US Visualization 81
6.1.2 Quantitative iRAI via Sensitivity Compensation 81
6.1.3 Dose Mapping Under Clinical Delivery Scenarios 82

6.2 Key Findings in PA–US Catheter Imaging 82

6.3 Overall Scientific Contributions 82
6.3.1 Contributions to iRAI and Radiotherapy Dosimetry 82
6.3.2 Contributions to Crohn's Disease Diagnosis and Characterization 83

6.4 Limitations 83
6.4.1 Limitations of iRAI Studies 83
6.4.2 Limitations of the Current PA–US Catheter 84

6.5 Future Directions 84
6.5.1 iRAI Future Work 84
6.5.2 Future Directions for Endoscopic PA–US Catheter 84

6.6 Concluding Remarks 85

Bibliography 86

List of Figures

Figure 1.1 Overview of modern radiotherapy workflow and radiation-induced biological mechanisms. Radiotherapy begins with volumetric imaging, typically planning CT, to delineate the target and surrounding OAR. Treatment planning is then performed to optimize dose delivery, followed by irradiation using a LINAC with image-guided radiotherapy for patient positioning verification. At the cellular level, ionizing radiation induces tumor cell death through both direct DNA damage and indirect damage mediated by reactive oxygen species, primarily hydroxyl radicals (·OH). 6
Figure 1.2 Schematic illustration of iRAI for dose visualization during radiotherapy. Pulsed x-ray irradiation deposits energy in tissue, producing a transient temperature rise and thermoelastic expansion that generates acoustic waves. These radiation-induced acoustic signals are detected by an external US transducer and reconstructed to map the spatial distribution of dose deposition. 10
Figure 1.3 Schematic illustration of the gastrointestinal tract highlighting common sites of Crohn's disease involvement, including the esophagus, stomach, terminal ileum, colon, and perianal area. 14
Figure 1.4 Illustration of the PA imaging principle. Optical absorption of pulsed laser energy induces thermoelastic expansion and generates acoustic waves, which are detected by an US probe to reconstruct images of chromophore distribution. 17
Figure 1.5 Relative optical absorption spectra of major chromophores in biological tissue. The vertical dashed lines indicate wavelengths at which different tissue components exhibit relatively strong optical absorption, corresponding to approximately 532 nm, 1220 nm, and 1310 nm. a.u., arbitrary units; Oxy-Hb., oxygenated hemoglobin; Deoxy-Hb., deoxygenated hemoglobin. 18
Figure 2.1 Volumetric acquisition workflow and timing of the dual-modality iRAI–US imaging system. (a) Workflow for volumetric dose-on-anatomy imaging during radiotherapy delivery. Megavoltage radiation pulses from the LINAC generate radiation-induced acoustic signals that are detected by a low-frequency 2D MAT for iRAI dose reconstruction, while a co-registered higher-frequency MAT acquires volumetric US images of anatomical structures. The reconstructed iRAI dose and US images are spatially aligned for dose-on-anatomy visualization. (b) Timing diagram showing coordination between LINAC triggering, iRAI acquisition, interleaved US imaging, and linear motion control. 23

Figure 2.2 Experimental setup and schematic illustrations for the motion-mimicking phantom study. (a) Photograph of the experimental setup showing the soft-tissue phantom mounted on a linear translation stage beneath the LINAC. The iRAI and US 2D MATs were positioned on opposite sides of the phantom for synchronized acquisition during irradiation. The translation stage generated controlled lateral and axial motions. (b) Schematics of the phantom configuration, transducer positioning, and prescribed motion patterns. A lard block embedded in the phantom provided echogenic contrast for US motion tracking. The relative orientation of the X-ray beam, transducers, and motion directions is indicated. (c) Illustration of the temporal relationship between phantom motion and radiation dose deposition. As the phantom moves during irradiation, the relative position between the embedded lard block and the deposited radiation dose changes while the radiation beam remains fixed. 27
Figure 2.3 Volumetric US imaging of the motion phantom at different frame rates. (a–c) Schematic illustrations of dynamic focusing configurations of the US 2D MAT with 16, 9, and 4 focusing positions, respectively. (d–f) Representative x–z cross-sectional US images of the embedded lard block acquired at volumetric frame rates of 2.5, 4, and 10 Hz, corresponding to 16, 9, and 4 focusing positions. Reducing the number of focusing positions increases the volumetric frame rate at the expense of spatial resolution. The scale bar represents 1 cm. 28
Figure 2.4 Volumetric dual-modality imaging of dose-on-anatomy in an *in vivo* rabbit model. (a) Experimental setup for the rabbit study in the radiotherapy treatment room. (b, c) Sagittal and coronal CT views of the rabbit anatomy with the planned dose distribution. 29
Figure 2.5 Spatial resolution of the iRAI and US imaging systems measured using a 0.15-mm-diameter tungsten wire target. (a) Axial and lateral resolutions of the iRAI system as a function of imaging depth. (b) Axial and lateral resolutions of the US system as a function of imaging depth. 30
Figure 2.6 Temporal dose-on-anatomy visualization in motion-mimicking phantom experiments. (a) Time-resolved x–z cross-sectional US images of the tissue-mimicking phantom with an embedded lard block (left), corresponding iRAI dose images (middle), and fused dose-on-anatomy images (right) acquired over a 2 s interval during lateral motion. The phantom moved back and forth along the lateral direction while the radiation beam remained fixed relative to the imaging geometry. (b) Corresponding image sequences acquired during axial motion of the phantom. In both motion scenarios, the US images show continuous displacement of the lard block, whereas the iRAI dose images remain spatially stationary relative to the beam isocenter. The fused images show the relative displacement between the anatomical structure and the deposited dose over time. 33

Figure 2.7 (a) Representative x–z cross-sectional iRAI images of temporal dose accumulation across the beam isocenter without ultrasound-guided motion correction during lateral phantom motion (2 cm/s, 4 cm range). Frames are shown every 0.25 s over 2 s. Pixel intensities are normalized to [0, 1], and green dashed boxes indicate the tracked lard block position. (b) Representative x–z cross-sectional iRAI images of temporal dose accumulation across the beam isocenter with ultrasound-guided motion correction, under the same conditions as in (a). (c) Comparison between radiochromic film measurements and motion-corrected iRAI dose maps for lateral motion (2 cm/s) with ranges of 1–4 cm. Film dose maps were extracted from a 2 cm × 6 cm region. (d) Corresponding comparison for axial motion (1 cm/s) with ranges of 0.5–2 cm. (e) Schematic of the central line used for dose profile extraction. (f, g) Dose profiles along the indicated line for the lateral (c) and axial (d) cases. Dashed lines: film; solid lines: iRAI. All profiles are normalized. 34
Figure 2.8 Volumetric dose-on-anatomy imaging in an *in vivo* rabbit liver model under respiratory motion. (a) Time-resolved multimodality image sequences in sagittal (top row) and coronal (bottom row) views acquired during irradiation. iRAI-derived dose is overlaid in red, US anatomy is shown in yellow, and the CT-derived liver boundary is outlined in light blue. Frames at selected time points during a 20 s delivery period illustrate respiration-induced liver motion and the resulting variation in dose–anatomy alignment. (b) 3D fusion images at the 1st, 10th, and 19th seconds of irradiation, combining CT-based liver segmentation with co-registered US anatomy and iRAI dose. 37
Figure 3.1 Detection sensitivity characterization of the 2D MAT. (a) Block diagram of the experimental setup used to measure the detection sensitivity of the 2D MAT. (b) Schematic of the numerical simulation used to estimate detection sensitivity using the Field II MATLAB toolbox. (c) Frequency spectra of the laser-induced acoustic source (measured by a hydrophone), the transducer measurement, and the deconvolved transducer response. 42
Figure 3.2 Experimental setup for the radiation beam study. (a) Photograph of the x-ray beam imaging experiment conducted in the radiotherapy treatment room. (b) Schematic illustrating x-ray beams delivered along the central axis of the homogeneous phantom at 2 cm intervals from the transducer surface. At a depth of 11 cm, six additional lateral beam positions were delivered with 2 cm spacing. Each beam had a field size of 1 cm × 1 cm. (c) Schematic illustrating x-ray beams with different field sizes (1 × 1 cm^2, 2 × 2 cm^2, 3 × 3 cm^2, 4 × 4 cm^2, and 5 × 5 cm^2) delivered to a fixed depth of 11 cm along the central axis. 43
Figure 3.3 Experimental setup and treatment plan for the clinical phantom study. (a) Photograph of the phantom positioning and irradiation setup in the radiotherapy treatment room. (b–d) Axial

(x–y), coronal (x–z), and sagittal (y–z) cross-sectional views of the treatment plan. Gray regions represent CT images, and the heatmaps indicate the planned dose distribution. 44
Figure 3.4 Detection sensitivity characterization of the 2D MAT. (a) Orthogonal cross-sectional views of simulated and experimentally measured detection sensitivity maps. The color bar represents relative amplitude in arbitrary units (a.u.), ranging from 0 (blue) to 1 (red). The scale bar indicates 5 cm. The orientation of the sensitivity maps follows the indicated coordinate system, where the x-, y-, and z-axes correspond to azimuth, elevation, and depth, respectively. (b) Comparison of DVH curves derived from the simulated and experimental volumetric detection sensitivity maps. 46
Figure 3.5 Quantification of radiation beams before and after sensitivity compensation. (a) A 2 cm × 2 cm radiation beam deposited on radiochromic film. (b) Normalized pseudocolor representation of the film measurement shown in (a). (c) 2D cross-sectional iRAI image of the 2 cm × 2 cm beam. (d) Sensitivity-compensated image corresponding to (c), obtained using correction factors derived from experimentally measured detection sensitivity. (e) Normalized amplitude profiles along the z-direction, comparing experimental and simulated results before compensation. (f) Normalized amplitude values measured at seven positions along the x-direction at a depth of z = 11 cm from the MAT surface. (g, h) Amplitude profiles extracted from compensated iRAI images corresponding to (e) and (f), respectively. 47
Figure 3.6 Reconstructed iRAI images and quantitative evaluation of the C-shaped treatment plan. (a) Axial cross-section of the treatment plan at the mid-plane of the C-shaped dose distribution along the z-axis. (b) Corresponding axial cross-section reconstructed from the iRAI image before sensitivity compensation. (c) Axial cross-section after sensitivity compensation. (d) Sagittal cross-section of the dose distribution from the treatment plan. (e) Corresponding sagittal cross-section reconstructed from the iRAI image before compensation. (f) Sagittal cross-section after compensation. All images were normalized for comparison. (g) Comparison of 80% isodose contours in axial cross-sections from the treatment plan, pre-compensation iRAI reconstruction, and post-compensation reconstruction corresponding to (a–c). (h) Comparison of 80% isodose contours in sagittal cross-sections from the treatment plan, pre-compensation reconstruction, and post-compensation reconstruction corresponding to (d–f). (i) Comparison of DVHs derived from volumetric dose distributions of the treatment plan, pre-compensation iRAI reconstruction, and post-compensation reconstruction. 49
Figure 4.1 Experimental design of the anthropomorphic abdominal phantom study. (a) Photograph of the experimental setup. The phantom was positioned on the treatment couch with the inferior side facing the camera and the anterior surface facing upward. A water-filled balloon was placed between the transducer and the phantom to provide acoustic coupling. Axial, sagittal, and coronal

planes are indicated to define the anatomical reference orientations. (b) Schematic illustration of Lesion 1 located in the right liver. The GTV, PTV and adjacent organs are outlined using color-coded solid lines. This configuration was used for 3DCRT, IMRT, and VMAT treatment plans. (c) Schematic illustration of Lesion 2 located anterior to the liver, used for a VMAT treatment plan. (d) Schematic illustration of Lesion 3 located in abdominal soft tissue lateral to the liver, used for a VMAT treatment plan. (e) Schematic illustration of Lesion 4 located in the right kidney. The spine partially blocked the acoustic propagation path between the transducer and the lesion. This configuration was used for a VMAT treatment plan. 53
Figure 4.2 Sagittal dose maps and isodose line comparisons between the treatment plan and iRAI for Lesion 1. Sagittal sections are taken through the center of the PTV. (a) Treatment plan dose distribution for 3DCRT. (b) Reconstructed iRAI dose distribution for 3DCRT. (c) Treatment plan dose distribution for IMRT. (d) Reconstructed iRAI dose distribution for IMRT. (e) Treatment plan dose distribution for VMAT. (f) Reconstructed iRAI dose distribution for VMAT. (g–i) Isodose line comparisons (50% blue, 70% green, 90% red) for 3DCRT, IMRT, and VMAT, respectively. Treatment plan contours are shown as dashed lines and iRAI contours as solid lines. Scale bars represent 2 cm. 57
Figure 4.3 Axial dose maps and isodose line comparisons between the treatment plan and iRAI for Lesion 1. Axial sections are taken through the center of the PTV. (a) Treatment plan dose distribution for 3DCRT. (b) Reconstructed iRAI dose distribution for 3DCRT. (c) Treatment plan dose distribution for IMRT. (d) Reconstructed iRAI dose distribution for IMRT. (e) Treatment plan dose distribution for VMAT. (f) Reconstructed iRAI dose distribution for VMAT. (g–i) Isodose line comparisons (50% blue, 70% green, and 90% red) for 3DCRT, IMRT, and VMAT, respectively. Treatment plan contours are shown as dashed lines, and iRAI contours are shown as solid lines. Scale bars represent 2 cm. 58
Figure 4.4 Sagittal dose maps and isodose line comparisons between the treatment plan and iRAI for Lesions 2–4. Sagittal sections are taken through the center of the PTV. (a) Treatment plan dose distribution for Lesion 2 (anterior to the liver). (b) Reconstructed iRAI dose distribution for Lesion 2. (c) Treatment plan dose distribution for Lesion 3 (abdominal soft tissue lateral to the liver). (d) Reconstructed iRAI dose distribution for Lesion 3. (e) Treatment plan dose distribution for Lesion 4 (right kidney, adjacent to the spine). (f) Reconstructed iRAI dose distribution for Lesion 4. (g–i) Isodose line comparisons (50% blue, 70% green, and 90% red) for Lesions 2–4, respectively. Treatment plan contours are shown as dashed lines, and iRAI contours are shown as solid lines. Scale bars represent 2 cm. 59
Figure 4.5 Axial dose maps and isodose line comparisons between the treatment plan and iRAI for Lesions 2–4. Axial sections are taken through the center of the PTV. (a) Treatment plan dose

distribution for Lesion 2. (b) Reconstructed iRAI dose distribution for Lesion 2. (c) Treatment plan dose distribution for Lesion 3. (d) Reconstructed iRAI dose distribution for Lesion 3. (e) Treatment plan dose distribution for Lesion 4. (f) Reconstructed iRAI dose distribution for Lesion 4. (g–i) Isodose line comparisons (50% blue, 70% green, and 90% red) for Lesions 2–4, respectively. Treatment plan contours are shown as dashed lines, and iRAI contours are shown as solid lines. Scale bars represent 2 cm. 60
Figure 4.6 DVH comparisons between the treatment plan (solid lines) and iRAI (dotted lines) for the PTV and corresponding OAR (liver or kidney) in each case. a, Lesion 1 in the right liver treated with 3DCRT. b, Lesion 1 treated with IMRT. c, Lesion 1 treated with VMAT. d, Lesion 2 located anterior to the liver (VMAT). e, Lesion 3 located in abdominal soft tissue lateral to the liver (VMAT). f, Lesion 4 in the right kidney (VMAT). Dose is normalized to the maximum value of the corresponding treatment plan, and volume is normalized to the structure volume. g, MAE between treatment plan and iRAI DVHs for the PTV in each case. h, MAE between treatment plan and iRAI DVHs for the OAR in each case. 63
Figure 5.1 Schematic of the dual-modality PA–US imaging system and *in vivo* experimental setup. (a) The endoscopy platform allows insertion of the imaging catheter through the biopsy channel for either APC (animal experiments only) or PA–US imaging. (b) A tunable pulsed laser provides optical excitation for PA imaging, while the Verasonics system acquires PA and US signals, performs image reconstruction, and displays co-registered images in real time. 68
Figure 5.2 Schematics of the water-balloon catheter integrated with a clinical endoscope. (a) Schematic of the balloon section of the catheter with labeled components and dimensions. (b) and (c) Photographs of the distal balloon section before and after inflation, respectively. (d) Photograph showing the catheter extending from the distal end of the endoscope. (e) Photograph of the catheter inserted through the endoscope biopsy channel (3.2 mm in diameter). (f) Illustration of the balloon inflation process using a hydrostatic pump. Markers 1, 2, and 3 indicate the three ports of the three-way stopcock. 69
Figure 5.3 Spatial resolution and frequency response of the PA–US catheter. (a) PA image of the cross-section of a 200 μm black polyethylene wire positioned at the balloon surface. (b) Lateral and axial point spread functions at the balloon surface, derived from the image in (a) after deconvolution with the wire cross-sectional profile. The lateral and axial full widths at half maximum (FWHM) are 143 μm and 104 μm, respectively. (c) Representative radiofrequency signal from the catheter transducer (black) and its corresponding frequency spectrum (red), obtained from manufacturer-provided characterization data. 70
Figure 5.4 Endoscopic images of APC modeling and PA–US imaging procedures. (a) Normal esophageal tissue in the pig. (b) APC procedure, with the white arrow indicating the APC catheter

that generates localized thermal coagulation for controlled mucosal injury. (c) The treated site 14 days after APC. (d) Endoscopic view of the balloon catheter (white arrow) inserted into the esophagus prior to inflation. (e) and (f) PA imaging at the target site using 800 nm illumination. The water-filled balloon conforms to the esophageal wall, ensuring effective acoustic coupling. 71
Figure 5.5 Clinical endoscopy suite and experimental setup for *in vivo* PA–US imaging during human endoscopic procedures. 73
Figure 5.6 Histological scoring of normal (no APC) and APC-treated esophageal segments in the porcine model. Inflammation and fibrosis were evaluated using H&E staining and Masson's trichrome staining, respectively, and graded on a semiquantitative 0–4 scale. Scoring was performed in a blinded manner. Statistical comparisons were conducted using two-sided Wilcoxon rank-sum tests. *** $p < 0.001$. 75
Figure 5.7 Validation of measurement consistency in PA signals acquired with the dual-modality imaging catheter. (a) Average PA signal magnitudes of the esophageal wall at baseline (T1), measured at multiple esophageal positions (25–50 cm). (b) PA signal magnitudes measured 14 days after APC treatment (T2). Positions at 30, 40, and 50 cm were APC-treated, while positions at 25, 35, and 45 cm served as untreated controls. 76
Figure 5.8 Representative US and PA images of the porcine esophagus. (a–c) Conventional B-mode US images of baseline (before treatment), untreated control, and APC-treated locations (14 days after APC), respectively. (d–f) Spectrally unmixed PA images showing relative HbT distributions. (g–i) Spectrally unmixed PA images showing relative collagen distribution. (j–k) Corresponding Masson's trichrome histological sections collected during necropsy. Solid black arrows denote blood vessels, and single white arrows mark normal structural collagen. Double white arrows indicate areas of pathological collagen deposition and transmural fibrosis. Arrows in (a–i) indicate the balloon–tissue interface. Scale bars: 3 mm for US and PA images. Histology scale bars: untreated control = 200 μm, APC lesion = 500 μm. 77
Figure 5.9 Quantitative comparison of chromophore signals derived from spectroscopic PA imaging. (a) Relative HbT signals measured at baseline, untreated control, and APC-treated locations. (b) Relative collagen signals measured in the same groups. Error bars represent mean ± SD across position-level samples, and dots indicate individual measurements. Statistical comparisons were performed using two-sided Wilcoxon rank-sum tests. *** $p < 0.001$, ** $p < 0.01$, * $p < 0.05$, n.s. = not significant. 78
Figure 5.10 *In vivo* PA–US imaging of intestinal tissue in a CD patient. (a) Schematic illustration of the J-pouch anatomy and the location of the anal canal anastomotic stricture. (b) Images acquired at an anal canal anastomotic stricture distal to the J pouch (top row) and from a non-

fibrotic, non-inflamed ileal segment proximal to the stricture (bottom row). White-light endoscopic images show the catheter and hydrostatic balloon when fully deployed. In the US and PA images, blue arrows indicate the US transducer array located at the top of the images, and red arrows mark the inner and outer surfaces of the bowel wall. Scale bar: 1 mm. 79

List of Tables

Table 1.1 Comparison of commonly used dosimetry methods in radiotherapy. 9
Table 2.1 Comparison of dose mapping accuracy with and without ultrasound-based motion correction across different motion scenarios. 35
Table 4.1 DVH metrics for PTV and OARS from TPS and IRAI. 63

List of Acronyms

iRAI	Ionizing radiation acoustic imaging
iRAI–US	Ionizing radiation acoustic imaging–ultrasound
PA–US	Photoacoustic–ultrasound
3D	Three-dimensional
PA	Photoacoustic
IARC	International Agency for Research on Cancer
CT	Computed tomography
DNA	Deoxyribonucleic acid
2D	Two-dimensional
3DCRT	Three-dimensional conformal radiotherapy
IMRT	Intensity-modulated radiotherapy
VMAT	Volumetric-modulated arc therapy
IGRT	Image-guided radiotherapy
TLD	Thermoluminescent dosimeter
OSLD	Optically stimulated luminescent dosimeter
EPID	Electronic portal imaging device
CD	Crohn's disease
MRI	Magnetic resonance imaging
US	Ultrasound
HbO_2	Oxygenated hemoglobin
HbR	Deoxygenated hemoglobin
MAT	Matrix array transducer
LINAC	Linear accelerator
SSIM	Structural similarity index measure
GPR	Gamma passing rate
DAS	Delay-and-sum
DD/DTA	Dose difference/distance to agreement
DVH	Dose–volume histogram

RMSE	Root-mean-square error
CBCT	Cone-beam computed tomography
GTV	Gross tumor volume
PTV	Planning target volume
OAR	Organ at risk
SBRT	Stereotactic body radiation therapy
MAE	Mean absolute error
D95	Dose received by 95% of the PTV volume
D2	Dose received by the hottest 2% of the PTV volume
Dmean	Mean dose
TPS	Treatment planning system
OPO	Optical parametric oscillator
APC	Argon plasma coagulation
FWHM	Full width at half maximum
IACUC	Institutional Animal Care and Use Committee
AVMA	American Veterinary Medical Association
USDA	United States Department of Agriculture
HbT	Total hemoglobin
IRB	Institutional Review Board
IPAA	Ileal pouch–anal anastomosis
H&E	Hematoxylin and eosin
ROI	Region of interest

Abstract

Radiotherapy treats cancer by delivering ionizing radiation to the tumor while limiting damage to surrounding healthy tissues. Accurate delivery of the planned dose is therefore essential for treatment effectiveness and safety. However, respiratory motion, anatomical changes, and patient positioning errors can cause deviations between planned and delivered dose. Current dosimetric and image-guidance technologies support treatment planning, quality assurance, and anatomical alignment, but they do not directly measure three-dimensional (3D) dose deposition inside the human body in real time. As a result, clinically relevant dose deviations cannot be fully detected during treatment. Ionizing radiation acoustic imaging (iRAI) offers a potential solution by detecting radiation-induced acoustic signals that are intrinsically related to radiation dose deposition, enabling real-time *in vivo* 3D dose mapping. This dissertation advances iRAI through three connected developments. First, a dual-modality iRAI–ultrasound system was developed for volumetric dose-on-anatomy visualization and assessment of motion-induced dose–target misalignment. Second, a sensitivity-compensated reconstruction method was developed to reduce transducer-related spatial bias and improve dose reconstruction accuracy. Third, iRAI was evaluated in an anthropomorphic abdominal phantom to assess dose mapping performance across selected anatomical configurations and clinical delivery techniques.

Inflammatory bowel disease, particularly Crohn's disease, causes transmural intestinal damage driven by inflammation and fibrosis, resulting in pain, obstruction, and reduced quality of life. Conventional endoscopy mainly visualizes surface features and cannot assess deeper tissue composition, limiting differentiation between inflammatory and fibrotic changes and leading to inappropriate treatment decisions. To address this, this dissertation developed a biopsy-channel-compatible photoacoustic–ultrasound (PA–US) catheter that integrates PA molecular contrast with US structural imaging for intraluminal gastrointestinal assessment. In a pig fibrosis model induced by argon plasma coagulation, hemoglobin and collagen contrasts distinguished inflammatory and fibrotic tissue features. Human studies further demonstrated the potential of PA–US to identify intestinal strictures and support disease characterization during endoscopic evaluation.

Together, these studies demonstrate the feasibility of acoustic imaging as a complementary tool for real-time *in vivo* dose monitoring in radiotherapy and intraluminal assessment of gastrointestinal inflammation and fibrosis.

Chapter 1 Introduction

Cancer remains a leading cause of morbidity and mortality worldwide [1-3]. Modern cancer management increasingly relies on multimodal strategies that combine surgery, systemic therapy, and radiotherapy, selected according to tumor type, disease stage, and patient condition [4-10]. This chapter outlines the scientific background and motivation of this dissertation. It begins with an overview of cancer biology, global disease burden, and current treatment approaches, followed by a review of radiotherapy, including its physical principles, technological evolution, and the roles of image guidance and dosimetry in clinical practice. Despite substantial advances in treatment planning and image guidance, a practical method for real-time, *in vivo* verification of 3D dose delivery within the patient remains unavailable [11-13]. Current dosimetry methods do not provide real-time measurements of delivered dose, making it difficult to detect deviations from the treatment plan. [13-17]. This gap motivates the development of ionizing radiation acoustic imaging (iRAI). This chapter introduces the underlying physical principles of iRAI, reviews prior work from theoretical modeling to early experimental validation and discusses the technical challenges that need to be addressed for clinical translation.

In parallel, this dissertation also investigates a photoacoustic–ultrasound (PA–US) catheter for intraluminal imaging of gastrointestinal inflammation and fibrosis. In conditions such as inflammatory bowel disease, pathological changes including inflammation and fibrosis often extend beyond the mucosal surface and cannot be fully characterized by standard endoscopy alone [18-20]. PA imaging offers molecular contrast based on optical absorption, providing sensitivity to vascular and collagen-related changes within the bowel wall [21-23]. These capabilities motivate the development of catheter-based PA–US systems for intraluminal gastrointestinal imaging.

The chapter concludes with an overview of the scope and main contributions of the dissertation.

1.1 Cancer

Cancer refers to a group of diseases characterized by uncontrolled cell growth and the ability of abnormal cells to invade surrounding tissues and metastasize to distant organs [24-26]. These processes arise from the accumulation of genetic and epigenetic alterations that disrupt normal regulation of cell proliferation, apoptosis, and tissue homeostasis [27, 28]. Despite substantial heterogeneity in biological behavior, cancers share a common consequence: progressive impairment of organ function and, if left untreated, eventual mortality. For this reason, cancer is not viewed as a single disease entity, but rather as a collection of related disorders that differ in origin, progression, and therapeutic response, and therefore require diverse diagnostic and treatment strategies.

1.1.1 Global Cancer Burden

Cancer has become a major global health challenge and a leading cause of premature mortality and disability [29-31]. According to GLOBOCAN 2020 estimates from the International Agency for Research on Cancer (IARC), approximately 19.3 million new cancer cases and 10.0 million cancer deaths occurred worldwide in 2020 [32, 33]. Beyond its biological complexity, cancer imposes a substantial socioeconomic burden on healthcare systems and societies. With continued population growth and aging, the global incidence of cancer is projected to increase to 28.4 million new cases annually by 2040, representing a 47% rise compared with 2020 [34-36].

In addition to demographic changes, lifestyle-related risk factors contribute significantly to this trend. Tobacco use remains the most preventable cause of cancer worldwide and is strongly associated with malignancies of the lung, head and neck, esophagus, and several other organs [37, 38]. Meanwhile, the increasing prevalence of obesity, unhealthy diet, and physical inactivity has been linked to elevated risks of colorectal, breast, and pancreatic cancers, reflecting the growing impact of metabolic and lifestyle factors on global cancer incidence [39, 40]. Environmental exposures, occupational hazards, and inherited genetic factors also play important roles in cancer development [41, 42]. Long-term exposure to environmental carcinogens such as air pollution, ultraviolet radiation, and industrial chemicals can increase cancer risk, while inherited mutations in cancer susceptibility genes further contribute to disease occurrence in certain populations [43-45].

The global cancer burden is unevenly distributed across regions [46, 47]. High-income countries often report higher incidence rates due to widespread screening programs, improved diagnostic technologies, and more comprehensive cancer registries, which enable earlier detection and more complete reporting of cases [48, 49]. In contrast, low- and middle-income countries experience disproportionately high mortality rates despite sometimes lower reported incidence [49, 50]. This imbalance is largely driven by delayed diagnosis, limited access to timely and effective treatment, and constrained healthcare resources. Consequently, many patients in these regions are diagnosed at advanced stages of disease, when treatment options are more limited and outcomes are poorer. These disparities highlight the need for continued progress not only in cancer treatment, but also in early detection, prevention, and equitable access to cancer care worldwide.

1.1.2 Classification of Cancer

Cancers are highly heterogeneous and are commonly classified according to tissue of origin and biological characteristics [51, 52]. Carcinomas, which arise from epithelial tissues, constitute the majority of malignancies and include many of the most prevalent cancer types, such as lung, breast, prostate, colorectal, liver, and pancreatic cancers [53, 54].

Sarcomas originate from mesenchymal tissues including bone, cartilage, muscle, and connective tissue [55]. Although less common than carcinomas, sarcomas are often clinically aggressive and present unique diagnostic and treatment challenges [56, 57]. Hematological malignancies, including leukemias and lymphomas, arise from bone marrow and lymphatic tissues and are typically systemic rather than localized, requiring distinct therapeutic approaches [58, 59].

Tumors of the central nervous system, such as gliomas and meningiomas, represent another biologically distinct category [60]. Despite lower incidence compared with carcinomas, these tumors are associated with substantial morbidity due to their critical anatomical location.

The diversity of cancer subtypes has important implications for diagnosis and treatment. Variability across and within tumor types has driven increasing emphasis on personalized treatment strategies, integration of multimodal therapies, and the use of advanced imaging to guide and monitor therapeutic interventions.

1.1.3 Approaches to Cancer Treatment

Cancer treatment has evolved from predominantly surgical interventions to multimodal strategies that integrate local and systemic therapies [61, 62]. Surgery remains the cornerstone of

curative treatment for many localized solid tumors, aiming to achieve complete resection of malignant tissue while preserving organ function [4, 63]. Surgical intervention enables direct removal of the primary tumor and provides pathological evaluation of tumor stage and surgical margins [64, 65]. However, surgery alone is often insufficient for advanced or locally invasive disease, particularly when tumors infiltrate surrounding tissues or metastasize to distant organs [66, 67]. Even after apparently complete tumor resection, postoperative recurrence occurs in approximately 20–50% of patients depending on cancer type, and many patients with metastatic or locally advanced disease are not eligible for curative surgical resection [68, 69].

Radiotherapy plays a central role in modern cancer care as a noninvasive local treatment that can deliver cytotoxic radiation doses to tumors while sparing surrounding normal tissues [7, 70-73]. It is widely used across many cancer types as a definitive treatment, an adjuvant following surgery to reduce recurrence risk, or in combination with systemic therapies to enhance treatment effectiveness [74, 75]. However, treatment outcomes depend critically on accurate dose delivery and careful management of radiation exposure to surrounding normal tissues. Chemotherapy provides systemic control by targeting rapidly dividing cells and is therefore commonly used for metastatic disease or cancers with a high risk of systemic spread. This lack of selectivity causes toxicity in normal tissues such as bone marrow, gastrointestinal epithelium, and hair follicles, resulting in complications including myelosuppression, mucositis, and alopecia [76, 77]. Severe treatment-related adverse events occur in approximately 20–40% of patients, depending on the regimen and cancer type [78].

Advances in molecular biology and immunology have further expanded therapeutic options. Targeted therapies, such as tyrosine kinase inhibitors and monoclonal antibodies, exploit specific molecular alterations that drive tumor growth and signaling pathways [79, 80]. Immunotherapies, including immune checkpoint inhibitors and CAR-T cell therapy, harness the immune system to recognize and eliminate malignant cells [81, 82]. While these approaches have produced remarkable responses in certain cancers, treatment outcomes remain highly variable, with objective response rates often in the range of 10–30% across many solid tumors [83, 84]. In addition, targeted therapies may lose effectiveness due to acquired resistance, and immunotherapies can produce immune-related adverse events affecting organs such as the skin, liver, lungs, and endocrine system, which may require treatment interruption or long-term

management [85, 86]. High treatment costs and limited accessibility also remain important barriers in many healthcare settings [87].

Given the biological heterogeneity of cancer, optimal management often relies on integrated treatment strategies that combine surgery, radiotherapy, and systemic therapy [88]. Advances in medical imaging have improved treatment planning and targeting precision across these modalities. Nevertheless, for radiotherapy in particular, treatment accuracy ultimately depends on how closely the delivered dose matches the planned distribution, highlighting the need for methods that can assess dose delivery during treatment rather than relying solely on pre-treatment calculations.

1.2 Radiotherapy

Large population-based analyses indicate that approximately 50–60% of cancer patients receive radiotherapy at least once during the course of their disease [73, 89-91]. Radiotherapy contributes to cancer cure or long-term local control in an estimated 40% of patients achieving curative outcomes, underscoring its central role alongside surgery and systemic therapy [92, 93]. It serves as definitive treatment for many localized tumors, reduces recurrence in the adjuvant setting, and remains an effective modality for symptom palliation in advanced disease [94].

Radiotherapy achieves tumor control by depositing ionizing radiation energy in tissue to induce biological damage in cancer cells, while treatment planning and delivery aim to confine the prescribed dose to the target and minimize exposure to surrounding organs at risk (OAR) [95]. Advances in delivery techniques have enabled increasingly conformal dose distributions and improved geometric precision, supporting selective dose escalation while sparing normal tissues [96, 97]. These improvements, however, place greater demands on accurate treatment execution and verification.

Figure 1.1 summarizes the modern radiotherapy workflow and the biological mechanisms of radiation-induced tumor control. Radiotherapy begins with volumetric imaging, typically planning computed tomography (CT), to delineate targets and OARs. Treatment planning optimizes beam geometry, intensity modulation, and dose constraints to achieve conformal dose delivery. Irradiation is delivered using a linear accelerator (LINAC), often with image guidance to verify positioning prior to treatment. At the cellular level, ionizing radiation deposits energy within tissue, leading to tumor cell death through direct deoxyribonucleic acid (DNA) damage and

indirect damage mediated by reactive oxygen species, including hydroxyl radicals (·OH) generated along radiation tracks [98].

Despite these advances, residual uncertainties in treatment accuracy can result in clinically meaningful deviations between intended and delivered dose distributions, potentially compromising tumor control or increasing toxicity.

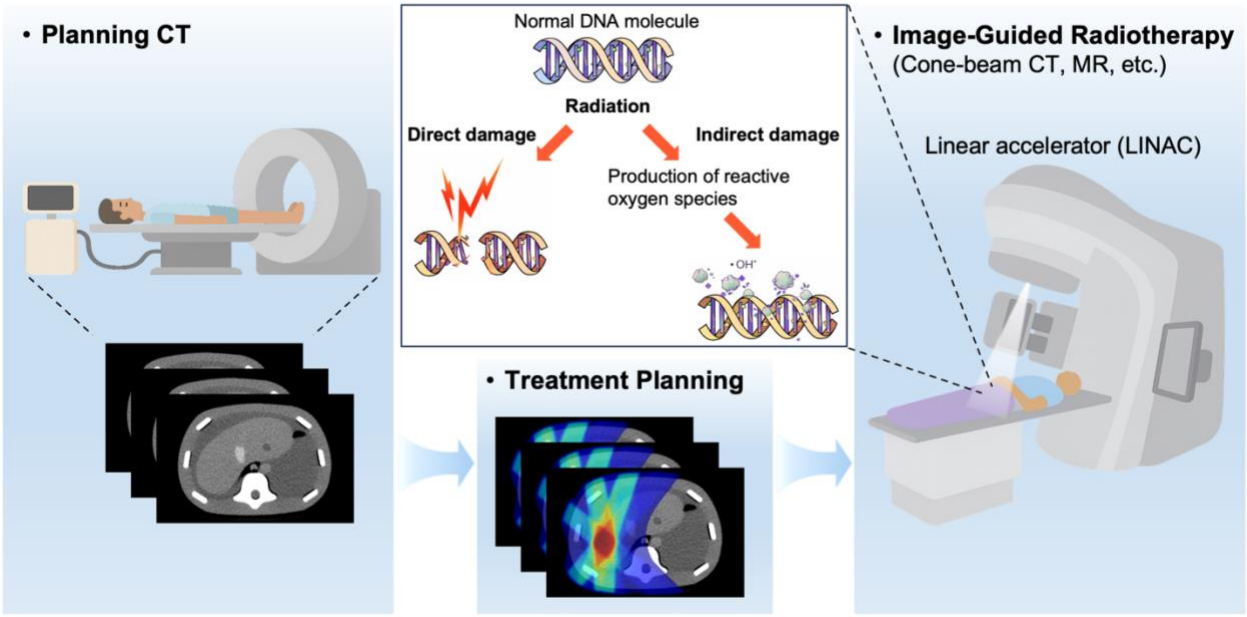


Figure 1.1 Overview of modern radiotherapy workflow and radiation-induced biological mechanisms. Radiotherapy begins with volumetric imaging, typically planning CT, to delineate the target and surrounding OAR. Treatment planning is then performed to optimize dose delivery, followed by irradiation using a LINAC with image-guided radiotherapy for patient positioning verification. At the cellular level, ionizing radiation induces tumor cell death through both direct DNA damage and indirect damage mediated by reactive oxygen species, primarily hydroxyl radicals (·OH).

1.2.1 Principles of Radiotherapy

Radiotherapy is a fundamental modality in modern oncology that uses ionizing radiation to damage malignant cells and inhibit tumor growth [99]. When high-energy photons, electrons, or charged particles traverse tissue, they deposit energy through ionization and excitation, generating secondary electrons and free radicals that disrupt cellular molecular structures [100, 101]. The primary biological target of radiation is DNA [101]. Radiation-induced damage includes base lesions, single-strand breaks, and double-strand breaks, the latter being particularly critical because they compromise chromosomal integrity and cell division [95, 102, 103]. If unrepaired or misrepaired, such damage can lead to mitotic arrest, apoptosis, or loss of reproductive capacity [104, 105].

Both normal and malignant tissues are exposed during radiotherapy. The therapeutic effect arises from differences in radiation response: cancer cells often exhibit impaired DNA repair and dysregulated cell cycle control, whereas many normal tissues retain greater repair and repopulation capacity, allowing partial recovery between fractions [106, 107]. Consequently, radiotherapy is delivered in multiple fractions to accumulate lethal tumor damage while limiting normal tissue injury [108]. Treatment outcome depends not only on total dose but also on fraction size and overall treatment time [109, 110].

Together, these physical and biological principles define the foundation of modern radiotherapy.

1.2.2 Evolution of Radiotherapy Delivery Techniques

Radiotherapy delivery techniques have evolved substantially over the past decades, progressing from simple geometric field arrangements to highly conformal dose delivery [111]. Early two-dimensional (2D) approaches relied on planar imaging and uniform radiation fields defined by external landmarks, resulting in limited conformity to complex tumor shapes and substantial irradiation of surrounding normal tissues [112].

The introduction of three-dimensional conformal radiotherapy (3DCRT) enabled CT-based planning with explicit delineation of targets and OARs [113]. Intensity-modulated radiotherapy (IMRT) further advanced this capability by allowing spatial modulation of beam intensity through inverse planning, producing steep dose gradients and improved sparing of adjacent critical structures [114]. Volumetric-modulated arc therapy (VMAT) extended this approach through continuous gantry rotation with dynamic modulation of dose rate and multileaf collimator motion, improving delivery efficiency while maintaining high conformity [115].

Particle therapies, including proton and carbon-ion radiotherapy, exploit distinct physical dose deposition characteristics [116]. Charged particles deposit most of their energy near the end of their range, forming a Bragg peak that enables sharp distal dose falloff and reduced dose to tissues beyond the target [117].

These developments have transformed radiotherapy into a highly engineered, patient-specific process capable of delivering complex dose distributions. As conformity increases and treatment margins narrow, accurate delivery of the planned dose becomes increasingly critical.

1.2.3 Image Guidance in Modern Radiotherapy

Early radiotherapy relied on external markers and bony anatomy for patient setup [118]. While acceptable for large treatment fields with relatively shallow dose gradients, this approach was insufficient for soft-tissue targets with substantial day-to-day variability [119]. Physiological processes such as respiration, organ filling, and anatomical changes introduce positional uncertainty, particularly in the presence of steep dose gradients where small geometric deviations can lead to meaningful dose differences [112, 120].

To address these limitations, image guidance has been incorporated into modern radiotherapy workflows [121]. Contemporary image-guided radiotherapy (IGRT) systems integrate imaging hardware directly into the treatment platform to localize the target and surrounding anatomy prior to or during delivery [122, 123]. Most LINACs are equipped with on-board imaging capabilities that enable verification of patient positioning and correction for inter-fraction variation [124].

However, these capabilities primarily address geometric alignment rather than direct measurement of delivered dose. Although some platforms support intra-fraction imaging, the acquired information typically represents anatomical configuration rather than dose deposition [112]. As a result, intra-fraction motion, anatomical deformation, and biological changes during treatment can alter the actual dose distribution without being fully captured by geometric verification alone.

This limitation highlights the need for complementary dosimetric methods that can directly assess delivered dose *in vivo* during radiotherapy.

1.2.4 Limitations of Current Dosimetry

Despite the availability of multiple clinical dosimetry techniques, practical verification of radiation dose delivery within the patient remains limited. A major challenge arises from anatomical motion and deformation during treatment [125, 126]. Physiological processes such as respiration, cardiac motion, and gastrointestinal activity can shift internal organs during irradiation [127, 128]. For thoracic and abdominal tumors, respiratory motion alone can result in target displacements on the order of 5–20 mm, altering the spatial relationship between the radiation beam and the intended target volume [129].

More fundamentally, current dosimetry methods do not provide direct, real-time verification of dose deposition within the body. Existing approaches are typically restricted to

surface, point, or planar measurements, or rely on post-acquisition reconstruction [130, 131]. Consequently, they cannot resolve the evolving 3D dose distribution within internal tissues during irradiation.

This limitation becomes more critical in modern radiotherapy, where highly conformal delivery and steep dose gradients increase sensitivity to geometric and anatomical uncertainty. Over the course of 20–40 fractions, additional variations arise from tumor regression, organ filling, weight loss, and other physiological changes, further increasing discrepancies between planned and delivered dose distributions [132, 133].

Table 1.1 summarizes the principal characteristics of commonly used dosimetry techniques in clinical practice [134-138]. Current methods provide limited *in vivo* capability, restricted spatial sampling, or retrospective readout. Although some techniques offer partial real-time or volumetric information, comprehensive verification of the full 3D dose distribution during irradiation remains unavailable.

The lack of real-time, volumetric, and *in vivo* dose assessment represents a fundamental limitation in current radiotherapy workflows. Addressing this challenge requires approaches capable of directly sensing radiation-induced signals within tissue and reconstructing dose distributions with high spatial and temporal resolution.

Table 1.1 Comparison of commonly used dosimetry methods in radiotherapy.

Method	**In vivo**	**Real-time**	**3D**	**Remarks**
Ion chamber	Limited	Yes	No	Point measurement
Diode	Limited	Yes	No	Energy and angle dependent
Film	No	No	No	2D, post-irradiation readout
TLD / OSLD	Limited	No	No	Retrospective
EPID	Limited	Limited	Yes	Model-dependent reconstruction

1.3 Ionizing Radiation Acoustic Imaging (iRAI)

1.3.1 Principles of iRAI

iRAI is based on the generation of acoustic waves following rapid energy deposition by ionizing radiation in tissue [139]. When a pulsed X-ray beam irradiates biological tissue, a fraction of the absorbed energy is converted into heat, producing a transient temperature rise within the irradiated volume. This localized heating induces thermoelastic expansion, which acts as an initial

pressure source and generates broadband acoustic waves that propagate through tissue and can be detected by external US transducers.

Figure 1.2 illustrates the conceptual framework of iRAI for dose visualization during radiotherapy. By synchronizing acoustic signal acquisition with radiation pulse delivery, the detected radiation-induced acoustic signals can be reconstructed to form spatial maps that reflect the distribution of deposited dose relative to anatomical structures.

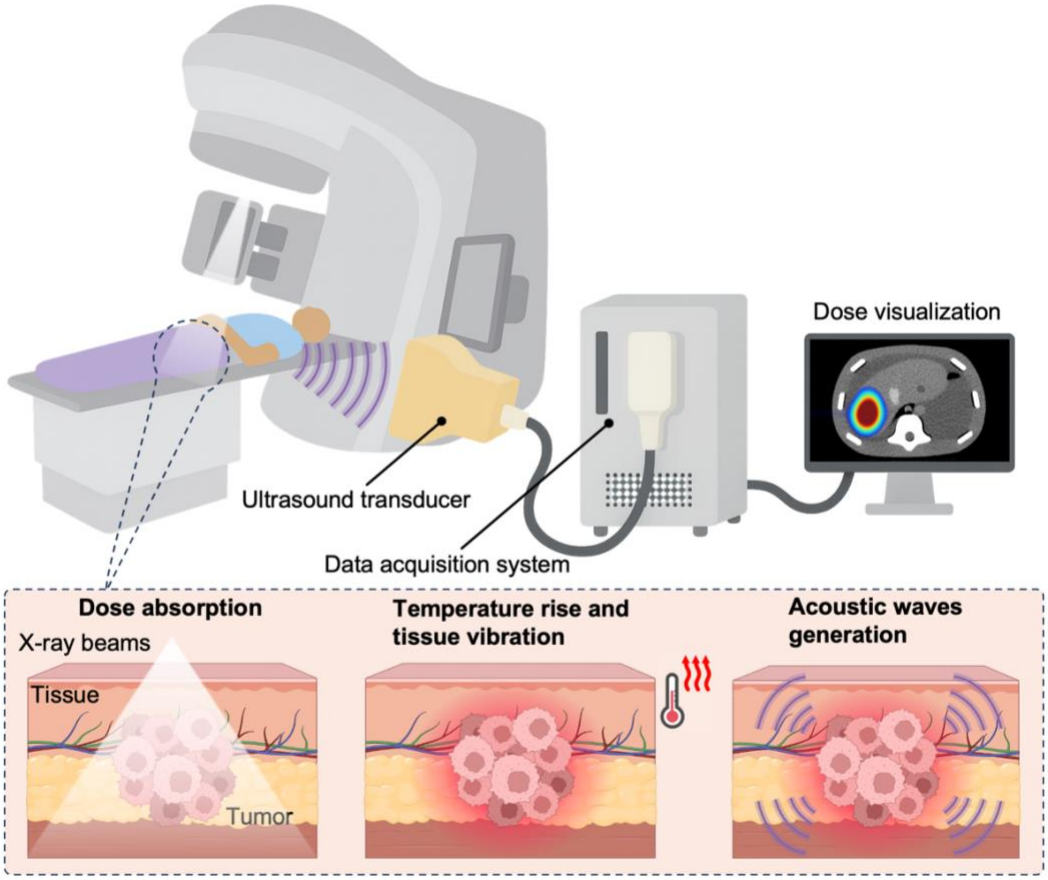


Figure 1.2 Schematic illustration of iRAI for dose visualization during radiotherapy. Pulsed X-ray irradiation deposits energy in tissue, producing a transient temperature rise and thermoelastic expansion that generates acoustic waves. These radiation-induced acoustic signals are detected by an external US transducer and reconstructed to map the spatial distribution of dose deposition.

Let $D(\boldsymbol{r}, t)$ denote the cumulative radiation dose deposited at spatial location $\boldsymbol{r} \in \boldsymbol{R^3}$ up to time t. The dose-rate profile during irradiation is given by the time derivative of the cumulative dose:

$$\dot{D}(\boldsymbol{r}, t) = \frac{\partial D(\boldsymbol{r}, t)}{\boldsymbol{\partial} t} \tag{1}$$

A fraction of the deposited radiation energy is converted into heat, resulting in a radiation-induced heat absorption rate:

$$H(\boldsymbol{r},t) = \eta_{th}\rho\dot{D}(\boldsymbol{r},t) \tag{2}$$

where η_{th} is the thermal conversion efficiency and ρ is the mass density of the medium.

The temperature rise generated by this heat source follows the heat diffusion equation. For the short X-ray pulse durations used in clinical LINACs and the relatively low thermal diffusivity of soft tissue, thermal diffusion during the pulse can be neglected. Under this thermal confinement condition, the temperature rise is determined primarily by the local energy deposition rather than heat transport. The resulting thermoelastic expansion serves as a source term in the acoustic wave equation:

$$\left(\nabla^2 - \frac{1}{v_s^2}\frac{\partial^2}{\partial t^2}\right)p(\boldsymbol{r},t) = -\frac{\beta}{C_v v_s^2}\frac{\partial H(\boldsymbol{r},t)}{\partial t} = -\frac{\beta\eta_{th}\rho}{C_v v_s^2}\frac{\partial \dot{D}(\boldsymbol{r},t)}{\partial t} \tag{3}$$

where $p(\boldsymbol{r},t)$ is the acoustic pressure, v_s is the speed of sound, β is the volumetric thermal expansion coefficient, and C_v is the specific heat capacity at constant volume. This equation shows that acoustic waves are generated by temporal variations in the heat deposition rate, rather than by static heating.

Solving the acoustic wave equation reveals that the detected pressure signals depend on the spatial distribution and temporal evolution of the dose-rate profile $\dot{D}(\boldsymbol{r},t)$, evaluated at retarded times determined by acoustic propagation. In clinical systems, the temporal profile of a single X-ray pulse typically spans only a few microseconds. When the acoustic detection bandwidth is insufficient to resolve this fine temporal structure, the pulse can be approximated as temporally compact relative to the acoustic detection bandwidth. By defining the start of the X-ray pulse as $t = 0$, the dose rate can be integrated over the pulse duration τ_p to yield the dose deposited per pulse:

$$D_p(\boldsymbol{r}) = \int_0^{\tau_p} \dot{D}(\boldsymbol{r},t)\,dt \tag{4}$$

Under thermal confinement, the pulse-integrated dose produces a transient temperature rise within the irradiated volume. The ensuing thermoelastic expansion generates an initial acoustic pressure rise proportional to the local temperature increase. Accordingly, the initial acoustic pressure immediately following energy deposition can be expressed as

$$p_0(\boldsymbol{r}) = \Gamma\frac{\eta_{th}\rho}{\tau_p}D_p(\boldsymbol{r}) \tag{5}$$

where $\Gamma = \frac{\beta K_T}{\rho C_v}$ is the Grüneisen parameter, and K_T is the isothermal bulk modulus.

Although the absolute recovery of the initial pressure distribution is challenging in practice, the reconstructed iRAI image reflects relative variations in the initial acoustic pressure $p_0(\boldsymbol{r})$. Because acoustic wave propagation, pressure detection, and image reconstruction are linear with respect to pressure amplitude, the relative spatial distribution of $p_0(\boldsymbol{r})$ is preserved in the reconstructed image. Accordingly, the reconstructed image intensity is proportional to the local dose deposited per pulse and can be expressed as

$$I(\boldsymbol{r}) \propto p_0(\boldsymbol{r}) \propto D_p(\boldsymbol{r}) \tag{6}$$

where $I(\boldsymbol{r})$ denotes the pixel intensity in the reconstructed iRAI image at spatial location $\boldsymbol{r}$. Consequently, the iRAI image enables visualization of radiation beam position, field shape, and dose distribution during irradiation.

1.3.2 Development and Current Progress

Early studies of iRAI focused on theoretical modeling and experimental validation. Numerical simulations were used to analyze the thermoelastic response of tissue following pulsed megavoltage irradiation and to predict the resulting acoustic pressure fields [140, 141]. These studies coupled radiation energy deposition with bioheat transfer and acoustic wave propagation models, establishing the physical framework for radiation-induced acoustic signal generation. Experimental validation was also performed using tissue-mimicking phantoms and *ex vivo* animal tissue [139, 142]. These studies enabled systematic characterization of acoustic signal amplitude, temporal response, and spatial resolution, demonstrated agreement between reconstructed iRAI images and reference dose measurements, and confirmed that radiation-induced acoustic signals could be detected in real biological tissue.

Subsequent work extended iRAI investigations to *in vivo* animal models [143, 144]. Experiments involving small-animal irradiation setups further supported the feasibility of integrating iRAI measurements within standard radiotherapy delivery workflows.

More recently, preliminary demonstrations have been reported in human radiotherapy environments [144, 145]. These studies showed that radiation-induced acoustic signals can be detected during clinical megavoltage beam delivery, and that iRAI can map volumetric radiation dose distributions within deep tissues.

1.3.3 Challenges and Limitations

Despite recent progress, several limitations remain in existing iRAI studies that restrict its practical use in radiotherapy.

First, most prior studies have focused on acoustic signal detection or image reconstruction alone, without direct integration with anatomical imaging. As a result, the reconstructed dose-related images lack clear spatial correspondence with underlying tissue structures, limiting their interpretability and clinical relevance.

Second, accurate quantitative dose mapping remains challenging in current iRAI implementations. Although the detected acoustic signals are related to deposited radiation dose, spatial variations in transducer detection sensitivity are not accounted for in conventional reconstruction, leading to inconsistencies in signal amplitude and reduced accuracy in dose mapping.

Third, existing studies have been conducted in simplified experimental settings, including homogeneous phantoms or limited tissue models. These conditions do not fully capture the complexity of clinically relevant scenarios, such as heterogeneous abdominal anatomy or realistic treatment geometries, making it difficult to assess system performance under practical conditions.

1.3.4 Significance

iRAI provides a distinct approach for monitoring radiation dose delivery during radiotherapy. Unlike conventional methods that rely on external measurements, surrogate indicators, or post-treatment verification, iRAI detects acoustic signals generated by radiation energy deposition within tissue. This direct physical relationship enables *in vivo* observation of dose deposition during irradiation.

Because the detected signals originate from the irradiated region, iRAI reflects dose deposition under patient-specific anatomical conditions, rather than relying solely on calculations from the treatment planning systems (TPS). In addition, ultrasound-based signal detection does not introduce additional ionizing radiation, allowing repeated or continuous monitoring without increasing patient dose.

The ability to observe dose deposition with both spatial and temporal resolution has the potential to reduce uncertainties associated with anatomical motion, delivery variability, and discrepancies between planned and delivered dose distributions. Such capabilities may improve treatment verification and enhance confidence in delivered radiation dose.

1.4 Photoacoustic Imaging for Assessment of Crohn's Disease

1.4.1 Crohn's Disease

Crohn's disease (CD) is a chronic inflammatory bowel disease characterized by recurrent inflammation of the gastrointestinal tract and progressive structural remodeling of the intestinal wall [146-149]. The disease can affect any segment of the digestive tract, from the mouth to the anus, although it most commonly involves the terminal ileum and colon [150]. Figure 1.3 illustrates the gastrointestinal tract and highlights the common sites of Crohn's disease involvement. Unlike ulcerative colitis, which is limited to the mucosa, CD frequently presents with transmural inflammation that extends through multiple layers of the bowel wall [151].

CD affects millions of individuals worldwide and represents a significant source of long-term morbidity [152]. The disease typically follows a relapsing–remitting course, with periods of active inflammation alternating with partial remission [152]. Common symptoms include abdominal pain, diarrhea, fatigue, weight loss, and nutritional deficiencies [153, 154]. In more severe cases, persistent inflammation can lead to complications such as fistulas, abscesses, and intestinal obstruction [155].

Over time, repeated cycles of inflammation and tissue repair drive progressive remodeling of the bowel wall [156]. Chronic inflammation promotes fibroblast activation and extracellular matrix deposition, leading to fibrotic thickening of intestinal tissue [157]. As the disease evolves, inflammatory and fibrotic processes often coexist within the same bowel segment, resulting in complex pathological changes that extend beyond the mucosal surface [18, 158, 159].

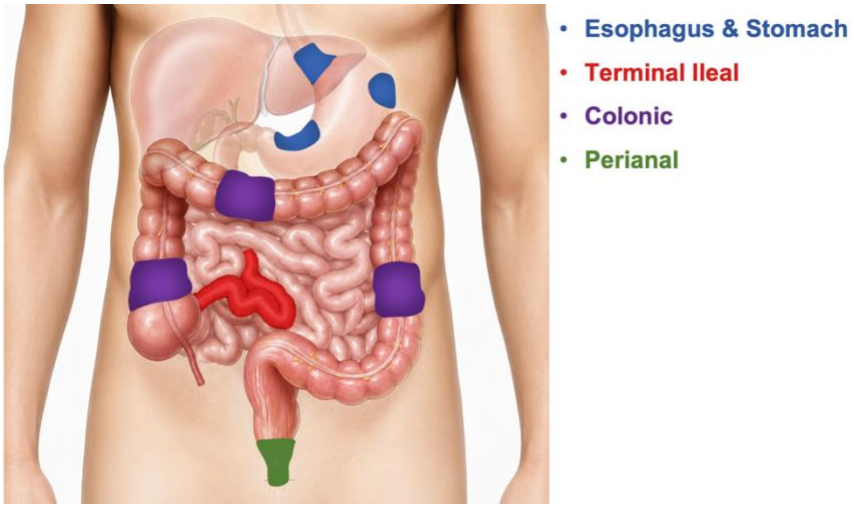


Figure 1.3 Schematic illustration of the gastrointestinal tract highlighting common sites of Crohn's disease involvement, including the esophagus, stomach, terminal ileum, colon, and perianal area.

1.4.2 Current Diagnostic Limitations in CD

Accurate assessment of disease activity in CD remains challenging in clinical practice [160]. This challenge is primarily driven by the coexistence of inflammatory and fibrotic components within the same bowel segment, which require fundamentally different treatment strategies. Predominantly inflammatory lesions may respond to anti-inflammatory or biologic therapies, whereas fibrotic strictures typically require endoscopic dilation or surgical intervention [161, 162].

Fibrotic complications are common during disease progression. Approximately 10% of patients present with intestinal strictures at diagnosis, and up to 50% develop a stricturing phenotype over time [163, 164]. These strictures are a major cause of bowel obstruction and frequently lead to surgery. Indeed, up to 70% of patients with CD eventually undergo intestinal resection during their lifetime, largely due to fibrostenotic disease [165].

Endoscopic evaluation with biopsy remains the clinical reference standard for the diagnosis of CD and provides valuable histological information [166, 167]. However, biopsy samples are typically limited to the superficial mucosa, restricting their ability to assess deeper pathological changes within the bowel wall. Because fibrosis often develops in submucosal and muscular layers, biopsy findings may not accurately reflect the extent of transmural remodeling [168, 169].

Cross-sectional imaging techniques, including US, CT, and magnetic resonance imaging (MRI), are widely used to evaluate bowel wall thickening and structural abnormalities [170, 171]. While these modalities provide important anatomical information, their ability to differentiate inflammation from fibrosis remains limited. Imaging features such as wall thickening, luminal narrowing, and contrast enhancement can arise from either process, leading to substantial diagnostic overlap. Consequently, the reported diagnostic accuracy of conventional imaging for distinguishing inflammatory and fibrotic lesions is generally moderate, with performance often reported in the range of approximately 60–80% [163, 172, 173].

Because treatment decisions critically depend on distinguishing inflammation from fibrosis, this limitation represents a major challenge in clinical management. It motivates the development of imaging approaches capable of providing composition-sensitive information about intestinal tissue, rather than relying solely on structural features.

1.4.3 Principles of Photoacoustic Imaging

Photoacoustic (PA) imaging is a hybrid imaging modality that combines optical excitation with ultrasonic detection to provide depth-resolved information about tissue composition [174, 175]. This capability is particularly relevant for gastrointestinal applications, where differentiation of tissue composition, such as inflammation and fibrosis, is clinically important. In PA imaging, short laser pulses illuminate biological tissue, where optical energy is absorbed by endogenous chromophores such as hemoglobin, melanin, lipids, and collagen [174]. The absorbed optical energy is partially converted into heat, leading to a transient temperature rise within the illuminated region [175].

Under thermal and stress confinement conditions, this rapid temperature increase induces thermoelastic expansion and generates broadband ultrasonic waves [21]. These pressure waves propagate through tissue and are detected by US transducers placed on the tissue surface. The recorded acoustic signals are then used to reconstruct images that represent the spatial distribution of optical absorption in the tissue, as illustrated in Figure 1.4.

The generation of PA signals can be described by the relationship between optical absorption and the resulting initial acoustic pressure. The initial pressure rise p_0 produced by optical absorption is given by

$$p_0 = \Gamma \mu_a F \tag{7}$$

where Γ is the Grüneisen parameter, representing the efficiency of conversion from thermal energy to pressure, μ_a is the optical absorption coefficient of the tissue, and F is local optical fluence. The Grüneisen parameter is defined as

$$\Gamma = \frac{\beta c^2}{C_p} \tag{8}$$

where β is the thermal expansion coefficient, c is the speed of sound in tissue, and C_p is the specific heat capacity at constant pressure. Once generated, the PA waves propagate through tissue and satisfy the acoustic wave equation

$$\nabla^2 p(\boldsymbol{r}, t) - \frac{1}{c^2}\frac{\partial^2 p(\boldsymbol{r}, t)}{\partial t^2} = -\frac{\beta}{C_p}\frac{\partial H(\boldsymbol{r}, t)}{\partial t} \tag{9}$$

where $p(\boldsymbol{r}, t)$ is the acoustic pressure, $H(\boldsymbol{r}, t)$ represents the rate of optical energy deposition.

Because PA signal generation depends on optical absorption while detection relies on acoustic propagation, PA imaging combines the molecular sensitivity of optical imaging with the

penetration depth of US. Optical scattering limits purely optical imaging to depths on the order of one millimeter in biological tissue, whereas ultrasonic waves can propagate several centimeters with relatively low scattering. As a result, PA imaging enables centimeter-scale imaging depth while preserving sensitivity to molecular composition.

In biological tissues, different molecular constituents exhibit distinct optical absorption spectra. Representative spectra of major chromophores, including oxygenated hemoglobin (HbO_2), deoxygenated hemoglobin (HbR), lipid, collagen, and water, are shown in Figure 1.5. In particular, hemoglobin is associated with vascular and inflammatory activity, while collagen is a key component of fibrotic tissue. Hemoglobin exhibits strong absorption in the visible and near-infrared ranges, whereas collagen and lipid show characteristic absorption features in the near-infrared region. By acquiring PA signals at multiple wavelengths, spectroscopic PA imaging enables estimation of the relative concentrations of different chromophores, facilitating functional and molecular imaging of biological tissues.

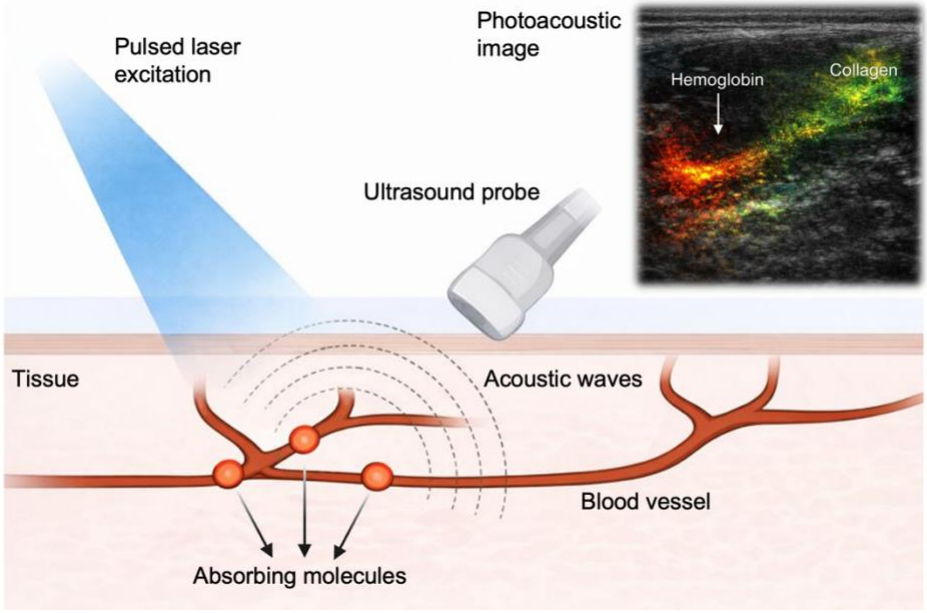


Figure 1.4 Illustration of the PA imaging principle. Optical absorption of pulsed laser energy induces thermoelastic expansion and generates acoustic waves, which are detected by an US probe to reconstruct images of chromophore distribution.

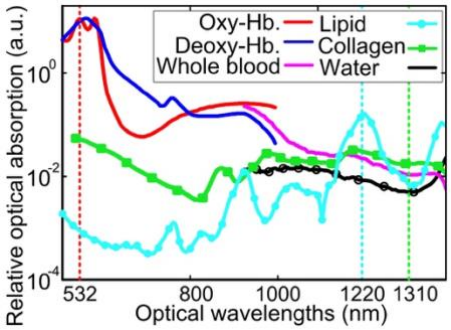


Figure 1.5 Relative optical absorption spectra of major chromophores in biological tissue. The vertical dashed lines indicate wavelengths at which different tissue components exhibit relatively strong optical absorption, corresponding to approximately 532 nm, 1220 nm, and 1310 nm. a.u., arbitrary units; Oxy-Hb., oxygenated hemoglobin; Deoxy-Hb., deoxygenated hemoglobin.

1.4.4 Evolution of PA Imaging for Intestinal Applications

PA imaging has been explored through several system designs for intestinal imaging, with progressive efforts to improve proximity to the bowel wall and measurement stability. Early studies investigated transabdominal PA imaging, demonstrating the feasibility of noninvasive detection of intestinal signals [176]. However, the large imaging depth and acoustic attenuation through abdominal tissues limited spatial resolution and localization accuracy, making it difficult to resolve detailed intestinal wall structures.

To improve proximity to the intestinal wall, capsule-based PA probes were subsequently developed [177]. These devices enabled closer access to the target tissue but remained limited by inadequate acoustic coupling and the lack of precise control over probe orientation within the gastrointestinal lumen.

Balloon-based catheter systems were later introduced to provide stable acoustic coupling and controlled contact with the intestinal wall [178]. The inflatable balloon maintains consistent contact with the tissue surface while stabilizing the imaging geometry. Despite these improvements, early balloon catheter designs were relatively bulky and incompatible with standard clinical endoscopes. Consequently, imaging often required a two-step workflow. An endoscope was first used to identify and localize the target region and was then withdrawn. The PA catheter was subsequently inserted based on the target location and depth estimated from the endoscopic examination. This approach introduced positioning uncertainty and limited the practicality of *in vivo* applications.

1.4.5 Endoscopic PA–US Imaging Catheter for Crohn's Disease

Endoscopic procedures provide a practical platform for deploying intraluminal imaging devices. An imaging catheter can be advanced through the working channel of a clinical endoscope and guided to specific locations within the intestine under direct visual observation. This enables precise positioning of the probe at regions of interest while maintaining stable contact with the bowel wall.

To address the limitations of existing PA imaging approaches, endoscope-compatible PA–US imaging catheters offer a feasible solution for performing *in vivo* PA measurements during routine endoscopic examinations. By integrating PA imaging with co-registered US, such systems can provide both compositional and structural information of intestinal tissue, enabling assessment of key pathological features associated with inflammatory bowel disease. In particular, this approach enables differentiation of inflammatory and fibrotic components within the bowel wall, which is critical for guiding treatment decisions in Crohn's disease.

1.5 Overview of Dissertation Scope

This dissertation consists of two parts. The first focuses on iRAI for real-time, *in vivo*, 3D mapping of radiotherapy dose deposition during treatment. The second presents a PA–US imaging catheter for intraluminal gastrointestinal imaging to characterize intestinal inflammation and fibrosis based on tissue composition.

The iRAI component comprises three main developments. First, a dual-modality iRAI–US volumetric imaging system was developed to co-register radiation dose with anatomical structures, enabling time-resolved visualization of dose-on-anatomy and providing a framework to address dose–target misalignment caused by anatomical motion. Second, a quantitative iRAI approach was established by incorporating voxel-wise transducer sensitivity compensation and validated through numerical simulations and homogeneous phantom experiments. This method corrects location-dependent detection sensitivity and improves the accuracy of dose reconstruction, representing a step toward quantitative iRAI. Third, the reliability of iRAI was systematically evaluated using an anthropomorphic abdominal phantom under multiple treatment delivery techniques and anatomical conditions.

The second part of the dissertation focuses on the development of a compact PA–US imaging catheter compatible with the biopsy channel of a clinical endoscope for intraluminal imaging. The system intestinal inflammation and fibrosis.

Chapter 2 Volumetric iRAI–US Imaging for Dose-on-Anatomy Visualization

2.1 Introduction

Accurate knowledge of the relationship between delivered radiation dose and patient anatomy is critical in modern radiotherapy, particularly in the presence of physiological motion. Although TPS provides high-resolution dose calculations based on pre-treatment imaging, direct visualization of the delivered dose relative to anatomy during irradiation remains challenging. This limitation is particularly important in anatomically moving regions, where motion can lead to discrepancies between planned and delivered dose distributions.

iRAI offers a potential approach for real-time visualization of radiation dose deposition through radiation-induced acoustic signals. However, previous iRAI studies primarily focused on dose visualization alone and did not provide concurrent anatomical information, limiting the ability to localize and interpret the measured dose within tissue structures during treatment.

To address this limitation, this chapter presents a dual-modality volumetric imaging framework that integrates iRAI with US imaging. In this framework, iRAI measures volumetric radiation dose deposition, while US provides co-registered anatomical information. By combining these two modalities, this approach enables dose-on-anatomy visualization during radiotherapy and provides a potential strategy for monitoring radiation delivery in the presence of motion. To our knowledge, this is among the first studies to demonstrate volumetric co-registered iRAI–US imaging for real-time visualization of radiation dose relative to anatomy during radiotherapy.

2.2 Materials and Methods

2.2.1 Dual-Modality iRAI–US Imaging System

Figure 2.1(a) illustrates the acquisition workflow and timing of the dual-modality iRAI–US imaging system. The system was developed by upgrading a previously established volumetric

iRAI platform designed for clinical use to enable synchronized acquisition of radiation-induced acoustic signals and US anatomical images [144].

A custom low-frequency 2D matrix array transducer (MAT) was used to receive radiation-induced acoustic signals generated by approximately 4-μs radiation pulses. As indicated by Equation (3), acoustic wave generation is governed by temporal transitions in the dose-rate profile. The measured X-ray pulse shown in Figure 2.1(b) had a separation of approximately 3.48 μs between the major positive and negative peaks in its first derivative, corresponding to a dominant frequency component on the order of 0.3 MHz. Therefore, a 2D MAT with a center frequency of 0.35 MHz was selected to approximately match the dominant frequency content of the generated radiation acoustic signals. The transducer had approximately 50% bandwidth, 1024 (32 × 32) elements, and a pitch of 3.65 mm.

For anatomical imaging, a higher-frequency 2D MAT with a center frequency of 3.5 MHz and 50% bandwidth was used, providing a balance between spatial resolution and imaging depth for soft-tissue visualization. The transducer contains 1024 (32 × 32) elements with a pitch of 0.3 mm.

The iRAI and US probes were spatially co-registered, allowing radiation dose information measured by iRAI to be directly visualized together with anatomical structures obtained from US imaging.

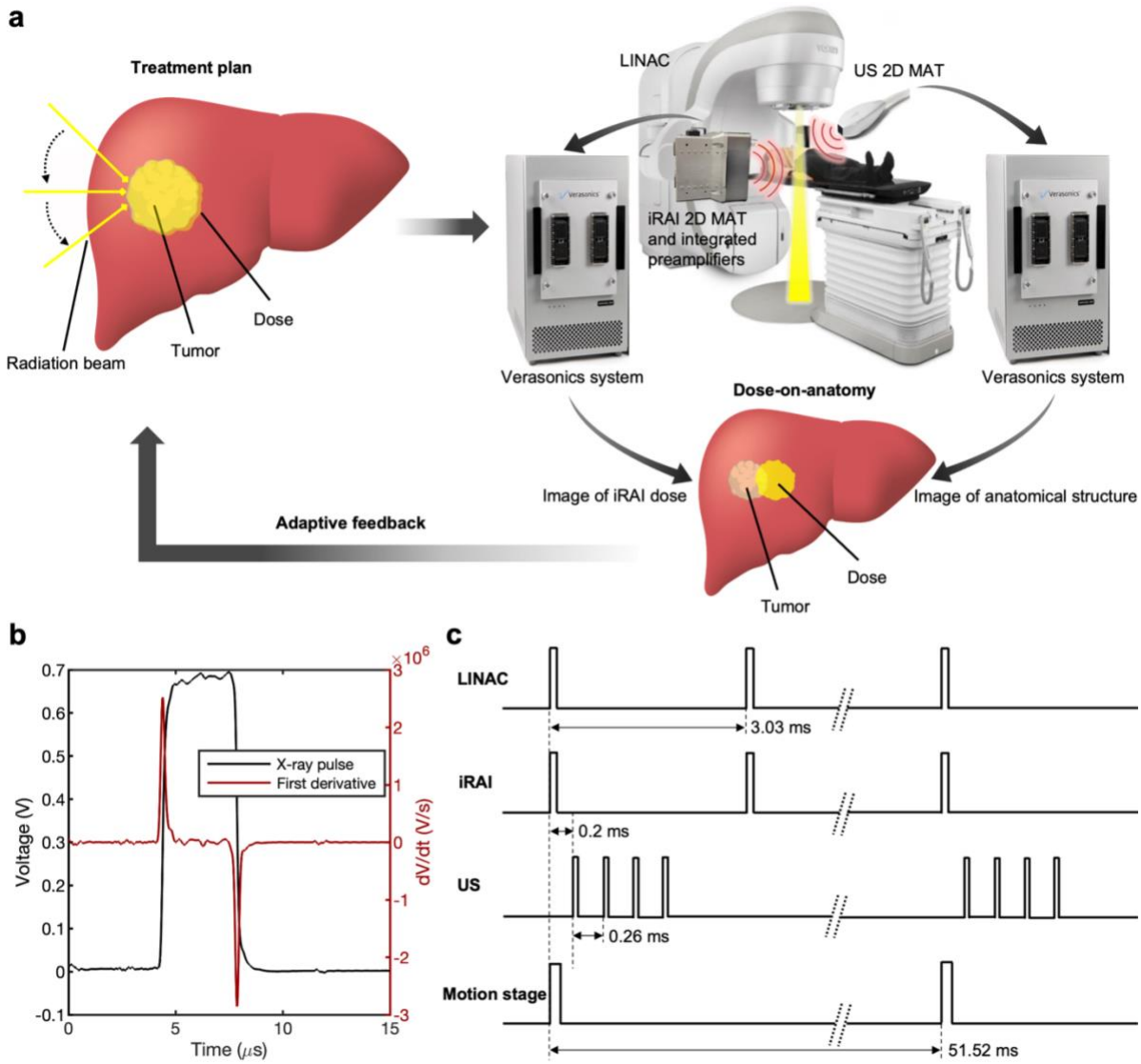


Figure 2.1 Workflow and timing of the dual-modality volumetric iRAI–US imaging system. (a) Workflow for volumetric dose-on-anatomy imaging during radiotherapy delivery. Megavoltage radiation pulses from the LINAC generate radiation-induced acoustic signals that are detected by a low-frequency 2D MAT for iRAI dose reconstruction, while a co-registered higher-frequency MAT acquires volumetric US images of anatomical structures. The reconstructed iRAI dose and US images are spatially aligned for dose-on-anatomy visualization. (b) Measured LINAC X-ray pulse profile and its first derivative. (c) Timing diagram showing coordination between LINAC triggering, iRAI acquisition, interleaved US imaging, and linear motion control.

2.2.2 Volumetric Acquisition and Synchronization

Volumetric iRAI acquisition was triggered by signals from the LINAC. Each megavoltage radiation pulse initiated an iRAI acquisition window, such that the recorded acoustic signals were temporally associated with individual radiation pulses. Due to the multiplexing scheme implemented in the front-end electronics, multiple radiation pulses were required to complete one

iRAI acquisition, and data collected over successive pulses were combined to reconstruct a volumetric dose distribution.

US imaging was temporally interleaved with iRAI acquisition to avoid cross-modality interference while maintaining temporal consistency between dose and anatomy. US transmissions were triggered 0.2 ms after each LINAC signal. Four US transmitting–receive events were acquired between two radiation pulses with a pulse repetition period of 0.26 ms. The timing sequence is illustrated in Figure 2.1(c).

For each imaging cycle, iRAI data collected over successive radiation pulses were combined to reconstruct a 3D dose map, followed by volumetric US imaging of the corresponding anatomy. Because the two modalities were spatially co-registered and temporally synchronized, the reconstructed iRAI and US volumes were inherently aligned without additional registration.

2.2.3 Characterization of Spatial Resolution

The spatial resolutions of the iRAI and US subsystems were experimentally characterized using a 0.15-mm-diameter tungsten wire target. For iRAI measurements, the wire was excited using a pulsed laser source with a wavelength of 750 nm and a pulse duration of 4 ns to generate localized acoustic signals. Laser illumination was delivered through a fiber bundle fixed relative to the wire to ensure consistent excitation conditions. For US measurements, conventional pulse–echo imaging was performed using the same tungsten wire target.

Axial and lateral resolutions were evaluated at multiple imaging depths covering the operational ranges of the two transducers. A digital positioning platform was used to place the wire at predefined depths along the central axis of each 2D MAT. For the iRAI 2D MAT, measurements were performed at depths of 10, 13, 16, 19, 22, 25, and 28 cm. For the US 2D MAT, measurements were conducted at depths of 1, 2, 3, 4, 5, 6, and 7 cm.

2.2.4 Estimation of Dose–anatomy Co-registration Error

In addition to spatial resolution, the performance of the dual-modality imaging system was evaluated by estimating the dose–anatomy co-registration error, which reflects the accuracy of dose mapping under motion conditions. The co-registration error was estimated based on the spatial resolution of the US 2D MAT and respiratory motion parameters. Two sources of uncertainty were considered: (1) the spatial resolution of the US volume used for anatomical definition and motion tracking, and (2) tissue motion occurring within one US imaging frame due

to respiration. The spatial resolution of the iRAI 2D MAT was not included in this estimate, as the iRAI array remained fixed with respect to the radiation beam during delivery and therefore did not contribute to co-registration uncertainty.

The two independent error terms were combined using a quadrature approach based on the root-sum-square method [179]. The co-registration error, denoted as ε_{reg}, was calculated as

$$\varepsilon_{reg} = \sqrt{{\varepsilon_{US}}^2 + {\varepsilon_{motion}}^2} \tag{10}$$

where ε_{US} represents the spatial resolution of the US 2D MAT, and ε_{motion} represents the tissue displacement occurring within one US imaging frame due to respiratory motion. The motion-induced tracking error was estimated as

$$\varepsilon_{motion} = v_{tissue} \cdot \Delta t_{US} = \frac{v_{tissue}}{f_{US}} \tag{11}$$

where v_{tissue} is the tissue velocity, Δt_{US} is the duration of one US frame, and f_{US} is the US volumetric frame rate.

2.2.5 Respiratory Motion–Mimicking Phantom Study

A motion-mimicking phantom study was conducted to evaluate the dose mapping accuracy of the dual-modality iRAI–US imaging system under controlled motion conditions. The experimental design considered several factors relevant to respiratory motion in radiotherapy, including motion direction, motion speed, motion range, and imaging frame rate. The overall experimental setup is shown in Figure 2.2(a), and a schematic of the transducer positioning and prescribed phantom motion is shown in Figure 2.2(b).

Tissue-mimicking phantoms were fabricated using solidified vegetable oil and mounted on a custom linear translation stage to generate repeatable one-dimensional motion. Two rectangular phantoms were prepared in 3D-printed containers with dimensions of 17 cm × 17 cm × 20 cm for lateral motion and 17 cm × 17 cm × 12.5 cm for axial motion. A 2 cm × 2 cm lard block was embedded in each phantom to provide strong echogenic contrast for motion tracking in US images. Based on reported respiratory motion characteristics in radiation oncology, motion speeds ranging from 0.5 cm/s to 4 cm/s and motion ranges from 0.5 cm to 4 cm were selected. The specific motion parameters used in the experiments are summarized in Table 2.1. Both lateral and axial motion patterns were investigated to evaluate direction-dependent effects on dose mapping accuracy.

The iRAI and US 2D MATs were positioned on opposite sides of the phantom and acoustically coupled using high-viscosity US gel. Their relative positions were calibrated using

the in-room LINAC laser alignment system to locate the beam isocenter. The initial position of the lard block was aligned to the LINAC isocenter, and a 2 cm × 2 cm square 6-MV X-ray beam was vertically aligned with the lard block location. As illustrated in Figure 2.2(c), the radiation beam was oriented perpendicular to the imaging plane.

To synchronize phantom motion with radiation delivery and imaging acquisition, a delayed LINAC trigger signal was used to drive the linear translation stage following the timing scheme described in Section 2.2.2. For the lateral and axial motion experiments, total delivered doses of 4.48 Gy over 24 s and 2.99 Gy over 16 s were applied, respectively.

Three volumetric US imaging frame rates (2.5 Hz, 4 Hz, and 10 Hz) were investigated by adjusting the number of dynamic focusing positions during acquisition. Dynamic focus counts of 4, 9, and 16 were used to achieve frame rates of 10 Hz, 4 Hz, and 2.5 Hz, respectively, as illustrated in Figure 2.3(a)–(c). Higher imaging frame rates were obtained by reducing the number of dynamic focusing positions, at the expense of spatial resolution. Each measurement was repeated three times.

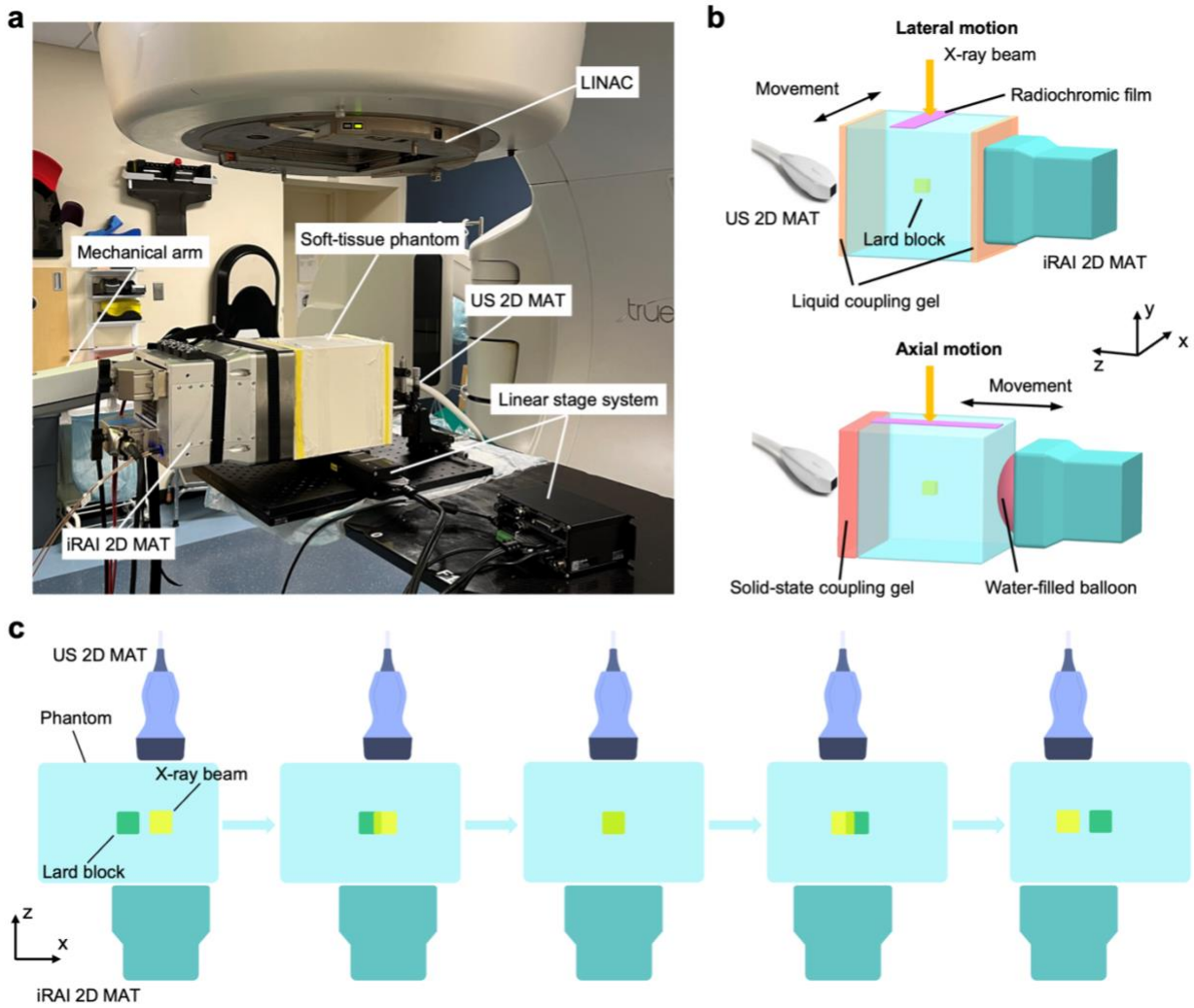


Figure 2.2 Experimental setup and schematic illustrations for the motion-mimicking phantom study. (a) Photograph of the experimental setup showing the soft-tissue phantom mounted on a linear translation stage beneath the LINAC. The iRAI and US 2D MATs were positioned on opposite sides of the phantom for synchronized acquisition during irradiation. The translation stage generated controlled lateral and axial motions. (b) Schematics of the phantom configuration, transducer positioning, and prescribed motion patterns. A lard block embedded in the phantom provided echogenic contrast for US motion tracking. The relative orientation of the X-ray beam, transducers, and motion directions is indicated. (c) Illustration of the temporal relationship between phantom motion and radiation dose deposition. As the phantom moves during irradiation, the relative position between the embedded lard block and the deposited radiation dose changes while the radiation beam remains fixed.

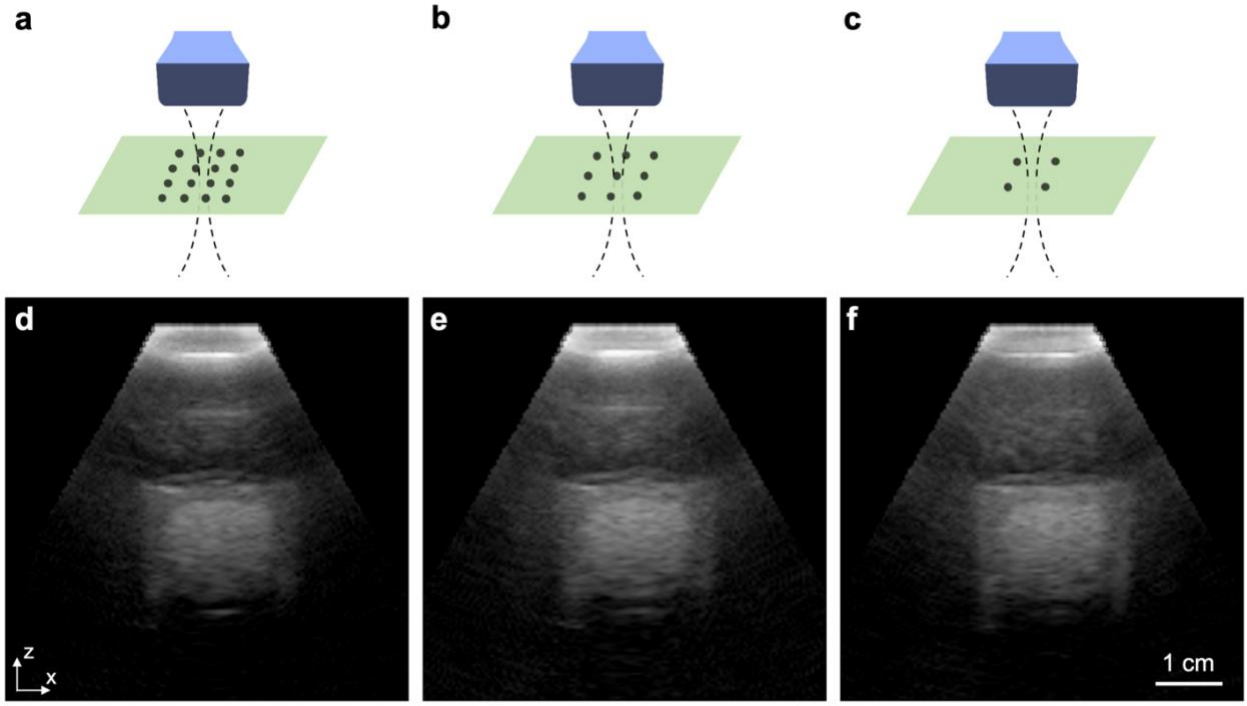


Figure 2.3 Volumetric US imaging of the motion phantom at different frame rates. (a–c) Schematic illustrations of dynamic focusing configurations of the US 2D MAT with 16, 9, and 4 focusing positions, respectively. (d–f) Representative x–z cross-sectional US images of the embedded lard block acquired at volumetric frame rates of 2.5, 4, and 10 Hz, corresponding to 16, 9, and 4 focusing positions. Reducing the number of focusing positions increases the volumetric frame rate at the expense of spatial resolution. The scale bar represents 1 cm.

2.2.6 *In Vivo* Rabbit Study

An *in vivo* rabbit experiment was conducted to demonstrate real-time dose-on-anatomy imaging using the dual-modality iRAI–US system under clinically relevant irradiation conditions. All animal procedures were approved by the University of South Florida Research Integrity and Compliance Institutional Animal Care and Use Committee under the protocol titled “Combined Radiation Acoustics and Ultrasound Imaging for Real-Time Guidance in Radiotherapy” (IS00008026).

CT simulation was performed on a female New Zealand white rabbit (4.5 kg, 6 months old; Charles River) to obtain anatomical information for treatment planning. Based on the CT images, a treatment plan was generated using a commercial TPS (RayStation 11A, RaySearch Laboratories). The plan employed an anterior-to-posterior beam configuration targeting the liver and delivered a total dose of 3.8 Gy.

The experimental setup for *in vivo* imaging is shown in Figure 2.4(a). During imaging, the iRAI and US 2D MATs were positioned on the rabbit’s body with the imaging field of view centered on the liver region. Abdominal fur was removed prior to imaging to improve acoustic

coupling. A water-filled balloon coated with US gel was used to acoustically couple the iRAI transducer to the body surface. Sagittal and coronal CT views of the rabbit anatomy together with the planned dose distribution are shown in Figure 2.4(b) and 2.4(c).

Anesthesia was induced with ketamine administered intramuscularly at 40 mg/kg and maintained using 1.5% isoflurane in oxygen. Anesthetic gas was delivered using a V-Gel airway device (J1350D, Jorgensen Laboratories) connected to a Matrix vaporizer (MidMark Corporation). Physiological parameters including heart rate, respiratory rate, oxygen saturation, and body temperature were continuously monitored using a SurgiVet Advisor vital signs monitor (Smiths Medical). Body temperature was maintained using a water-circulating heating pad (TP-700, Stryker Corporation).

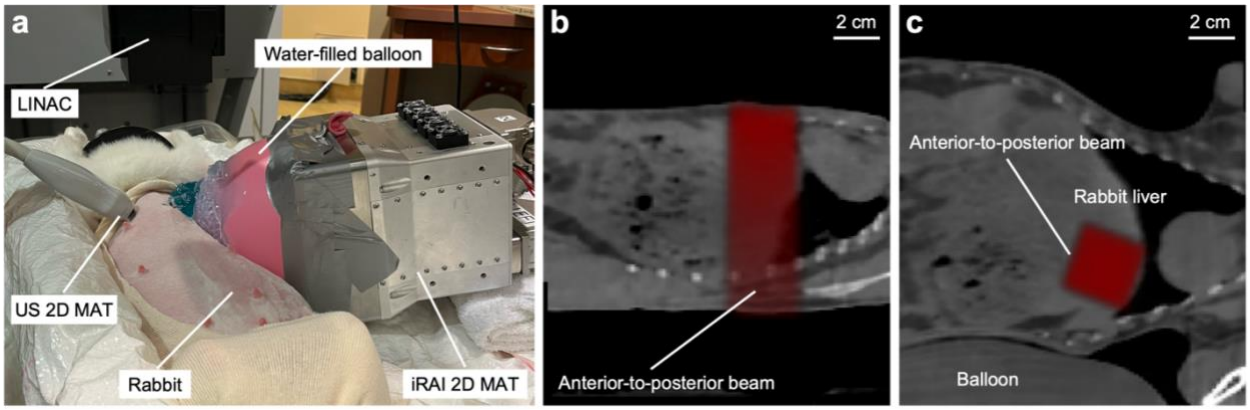


Figure 2.4 Volumetric dual-modality imaging of dose-on-anatomy in an *in vivo* rabbit model. (a) Experimental setup for the rabbit study in the radiotherapy treatment room. (b, c) Sagittal and coronal CT views of the rabbit anatomy with the planned dose distribution.

2.3 Results

2.3.1 Spatial Resolution and Dose–Anatomy Co-Registration Error

The spatial resolutions of the iRAI and US subsystems are summarized in Figure 2.5 as a function of imaging depth. For the iRAI subsystem (Figure 2.5a), the axial resolution remained relatively stable over the evaluated depth range from 10 to 28 cm, with values of approximately 2 mm. In contrast, the lateral resolution showed a clear dependence on depth and gradually degraded as depth increased.

For the US subsystem (Figure 2.5b), substantially higher spatial resolution was achieved within the shallow imaging depths relevant for anatomical visualization. The axial resolution remained approximately constant at about 0.5 mm over depths from 1 to 7 cm, while the lateral

resolution gradually degraded with depth, with the best resolution achieved near the transducer surface.

The co-registration error was estimated from two sources. First, based on a representative human respiratory frequency of 0.27 Hz and an average liver displacement amplitude of 8 mm [180], the average tissue motion velocity was estimated to be approximately 2.1 mm/s. At the highest volumetric ultrasound frame rate of 10 Hz used in this study, the corresponding motion-induced tracking error was calculated to be approximately 0.21 mm. Second, the optimal axial resolution of the ultrasound subsystem was measured to be 0.40 mm. Assuming these errors were independent, they were combined in quadrature, resulting in an estimated dose–anatomy co-registration error of approximately 0.45 mm.

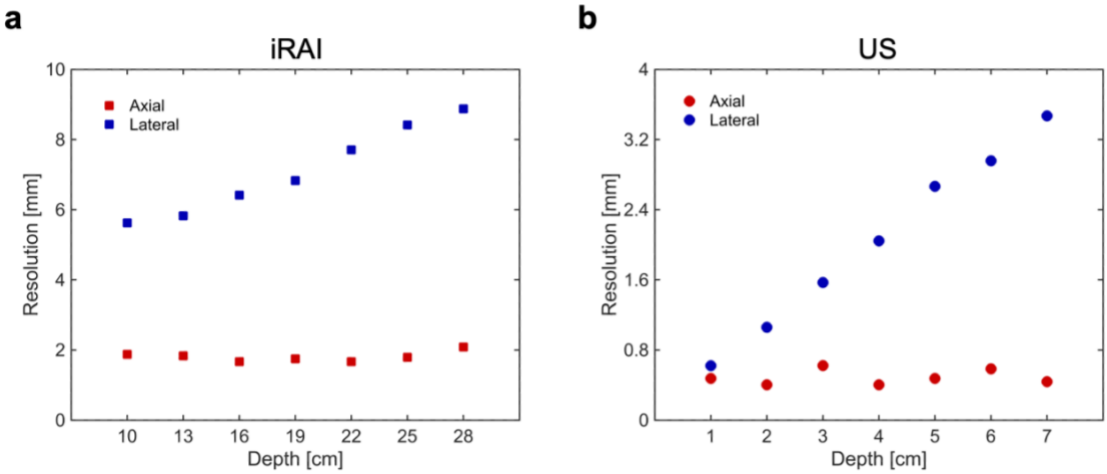


Figure 2.5 Spatial resolution of the iRAI and US imaging systems measured using a 0.15-mm-diameter tungsten wire target. (a) Axial and lateral resolutions of the iRAI system as a function of imaging depth. (b) Axial and lateral resolutions of the US system as a function of imaging depth.

2.3.2 Temporal Dose Visualization and Motion-Induced Dose–Anatomy Mismatch

Figure 2.6 presents representative time-resolved volumetric imaging results from the motion-mimicking phantom experiments, illustrating the relative behavior of anatomical motion and radiation dose deposition. Cross-sectional x–z US images, corresponding iRAI dose images, and fused dose-on-anatomy images are shown over a 2 s acquisition window for both lateral and axial motion scenarios.

Volumetric iRAI reconstruction captured radiation dose deposition within the tissue-mimicking phantom. The reconstructed dose distribution remained spatially stationary with respect to the beam isocenter throughout the imaging period, consistent with the fixed geometry of the

radiation beam. After envelope-based processing, a continuous dose distribution corresponding to the irradiated field was obtained.

In contrast, the simultaneously acquired US images clearly visualized the embedded lard block and its motion within the phantom. As shown in Figure 2.6a, the phantom translated along the lateral direction, while in Figure 2.6b motion occurred along the axial direction. In both cases, the US image sequences show clear displacement of the lard block over time, whereas the iRAI dose images exhibit minimal apparent motion.

By fusing the temporally synchronized iRAI and US volumes using the pre-calibrated relative positions of the two MATs, radiation dose deposition can be visualized directly on the moving anatomical structure without additional registration. The fused images reveal time-varying spatial offsets between the target position and the deposited dose under motion conditions.

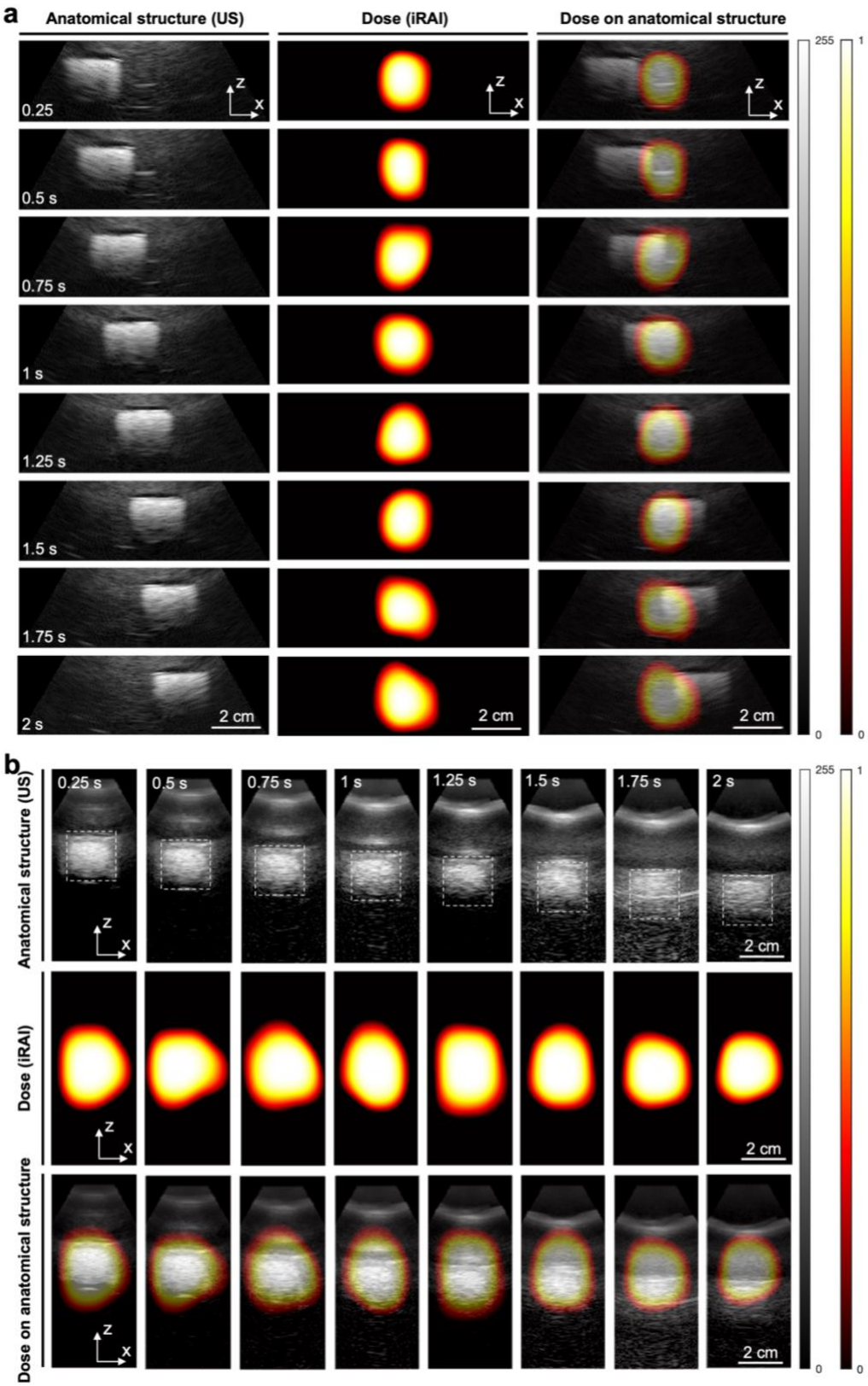

a
Anatomical structure (US)
Dose (iRAI)
Dose on anatomical structure
0.25
0.5 s
0.75 s
1 s
1.25 s
1.5 s
1.75 s
2 s
2 cm
255
0
1
0
b
Anatomical structure (US)
Dose (iRAI)
Dose on anatomical structure
0.25 s
0.5 s
0.75 s
1 s
1.25 s
1.5 s
1.75 s
2 s
2 cm
255
0
1
0

Figure 2.6 Temporal dose-on-anatomy visualization in motion-mimicking phantom experiments. (a) Time-resolved x–z cross-sectional US images of the tissue-mimicking phantom with an embedded lard block (left), corresponding iRAI dose images (middle), and fused dose-on-anatomy images (right) acquired over a 2 s interval during lateral motion. The phantom moved back and forth along the lateral direction while the radiation beam remained fixed relative to the imaging geometry. (b) Corresponding image sequences acquired during axial motion of the phantom. In both motion scenarios, the US images show continuous displacement of the lard block, whereas the iRAI dose images remain spatially stationary relative to the beam isocenter. The fused images show the relative displacement between the anatomical structure and the deposited dose over time.

2.3.3 Dose Accumulation Mapping with US-Guided Motion Correction

To estimate dose accumulation on a moving target, iRAI dose images were aligned frame by frame using motion information extracted from the co-registered US volumes. Figure 2.7(a) shows representative x–z cross-sectional iRAI images without motion correction during a lateral motion experiment (2 cm/s, 4 cm range). Frames are displayed every 0.25 s over a 2 s interval, consistent with the effective 4 Hz imaging rate. Without ultrasound-based motion tracking, dose accumulation is reconstructed assuming a fixed beam position relative to the phantom. Figure 2.7(b) shows the corresponding images after motion correction under the same conditions. After motion correction, the accumulated dose forms a more spatially consistent distribution along the motion direction, reflecting cumulative dose deposition relative to the moving target.

Figure 2.7(c) compares motion-corrected iRAI dose maps with radiochromic film measurements for lateral motion at a fixed speed of 2 cm/s and motion ranges of 1, 2, 3, and 4 cm. Film dose maps extracted from a 2 cm × 6 cm region show increasing elongation along the motion direction as the motion range increases. The corresponding iRAI dose maps exhibit more similar spatial extent and overall shape compared to the uncorrected iRAI dose maps. Figure 2.7(d) presents analogous results for axial motion at a speed of 1 cm/s with motion ranges of 0.5, 1, 1.5, and 2 cm, demonstrating consistent agreement between film and iRAI measurements across different motion directions.

As illustrated in Figure 2.7(e), dose profiles were extracted along a central line through the dose distribution. The resulting profiles for lateral and axial motion are shown in Figure 2.7(f) and Figure 2.7(g), respectively. In both cases, the motion-corrected iRAI profiles closely follow the film-based profiles. For a fixed motion speed, the agreement between iRAI and film measurements improves as the motion range increases, indicating increased averaging of dose deposition over larger motion amplitudes.

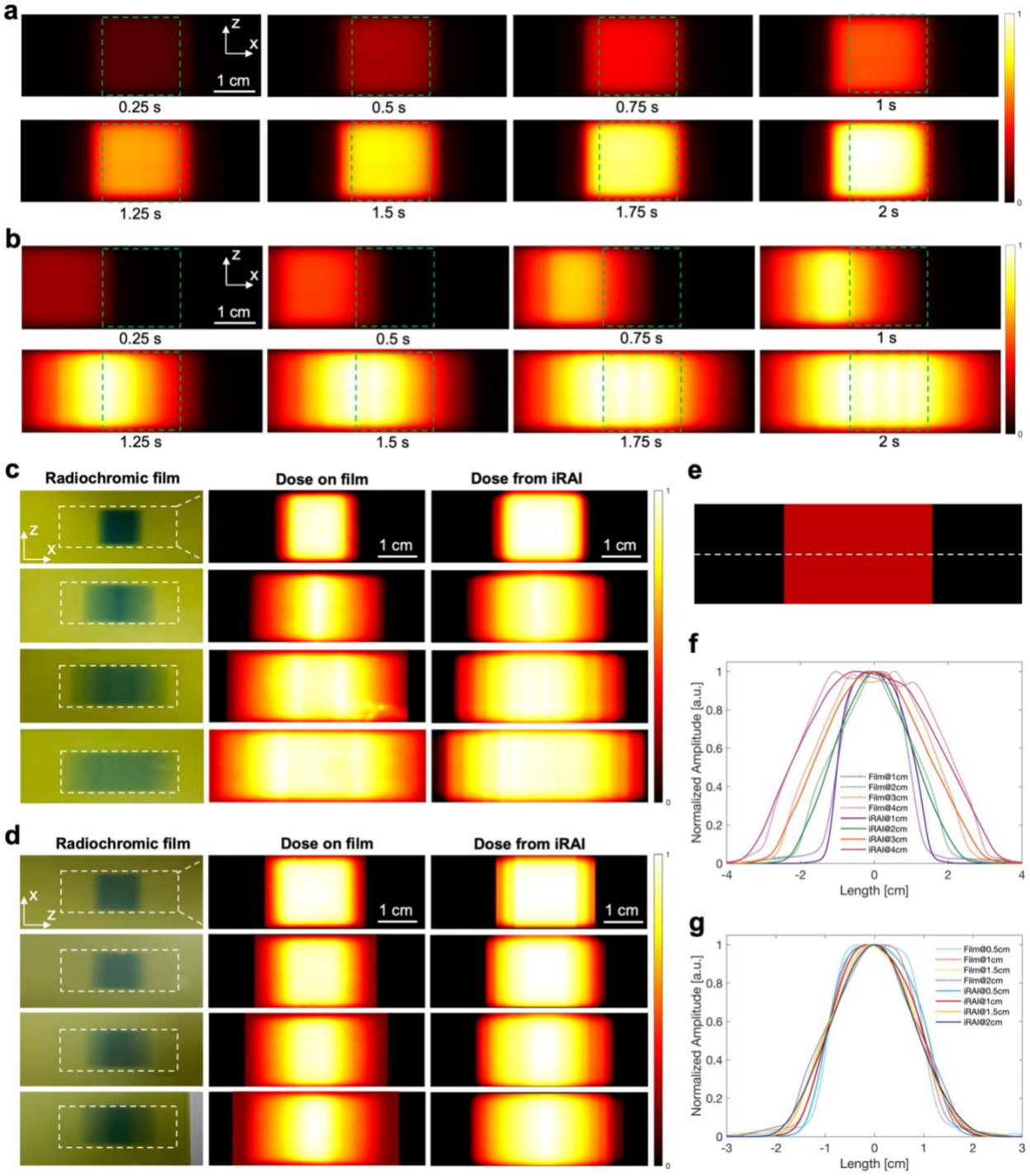


Figure 2.7 (a) Representative x–z cross-sectional iRAI images of temporal dose accumulation across the beam isocenter without ultrasound-guided motion correction during lateral phantom motion (2 cm/s, 4 cm range). Frames are shown every 0.25 s over 2 s. Pixel intensities are normalized to [0, 1], and green dashed boxes indicate the tracked lard block position. (b) Representative x–z cross-sectional iRAI images of temporal dose accumulation across the beam isocenter with ultrasound-guided motion correction, under the same conditions as in (a). (c) Comparison between radiochromic film measurements and motion-corrected iRAI dose maps for lateral motion (2 cm/s) with ranges of 1–4 cm. Film dose maps were extracted from a 2 cm × 6 cm region. (d) Corresponding comparison for axial motion (1 cm/s) with ranges of 0.5–2 cm. (e) Schematic of the central line used for dose profile extraction. (f, g) Dose profiles along the indicated line for the lateral (c) and axial (d) cases. Dashed lines: film; solid lines: iRAI. All profiles are normalized.

2.3.4 Quantitative Accuracy of Dose Mapping

Agreement between film dose maps and iRAI-based dose maps was quantified using the structural similarity index measure (SSIM) [181] and gamma index analysis [182], reported as the gamma passing rate (GPR) under 3% dose difference and 3 mm distance-to-agreement criteria. Motion speed, motion range, and US volumetric frame rate were treated as key variables. Table 2.1 reports the mean and standard deviation from three repeated acquisitions for each condition.

Results obtained with US-based motion correction were compared with standalone iRAI results without correction. Without real-time motion tracking, the analysis assumes that the target remains stationary, so the reconstructed dose accumulates at a fixed location. This assumption resulted in large mismatches relative to film measurements when the phantom moved. With motion correction, both SSIM and GPR increased across all tested scenarios.

Consistent trends were observed after motion correction. At fixed frame rate and speed, larger motion ranges produced higher SSIM and GPR values. At fixed frame rate and motion range, higher motion speeds reduced both metrics. At fixed motion speed and range, higher US frame rates improved the agreement. The largest improvement occurred for lateral motion at 1 cm/s over a 4 cm range with a 4 Hz US frame rate, where SSIM increased by 0.5065 and GPR increased by 74.60%. In most cases after motion correction, GPR exceeded 90%, and the variability across repeated measurements remained low (standard deviation up to 0.0064 for SSIM and 1.34% for GPR).

Table 2.1 Comparison of dose mapping accuracy with and without ultrasound-based motion correction across different motion scenarios.

Motion parameter				**Quantitative metrics**					
Direction	**Frame rate [Hz]**	**Speed [cm/s]**	**Range [cm]**	**SSIM [a.u.]**			**GPR [a.u.]**		
				Without correction	**With correction**	**Improvement**	**Without correction**	**With correction**	**Improvement**
Lateral	4	2	1	0.7783 ± 0.0057	0.8573 ± 0.0064	0.0790	65.60% ± 2.92%	90.48% ± 0.53%	24.88%
			2	0.6469 ± 0.0494	0.8793 ± 0.0042	0.2324	49.29% ± 2.39%	91.57% ± 0.34%	42.28%
			3	0.5529 ± 0.0525	0.9020 ± 0.0026	0.3491	36.48% ± 1.36%	93.11% ± 0.27%	56.63%
			4	0.4804 ± 0.0362	0.9213 ± 0.0023	0.4409	28.81% ± 1.13%	95.37% ± 0.21%	66.56%
	4	1	4	0.4365 ± 0.0290	0.9430 ± 0.0017	0.5065	22.09% ± 1.47%	96.69% ± 0.13%	74.60%
		2		0.4804 ± 0.0362	0.9213 ± 0.0023	0.4409	28.81% ± 1.13%	95.38% ± 0.21%	66.57%
		3		0.4734 ± 0.0839	0.9060 ± 0.0026	0.4326	22.33% ± 1.32%	93.61% ± 0.27%	71.28%
		4		0.5135 ± 0.0370	0.8867 ± 0.0031	0.3732	28.17% ± 2.05%	92.08% ± 0.47%	63.91%

	2.5	2	4	0.4971 ± 0.0677	0.9062 ± 0.0005	0.4091	31.19% ± 1.89%	92.46% ± 0.11%	66.57%
	4			0.4804 ± 0.0362	0.9213 ± 0.0023	0.4409	28.81% ± 1.13%	95.38% ± 0.21%	61.27%
	10			0.4827 ± 0.0410	0.9366 ± 0.0003	0.4539	31.82% ± 2.60%	96.13% ± 1.28%	66.57%
Axial	4	1	0.5	0.8384 ± 0.0134	0.8599 ± 0.0013	0.0215	81.03% ± 6.15%	85.97% ± 1.34%	64.31%
			1	0.8173 ± 0.0268	0.8676 ± 0.0008	0.0503	65.93% ± 4.45%	87.49% ± 0.35%	4.94%
			1.5	0.7694 ± 0.0269	0.8793 ± 0.0035	0.1099	55.84% ± 0.96%	88.15% ± 0.18%	22.00%
			2	0.7079 ± 0.0476	0.8911 ± 0.0007	0.1832	44.73% ± 4.19%	90.30% ± 0.55%	12.91%
	4	0.5	2	0.7195 ± 0.0531	0.9105 ± 0.0004	0.1910	46.14% ± 3.27%	91.48% ± 0.56%	33.03%
		1		0.7079 ± 0.0476	0.8911 ± 0.0007	0.1832	44.73% ± 4.19%	90.30% ± 0.55%	22.74%
		1.5		0.7414 ± 0.0283	0.8829 ± 0.0017	0.1415	43.53% ± 2.75%	89.27% ± 0.47%	44.41%
		2		0.7009 ± 0.0215	0.8646 ± 0.0023	0.1637	48.57% ± 2.27%	87.41% ± 0.57%	43.53%
	2.5	1	2	0.7073 ± 0.0203	0.8668 ± 0.0017	0.1595	44.13% ± 3.29%	87.54% ± 0.19%	42.68%
	4			0.7079 ± 0.0476	0.8911 ± 0.0007	0.1832	44.73% ± 4.19%	90.30% ± 0.55%	24.88%
	10			0.7473 ± 0.0316	0.9212 ± 0.0014	0.1739	48.15% ± 1.52%	92.58% ± 0.38%	42.28%

2.3.5 *In Vivo* Dose-on-Anatomy Imaging in a Rabbit Liver Model

The *in vivo* rabbit experiment demonstrated dose-on-anatomy imaging under respiratory motion. During irradiation, iRAI dose volumes and US anatomy volumes were fused and co-registered to the on-board CT based on anatomical landmarks and the known relative positions of the probes and the rabbit.

Figure 2.8(a) shows time-resolved image sequences in sagittal and coronal views. In these images, iRAI dose is displayed in red, US anatomy in yellow, and the CT-derived liver boundary is overlaid in light blue. The sequences show that respiratory motion introduces time-varying misalignment between the deposited dose and the intended target region.

Figure 2.8(b) presents three representative 3D fusion snapshots at 1 s, 10 s, and 19 s during irradiation, combining CT-derived liver structure with the co-registered US and iRAI volumes. The full 20 s volumetric dose-on-anatomy result is provided as a supplementary video.

In this experiment, iRAI signals were averaged over 100 radiation pulses, resulting in an effective frame rate of 3 Hz. A separate US B-mode sequence further visualized respiratory-induced tissue motion in a sagittal view, with arrows indicating liver displacement during respiration.

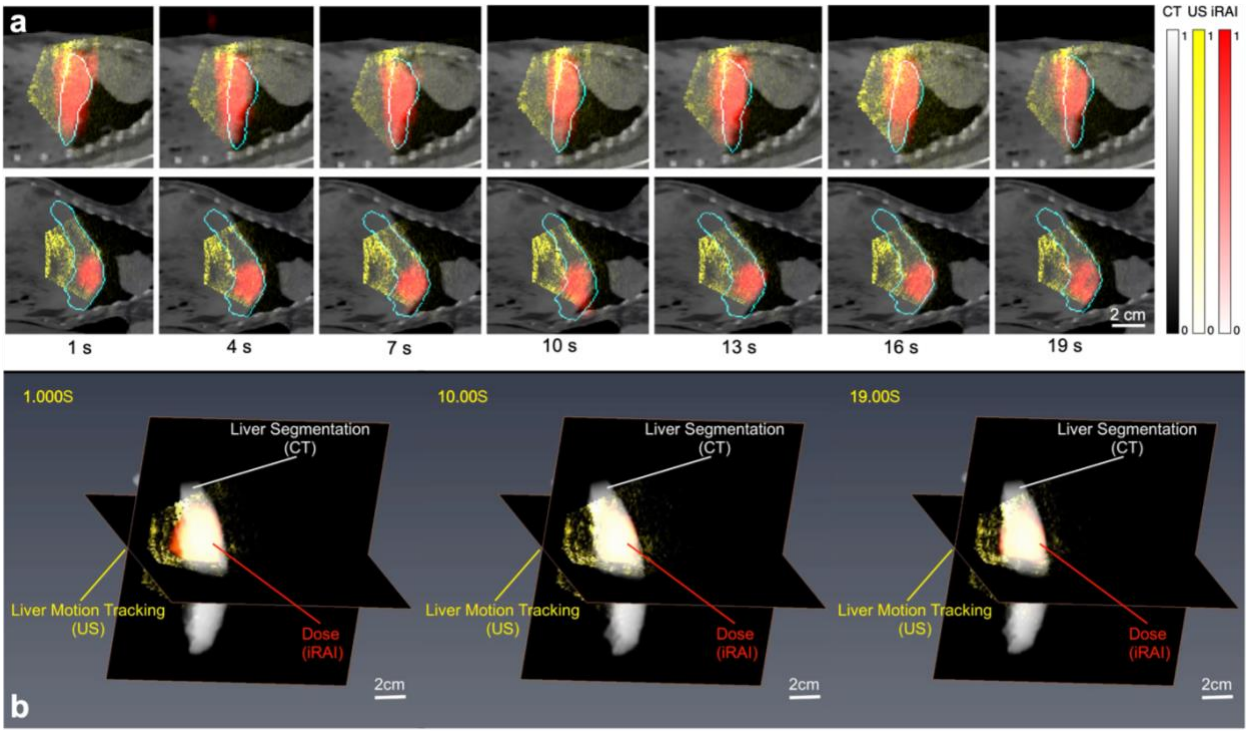


Figure 2.8 Volumetric dose-on-anatomy imaging in an *in vivo* rabbit liver model under respiratory motion. (a) Time-resolved multimodality image sequences in sagittal (top row) and coronal (bottom row) views acquired during irradiation. iRAI-derived dose is overlaid in red, US anatomy is shown in yellow, and the CT-derived liver boundary is outlined in light blue. Frames at selected time points during a 20 s delivery period illustrate respiration-induced liver motion and the resulting variation in dose–anatomy alignment. (b) 3D fusion images at the 1st, 10th, and 19th seconds of irradiation, combining CT-based liver segmentation with co-registered US anatomy and iRAI dose.

2.4 Discussion and Conclusions

This chapter presents a volumetric dual-modality imaging framework for visualizing radiation dose relative to anatomical structures during treatment. By combining iRAI-based dose reconstruction with US-based motion tracking, the spatial relationship between deposited dose and moving anatomy can be evaluated in real time. Phantom experiments demonstrate that incorporating US-derived motion information for frame-by-frame dose remapping substantially improves dose mapping accuracy compared with standalone iRAI, as confirmed by SSIM and gamma analysis. An *in vivo* rabbit experiment further illustrates that respiratory motion introduces time-varying misalignment between delivered dose and target anatomy.

Despite these advances, quantitative interpretation of iRAI signal amplitude remains limited. The reconstructed signal depends not only on local radiation energy deposition but also on spatially varying transducer sensitivity and system response. As a result, the current implementation primarily provides relative dose information. Achieving accurate absolute dose quantification will require system calibration and compensation for sensitivity-related variations.

Overall, this chapter demonstrates the feasibility of real-time volumetric dose-on-anatomy imaging under motion. Building on this spatial framework, the next chapter focuses on improving quantitative accuracy through transducer sensitivity compensation.

Chapter 3 Towards Quantitative iRAI Using Transducer Sensitivity Compensation

3.1 Introduction

Quantitative dose mapping has not yet been realized by current iRAI technology. Current reconstructed iRAI images primarily reflect the relative spatial distribution of deposited radiation dose rather than absolute dose values. However, quantitative dose measurement is important for radiotherapy applications because it could enable more reliable treatment verification, facilitate direct comparison with TPS dose distributions, and potentially support adaptive radiotherapy workflows in the future. Several factors still limit fully quantitative iRAI, including uncertainties in acoustic propagation and modeling, tissue heterogeneity, imperfect knowledge of acoustic properties, transducer-dependent detection nonuniformity, and the lack of absolute calibration between iRAI signal amplitude and absorbed dose.

One important limitation of conventional iRAI reconstruction is that it does not account for spatial variations in the receiving sensitivity of the US transducer. Compared with other factors, transducer sensitivity nonuniformity represents a system-dependent effect that can be experimentally characterized and computationally compensated. Because transducer sensitivity varies with depth and lateral position, voxels receiving the same deposited dose can produce different reconstructed signal amplitudes solely due to differences in detection efficiency. As a result, reconstructed iRAI amplitudes do not directly correspond to the actual deposited dose distribution. These sensitivity nonuniformities arise from multiple system-related effects, including element directivity, finite aperture effects, frequency-dependent system response, and reconstruction-dependent nonuniformity associated with delay-and-sum beamforming [183, 184].

To address this limitation, this chapter develops a transducer sensitivity compensation strategy for iRAI reconstruction. The spatial detection sensitivity of the transducer is characterized through experimental measurements and numerical simulations, and voxel-wise compensation factors are incorporated into the volumetric reconstruction process. This approach aims to reduce

sensitivity-induced bias and improve the fidelity of 3D dose distribution mapping. Although not sufficient to achieve fully quantitative iRAI, it represents an important step toward that goal.

3.2 Materials and Methods

3.2.1 Transducer Detection Sensitivity Characterization

In this study, a 2D MAT driven by a Verasonics Vantage system was used for volumetric iRAI acquisition. To quantify spatial variations in receiving sensitivity, the transducer response was experimentally characterized in a homogeneous medium. A 532 nm pulsed laser (GLPM-10, IPG Photonics, Inc.) with a pulse duration of 4 ns and a repetition rate of 500 Hz was used to generate broadband photoacoustic signals. The laser output was delivered through a 600 μm-core optical fiber (FT600EMT, Thorlabs, Inc.). The distal end of the fiber was coated with a UV-curable adhesive to form a hemispherical tip and subsequently coated with a thin gold layer, forming a localized spherical acoustic source upon laser excitation. A spherical acoustic source was positioned at known locations within a predefined 3D region, as illustrated in Figure 3.1(a). Signals were recorded across the full aperture and reconstructed using a 3D delay-and-sum (DAS) algorithm. For each source location, the maximum reconstructed amplitude was extracted to represent the local detection sensitivity. By scanning the source throughout the imaging volume, a 3D sensitivity map was obtained.

To verify that the laser-induced acoustic source can serve as an approximately ideal source for sensitivity characterization, the generated acoustic signals were measured using both a broadband hydrophone and the 2D MAT. The hydrophone measurement was used as a reference for the source spectrum, while the transducer measurement reflects the convolution of the source and transducer responses. Deconvolution of the transducer signal with the hydrophone measurement isolates the intrinsic frequency response of the transducer, as shown in Figure 3.1(c). The source spectrum is broadband, the transducer measurement is band-limited, and the deconvolved spectrum recovers the intrinsic transducer response, supporting the assumption that the source can be treated as ideal for sensitivity characterization.

To validate the experimentally measured sensitivity distribution, numerical simulations were performed using the Field II MATLAB toolbox (Version 3.30), based on the geometric parameters of the 2D MAT. The simulation configuration is shown in Figure 3.1(b). A 3D region of 15 × 15 × 25 cm^3, consistent with the experimental measurement space, was defined. Based on

the acoustic reciprocity principle in linear, time-invariant systems, the transmitting field of the array is equivalent to its receiving sensitivity under identical geometric and frequency conditions [185, 186]. Therefore, the simulated transmitting field can be used to represent the spatial variation in receiving sensitivity.

A dynamic focusing strategy was implemented to emulate volumetric traversal without physically moving an acoustic source. The receive focus of the array was electronically steered across the defined region by adjusting the focal angles in both the azimuth and elevation directions. The azimuth and elevation angles were swept from 0° to 180° with a step size of 0.5°. For each focusing event, the transmitting acoustic field of the array was computed. At each voxel within the simulated volume, the maximum amplitude across all computed fields was selected to represent the receiving sensitivity at that location. By sweeping the receive focus throughout the volume, this approach reproduces the spatial traversal performed in the experiment and generates a volumetric sensitivity map primarily determined by array geometry and element directivity.

In addition, DVH analysis was used to compare the experimentally measured and simulated 3D sensitivity maps. The cumulative volume percentage was calculated as a function of normalized sensitivity amplitude, allowing quantitative comparison of the overall volumetric sensitivity distributions.

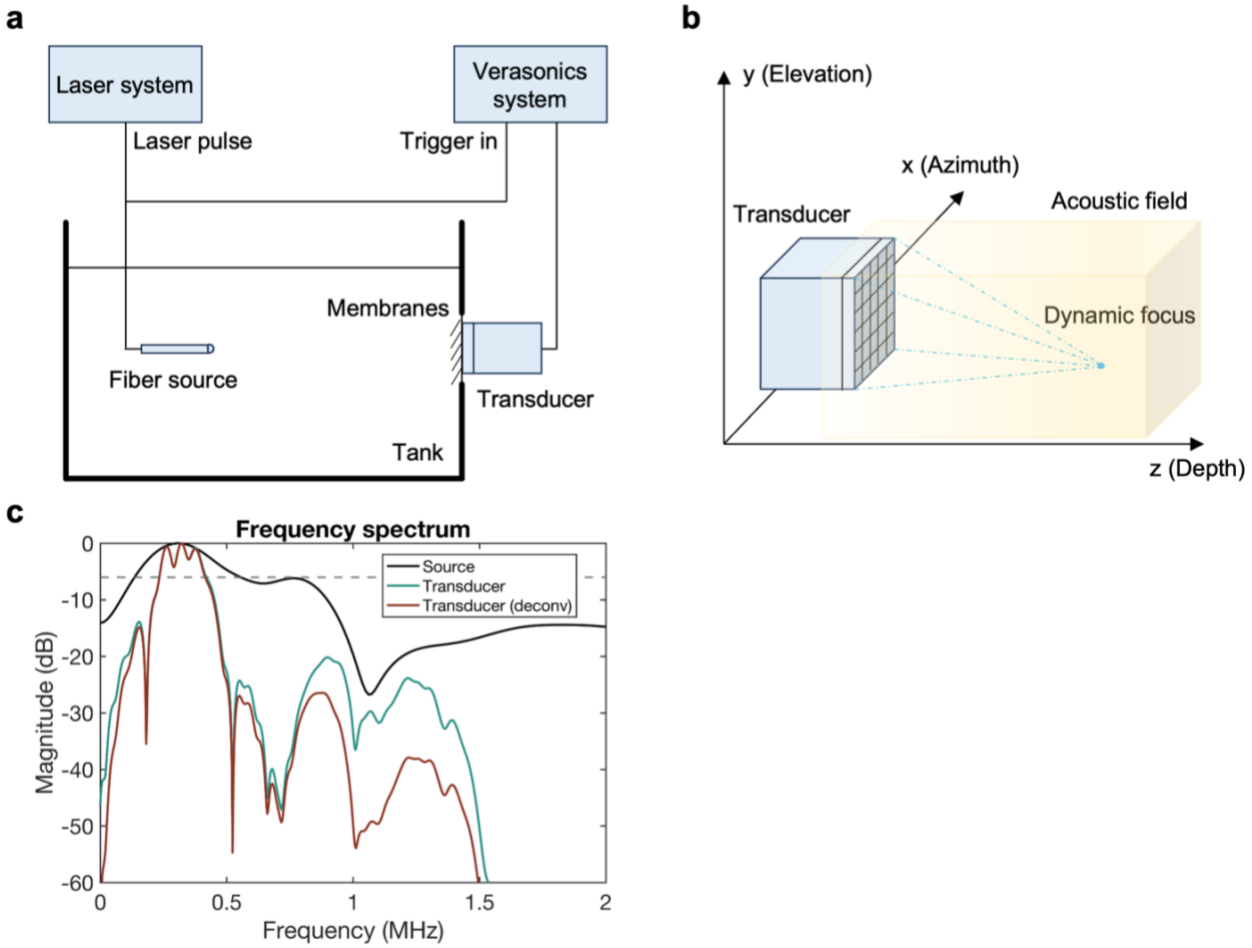


Figure 3.1 Detection sensitivity characterization of the 2D MAT. (a) Block diagram of the experimental setup used to measure the detection sensitivity of the 2D MAT. (b) Schematic of the numerical simulation used to estimate detection sensitivity using the Field II MATLAB toolbox. (c) Frequency spectra of the laser-induced acoustic source (measured by a hydrophone), the transducer measurement, and the deconvolved transducer response.

3.2.2 Radiation Beam Evaluation in a Homogeneous Phantom

To evaluate the influence of spatial detection sensitivity on iRAI reconstruction, experiments were conducted using a homogeneous soft-tissue phantom. The experimental configuration is shown in Figure 3.2(a). A clinical LINAC (TrueBeam, Varian Medical Systems) delivered megavoltage X-ray beams to irradiate a rectangular phantom composed of solidified vegetable oil enclosed in a biopolymer container (17 cm × 17 cm × 20 cm). After mixing with an oil solidifier (FRYAWAY Inc.), the vegetable oil formed a solid medium with a density of approximately 920 kg/m³ and a sound speed of approximately 1445 m/s. The 2D MAT was attached to one side of the phantom and acoustically coupled using US gel to capture radiation-induced acoustic signals during beam delivery.

The LINAC operated at a dose rate of 1400 MU/min (1 MU = 0.8 cGy) with a pulse repetition rate of 330 Hz, delivering a total dose of 2.26 Gy per measurement. Representative beam delivery configurations are illustrated in Figure 3.2(b–c).

For depth-dependent measurements, X-ray beams with a field size of 1 cm × 1 cm were delivered along the central axis at distances of 5, 7, 9, 11, 13, 15, and 17 cm from the transducer surface. To evaluate lateral response, seven lateral positions separated by 2 cm were targeted at a depth of 11 cm using the same beam configuration.

To examine the effect of beam size on iRAI reconstruction, square X-ray beams with field sizes of 1 × 1 cm², 2 × 2 cm², 3 × 3 cm², 4 × 4 cm², and 5 × 5 cm² were delivered at a fixed depth of 11 cm. Each beam configuration was repeated three times to ensure measurement consistency.

Corresponding simulations were performed using the k-Wave under matched geometric conditions. Radiation-induced acoustic sources were defined according to the planned beam geometries, enabling direct comparison between simulated and experimental datasets.

To obtain reference dose distributions, the delivered X-ray beams were measured using radiochromic films (EBT3, Ashland Inc.), which are widely used for dosimetry validation.

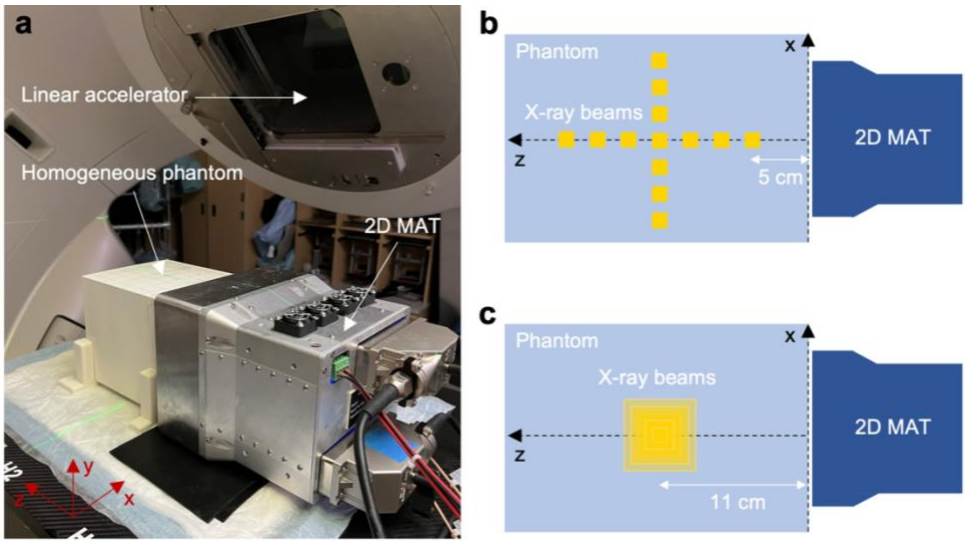


Figure 3.2 Experimental setup for the radiation beam study. (a) Photograph of the X-ray beam imaging experiment conducted in the radiotherapy treatment room. (b) Schematic illustrating X-ray beams delivered along the central axis of the homogeneous phantom at 2 cm intervals from the transducer surface. At a depth of 11 cm, six additional lateral beam positions were delivered with 2 cm spacing. Each beam had a field size of 1 cm × 1 cm. (c) Schematic illustrating X-ray beams with different field sizes (1 × 1 cm², 2 × 2 cm², 3 × 3 cm², 4 × 4 cm², and 5 × 5 cm²) delivered to a fixed depth of 11 cm along the central axis.

3.2.3 Clinical Treatment Plan Evaluation

To evaluate the performance of sensitivity compensation under spatially complex dose distributions, a phantom experiment was conducted using a C-shaped radiotherapy treatment plan.

The experimental setup is shown in Figure 3.3(a). A cylindrical homogeneous soft-tissue phantom was scanned using CT for treatment planning. Based on the CT images, a treatment plan was generated using a commercial TPS (Varian Medical Systems), with a prescribed maximum dose of 21.6 Gy.

Representative axial, coronal, and sagittal views of the treatment plan are presented in Figure 3.3(b–d), illustrating the spatial structure of the C-shaped dose distribution within the phantom volume. During irradiation, the phantom was positioned in the treatment room and aligned using the in-room laser guidance system such that the beam isocenter coincided with the geometric center of the phantom.

The 2D MAT was acoustically coupled to one side of the phantom using US gel to capture radiation-induced acoustic signals during beam delivery. Volumetric iRAI data were reconstructed from the acquired signals and compared with the CT-based treatment plan, which served as the reference dose distribution for subsequent quantitative evaluation.

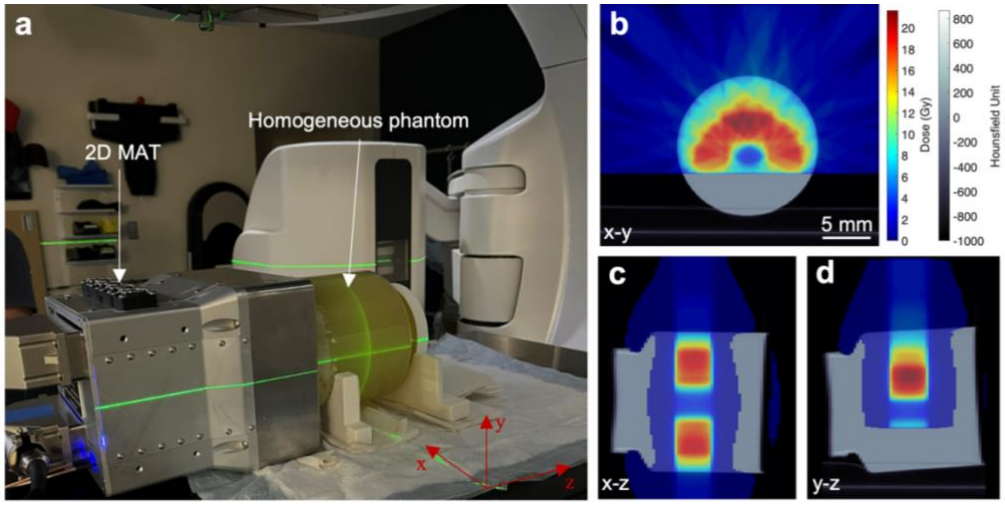


Figure 3.3 Experimental setup and treatment plan for the clinical phantom study. (a) Photograph of the phantom positioning and irradiation setup in the radiotherapy treatment room. (b–d) Axial (x–y), coronal (x–z), and sagittal (y–z) cross-sectional views of the treatment plan. Gray regions represent CT images, and the heatmaps indicate the planned dose distribution.

3.2.4 Data Processing and Quantification

Raw iRAI data from both experimental measurements and numerical simulations were reconstructed using a 3D DAS algorithm implemented in MATLAB. Detection sensitivity compensation was applied after reconstruction using voxel-wise correction factors defined as the reciprocal of the normalized detection sensitivity map. Correction factors derived from

experimentally measured and simulated sensitivity maps were applied to their corresponding datasets.

For radiation beam experiments in the homogeneous phantom, reconstructed image amplitudes were normalized prior to analysis. Voxels within the irradiated region were averaged to obtain representative amplitudes for each beam position. To analyze beams with different field sizes, depth-dependent dose profiles were extracted along the central axis of the reconstructed volumes.

For the clinical treatment plan study, reconstructed iRAI volumes were compared with the corresponding treatment plan dose distribution. Quantitative evaluation was performed using isodose line comparison, SSIM, and gamma index analysis with 5% dose-difference and 5 mm distance-to-agreement (DD/DTA) criteria.

Dose–volume histograms (DVH) were also computed to compare volumetric dose distributions between reconstructed iRAI images and the reference treatment plan. DVH curves describe the relationship between relative dose level and the fraction of volume receiving that dose or higher, enabling volumetric comparison of dose distributions [187, 188].

All image amplitudes were normalized prior to quantitative comparison to ensure consistent evaluation of relative agreement between reconstructed iRAI results and the reference dose distributions.

3.3 Results

3.3.1 Transducer Detection Sensitivity and Correction Factors

The experimentally measured and Field II–simulated volumetric detection sensitivity maps are shown in Figure 3.4(a). The experimental map exhibits a depth-dependent sensitivity distribution, with higher responses near the effective focal region at approximately 15 cm from the transducer surface and progressively reduced sensitivity toward peripheral and deeper regions.

The simulated sensitivity map presents a more symmetric spatial pattern, reflecting the idealized acoustic conditions assumed in the simulation. Although absolute amplitudes differ between the experimental and simulated results, the overall spatial trends are consistent, including reduced responses at off-axis locations and depth-dependent variations.

The corresponding DVH curves are presented in Figure 3.4(b). Both the experimental and simulated sensitivity maps exhibit similar cumulative distributions, with approximately 80% of the imaging volume showing relative sensitivity greater than 0.5 a.u.

Voxel-wise correction factors were computed as the reciprocal of the normalized sensitivity maps and applied in the subsequent sensitivity compensation procedure.

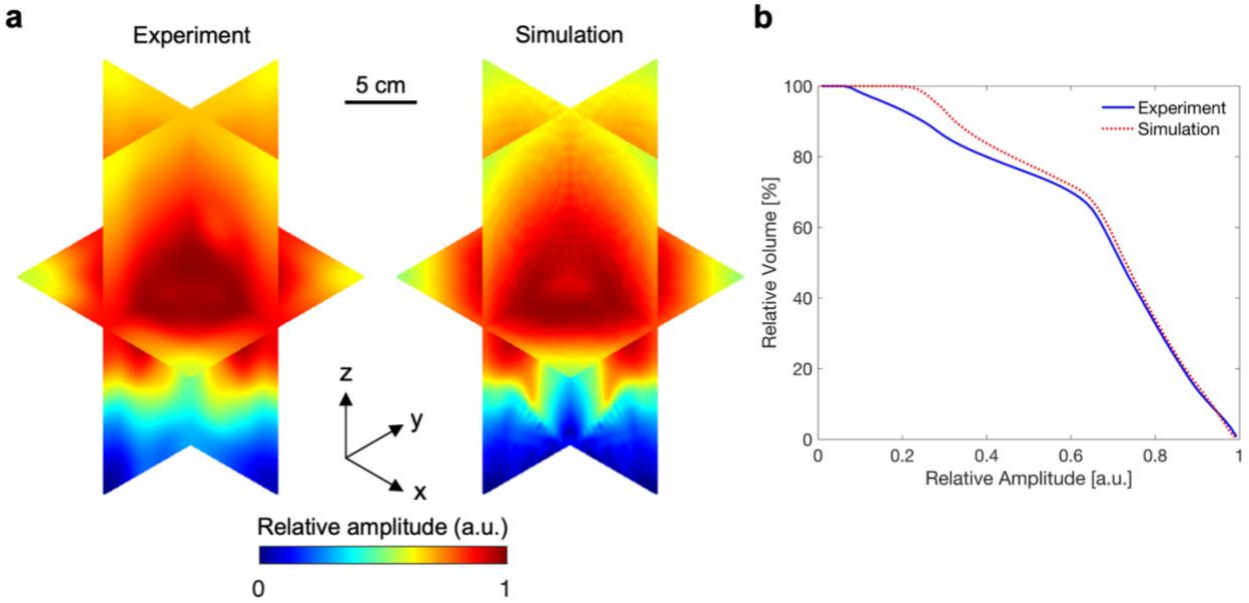


Figure 3.4 Detection sensitivity characterization of the 2D MAT. (a) Orthogonal cross-sectional views of simulated and experimentally measured detection sensitivity maps. The color bar represents relative amplitude in arbitrary units (a.u.), ranging from 0 (blue) to 1 (red). The scale bar indicates 5 cm. The orientation of the sensitivity maps follows the indicated coordinate system, where the x-, y-, and z-axes correspond to azimuth, elevation, and depth, respectively. (b) Comparison of DVH curves derived from the simulated and experimental volumetric detection sensitivity maps.

3.3.2 Radiation Beam Quantification

Representative results for a 2 cm × 2 cm radiation beam are shown in Figure 3.5. The radiochromic film measurement and its normalized pseudo-color representation serve as reference dose distributions (Figure 3.5a–b). The corresponding iRAI reconstruction before sensitivity compensation is shown in Figure 3.5c, where lateral amplitude asymmetry and depth-dependent intensity variation are observed. After applying sensitivity compensation, the corrected image (Figure 3.5d) exhibits improved spatial uniformity across the beam region.

Depth-dependent amplitude profiles extracted along the central axis are presented in Figure 3.5e. Prior to compensation, reconstructed amplitudes increase with depth, reflecting higher detection sensitivity near deeper focal regions. After compensation (Figure 3.5g), this depth-dependent variation is substantially reduced, and normalized amplitudes approach a more uniform distribution.

Lateral amplitude profiles at a fixed depth are shown in Figure 3.5f. Before compensation, the profiles exhibit center-weighted intensity and mild asymmetry between the left and right sides. After compensation (Figure 3.5h), spatial variation is reduced, and the profiles show improved agreement with the simulated results.

For beams with varying field sizes delivered at a depth of 11 cm, experimental depth-dependent profiles are presented in Figure 3.5i, and the corresponding compensated profiles are shown in Figure 3.5j. Simulation results before and after compensation are shown in Figure 3.5k–l. Prior to compensation, the depth profiles exhibit systematic upward trends consistent with the spatial sensitivity distribution shown in Figure 3.4. After compensation, the profiles become more uniform while preserving sharp beam boundaries and distinct field sizes, indicating effective reduction of sensitivity-induced distortion without degradation of spatial resolution.

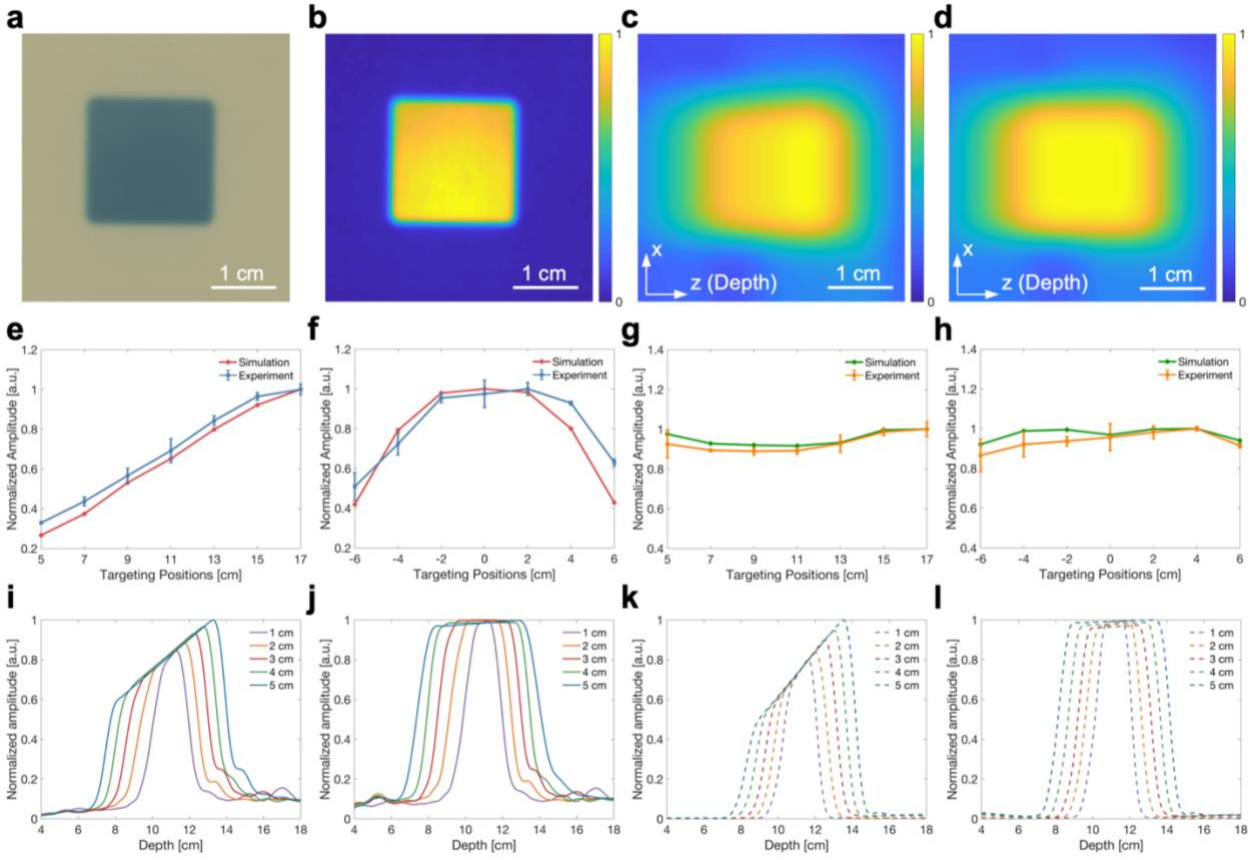


Figure 3.5 Quantification of radiation beams before and after sensitivity compensation. (a) A 2 cm × 2 cm radiation beam deposited on radiochromic film. (b) Normalized pseudocolor representation of the film measurement shown in (a). (c) 2D cross-sectional iRAI image of the 2 cm × 2 cm beam. (d) Sensitivity-compensated image corresponding to (c), obtained using correction factors derived from experimentally measured detection sensitivity. (e) Normalized amplitude profiles along the z-direction, comparing experimental and simulated results before compensation. (f) Normalized amplitude values measured at seven positions along the x-direction at a depth of z = 11 cm from the MAT surface. (g, h) Amplitude profiles extracted from compensated iRAI images corresponding to (e) and (f), respectively.

3.3.3 Quantitative Evaluation of a C-Shaped Treatment Plan

The effect of sensitivity compensation under a spatially complex dose distribution is illustrated in Figure 3.6. An axial cross-section of the C-shaped treatment plan is shown in Figure 3.6a, with the corresponding reconstructed iRAI images before and after compensation displayed in Figure 3.6b–c. All images were normalized for comparison. Before compensation, the reconstructed iRAI image exhibits reduced signal intensity in deeper and off-axis regions, resulting in boundary distortion and asymmetric amplitude distribution. After compensation, signal uniformity improves, and the reconstructed C-shaped structure shows closer agreement with the treatment plan.

Sagittal cross-sections are shown in Figure 3.6d–f. The pre-compensation image exhibits noticeable left–right imbalance and reduced uniformity. After compensation, the reconstructed image demonstrates improved geometric conformity to the planned dose distribution. The comparison of 80% isodose contours is provided in Figure 3.6g–h. In axial views, compensation reduces inward displacement and improves alignment with the planned C-shaped geometry. In sagittal views, the compensated contours better follow the superior and inferior boundaries, although small discrepancies remain near the outer edges.

Volumetric DVH analysis is shown in Figure 3.6i. The DVH obtained before compensation deviates from the treatment plan, indicating underestimation of higher-dose regions. After compensation, the DVH curve shifts toward the reference distribution, indicating improved recovery of higher-dose regions. The root-mean-square error (RMSE) between DVHs decreases from 6.92 to 4.85 after compensation. 3D global gamma analysis (5% dose difference and 5 mm distance-to-agreement) further demonstrates improvement, with the passing rate increasing from 56.86% before compensation to 78.24% after compensation.

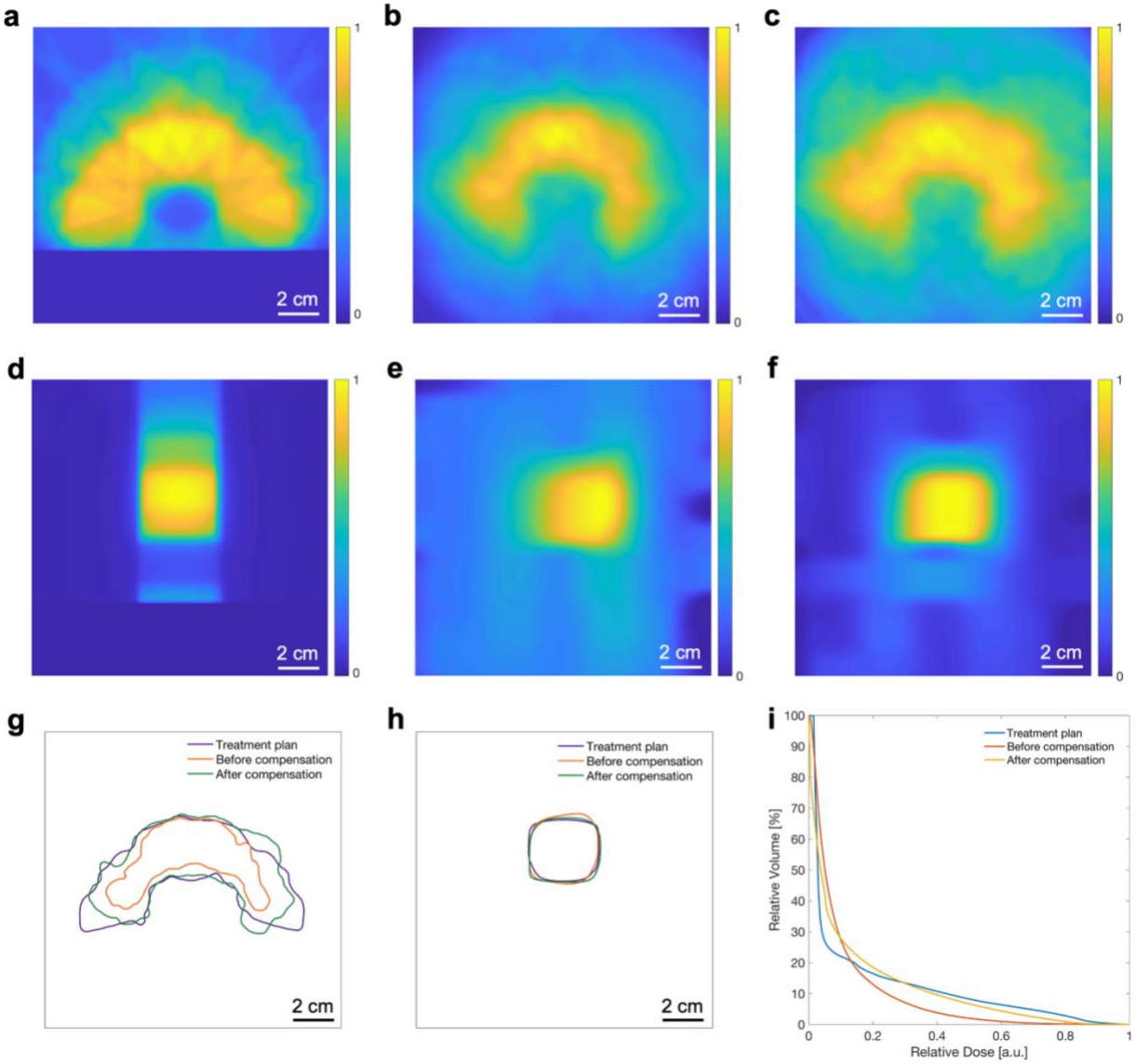


Figure 3.6 Reconstructed iRAI images and quantitative evaluation of the C-shaped treatment plan. (a) Axial cross-section of the treatment plan at the mid-plane of the C-shaped dose distribution along the z-axis. (b) Corresponding axial cross-section reconstructed from the iRAI image before sensitivity compensation. (c) Axial cross-section after sensitivity compensation. (d) Sagittal cross-section of the dose distribution from the treatment plan. (e) Corresponding sagittal cross-section reconstructed from the iRAI image before compensation. (f) Sagittal cross-section after compensation. All images were normalized for comparison. (g) Comparison of 80% isodose contours in axial cross-sections from the treatment plan, pre-compensation iRAI reconstruction, and post-compensation reconstruction corresponding to (a–c). (h) Comparison of 80% isodose contours in sagittal cross-sections from the treatment plan, pre-compensation reconstruction, and post-compensation reconstruction corresponding to (d–f). (i) Comparison of DVHs derived from volumetric dose distributions of the treatment plan, pre-compensation iRAI reconstruction, and post-compensation reconstruction.

3.4 Discussion and Conclusions

This chapter examined spatial bias in volumetric iRAI reconstruction arising from non-uniform transducer detection sensitivity. By experimentally characterizing the 3D receiving sensitivity of the MAT and incorporating voxel-wise correction into the reconstruction process,

systematic amplitude distortion was reduced. After compensation, the reconstructed dose distributions showed improved agreement with the reference dose distributions for both simple beam geometries and spatially complex treatment patterns.

Previous studies from our group have demonstrated the feasibility of *in vivo* iRAI for monitoring radiation delivery in patient studies. These experiments were primarily conducted at anatomically favorable locations, where acoustic windows were sufficient, attenuation was limited, and the transducer–target geometry was relatively simple. A broader evaluation under diverse anatomical conditions and treatment configurations has not yet been fully explored.

To isolate the effect of transducer detection sensitivity, experiments were conducted in a homogeneous medium. In realistic anatomical environments, additional factors such as heterogeneous acoustic propagation and increased structural complexity may further influence reconstruction accuracy. These factors introduce additional challenges beyond transducer sensitivity alone and motivate further investigation.

Building on the sensitivity-compensated reconstruction developed in this chapter, the following chapter evaluates quantitative iRAI performance in an abdominal phantom with anatomically relevant structures and treatment delivery conditions.

Chapter 4 Volumetric Dose Mapping in an Anthropomorphic Abdominal Phantom

4.1 Introduction

Accurate volumetric verification of delivered dose remains an important objective in radiotherapy, particularly in anatomically complex regions such as the abdomen. While the previous chapter introduced a sensitivity-compensated reconstruction framework under homogeneous conditions, more anatomically structured and clinically relevant settings involve additional sources of variability, including anatomical structure, beam modulation, and complex treatment geometries.

The abdominal region presents several challenges for acoustic-based dose mapping. Variations in tissue composition, acoustic impedance mismatches, and depth-dependent attenuation can affect the propagation of radiation-induced acoustic signals and influence reconstruction accuracy. In addition, modern radiotherapy techniques such as 3DCRT, IMRT, and VMAT produce spatially complex dose distributions, placing increased demands on volumetric dose mapping.

To evaluate system performance in a more anatomically structured setting beyond homogeneous conditions, this chapter investigates volumetric iRAI dose mapping using an anthropomorphic abdominal phantom. The study examines reconstruction performance in the presence of anatomical structures and commonly used clinical beam delivery techniques, providing an initial extension of validation beyond homogeneous conditions. Quantitative comparisons with treatment planning dose distributions are performed to assess the performance of the sensitivity-compensated reconstruction framework in this structured phantom setting.

4.2 Materials and Methods

4.2.1 Abdominal Phantom and Experimental Configuration

An anthropomorphic abdominal phantom (model 057A, Sun Nuclear Corp., USA) was used to evaluate volumetric iRAI dose mapping under anatomically structured phantom conditions. The phantom measured approximately 26 × 19 × 12.5 cm^3 and weighed about 5 kg. It consisted of an acrylonitrile butadiene styrene (ABS) outer housing, a Z-Skin™ elastomer layer mimicking subcutaneous fat, and internal structures composed of Zerdine® gel and epoxy resin representing soft tissue and bone, respectively. The phantom contained anatomically relevant structures, including the liver, kidneys, spine, ribs, and surrounding abdominal soft tissue.

The overall experimental configuration is shown in Figure 4.1(a). The phantom was positioned on the treatment couch in the supine orientation, with the anterior surface facing upward. A water-filled balloon was placed between the 2D MAT and the phantom surface to provide stable acoustic coupling. Axial, sagittal, and coronal orientations are indicated in the figure to define the anatomical reference planes.

For geometric alignment, cone-beam CT (CBCT) imaging was performed prior to irradiation. A representative axial CBCT slice used for positioning is shown in Figure 4.1(b), where both the abdominal phantom and the transducer location are indicated. CBCT guidance was used to support consistent spatial alignment among the phantom, the treatment isocenter, and the transducer.

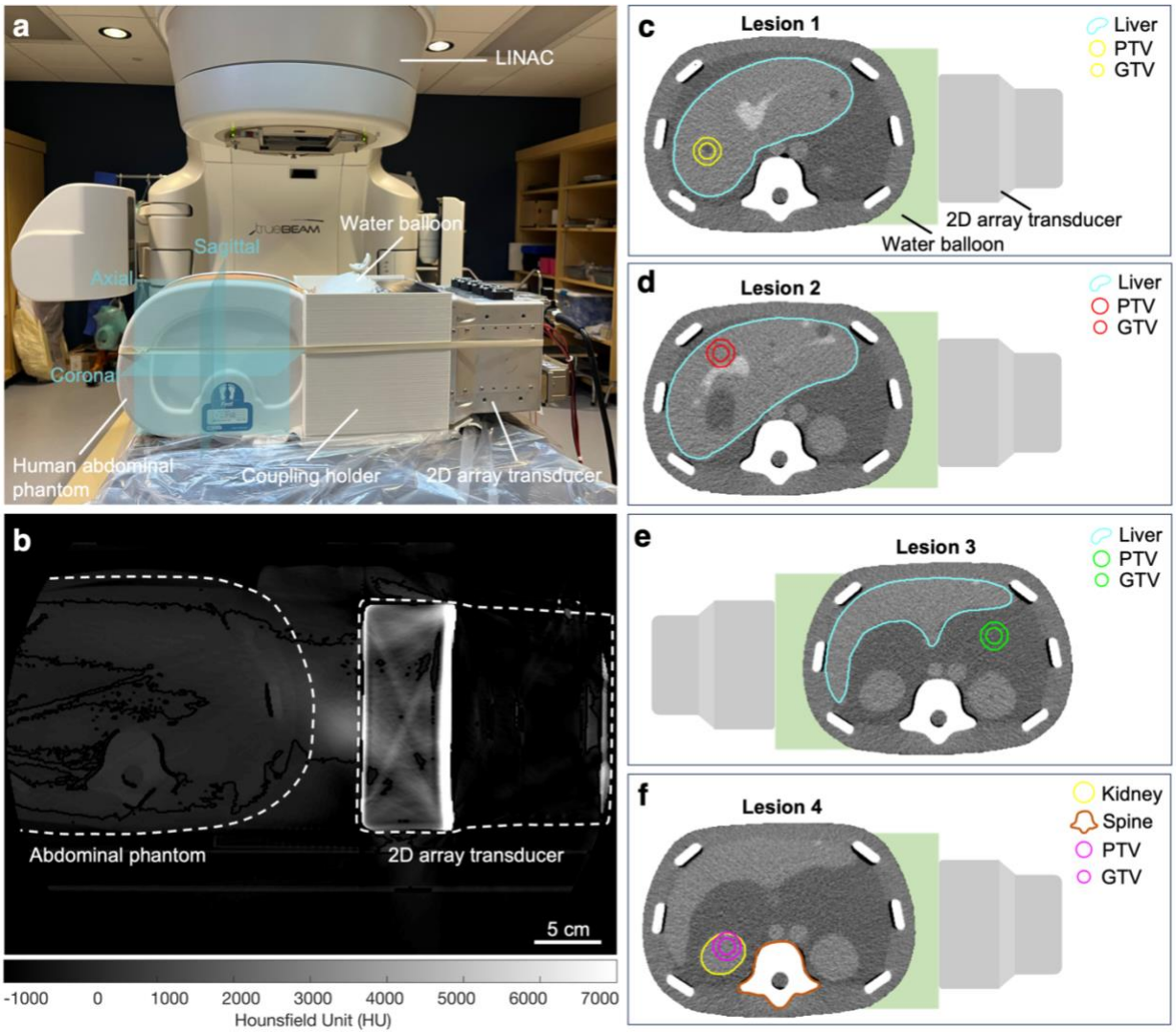


Figure 4.1 Experimental design of the anthropomorphic abdominal phantom study. (a) Photograph of the experimental setup. The phantom was positioned on the treatment couch with the inferior side facing the camera and the anterior surface facing upward. A water-filled balloon was placed between the transducer and the phantom to provide acoustic coupling. Axial, sagittal, and coronal planes are indicated to define the anatomical reference orientations. (b) Schematic illustration of Lesion 1 located in the right liver. The GTV, PTV and adjacent organs are outlined using color-coded solid lines. This configuration was used for 3DCRT, IMRT, and VMAT treatment plans. (c) Schematic illustration of Lesion 2 located anterior to the liver, used for a VMAT treatment plan. (d) Schematic illustration of Lesion 3 located in abdominal soft tissue lateral to the liver, used for a VMAT treatment plan. (e) Schematic illustration of Lesion 4 located in the right kidney. The spine partially blocked the acoustic propagation path between the transducer and the lesion. This configuration was used for a VMAT treatment plan.

4.2.2 Target Configurations and Treatment Planning

Four target configurations were designed to sample different anatomical locations and acoustic propagation conditions within the abdominal region. Treatment plans were generated using a clinical TPS based on CT images of the phantom.

For all targets, the gross tumor volume (GTV) was defined as a spherical region with a diameter of 1.5 cm. The planning target volume (PTV) was generated by expanding the GTV by 0.5 cm radially and 0.8 cm in the superior–inferior direction, resulting in approximate PTV dimensions of 2.5 cm in the left–right and anterior–posterior directions and 3.1 cm in the superior–inferior direction.

Lesion 1, located in the right liver, is illustrated in Figure 4.1(b). The GTV, PTV, and adjacent OARs, including the liver and kidney, are indicated. This configuration was evaluated using three delivery techniques: 3DCRT, IMRT and VMAT. Lesion 2 was positioned anterior to the liver, as shown in Figure 4.1(c). Lesion 3 was located in abdominal soft tissue lateral to the liver (Figure 4.1(d)). Lesion 4 was placed within the right kidney (Figure 4.1(e)), where the spine partially obstructed the acoustic propagation path between the transducer and the lesion. Lesions 2–4 were evaluated using VMAT delivery.

All treatment plans prescribed a dose of 50 Gy in five fractions, following a clinically relevant SBRT-style dose fractionation scheme. The plans were optimized to achieve adequate PTV coverage while following planning constraints for surrounding OARs in this phantom study.

4.2.3 Volumetric iRAI Acquisition and Reconstruction

Volumetric iRAI data were acquired during radiation beam delivery using the imaging system and acquisition framework described in Chapter 3. The system was synchronized with LINAC pulses to record radiation-induced acoustic signals generated by each pulse during irradiation.

The acquired radiofrequency signals were bandpass filtered (0.1–1 MHz) and reconstructed into volumetric images using a 3D DAS beamforming algorithm implemented in MATLAB. Voxel-wise transducer sensitivity compensation, as described in Chapter 3, was applied after reconstruction to reduce the influence of spatial variations in detection sensitivity.

To enable comparison with treatment planning data, reconstructed iRAI volumes were spatially aligned with the planning CT using CBCT images to determine the relative geometry between the phantom and the transducer. The reconstructed iRAI volumes represent relative radiation-induced acoustic signal distributions and were not independently calibrated as absolute dose maps. Axial and sagittal cross-sections passing through the center of the PTV were extracted for visualization and subsequent quantitative analysis.

4.2.4 Quantitative Evaluation

Quantitative evaluation was performed by comparing reconstructed iRAI relative dose maps with the corresponding treatment plan dose maps. Both qualitative and quantitative metrics were used to assess agreement between the two datasets.

For visualization, sagittal and axial slices passing through the geometric center of the PTV were selected. Isodose lines at 50%, 70%, and 90% of the maximum dose were extracted from both the treatment plan and the iRAI images and overlaid to assess spatial agreement of the dose distributions. These levels correspond to low-, intermediate-, and high-dose regions commonly used in radiotherapy plan evaluation.

For volumetric evaluation, DVH analysis was performed for the PTV and corresponding OARs. DVHs were computed from both the treatment plan and reconstructed iRAI volumes. Prior to comparison, reconstructed iRAI maps were linearly normalized by matching their maximum intensity to the maximum dose in the corresponding treatment plan. This normalization allowed comparison of the relative volumetric dose distribution but did not represent an independent absolute dose calibration. The iRAI volumes were resampled to match the treatment plan grid, and structure masks derived from the planning CT were aligned to the reconstructed iRAI volumes using the CBCT-based spatial registration described above.

To quantify differences between DVH curves, the mean absolute error (MAE) between the treatment plan DVH and iRAI-derived DVH was calculated across uniformly sampled dose bins. In addition, commonly used DVH metrics were extracted for comparison. For the PTV, these included D95, defined as the dose received by 95% of the PTV volume, and D2, defined as the dose received by the hottest 2% of the PTV volume. For OARs, the mean dose (Dmean) and volume-based metrics were evaluated. Specifically, V30 was calculated for the liver and V20 for the kidney, representing the percentage of organ volume receiving at least 30 Gy and 20 Gy, respectively. For iRAI, these DVH metrics were interpreted as normalized, plan-scaled estimates rather than independently measured absolute dose values.

4.3 Results

4.3.1 iRAI–CT Co-registered Images

The reconstructed volumetric iRAI dose maps were co-registered with the planning CT using CBCT as the spatial reference. This alignment enabled anatomical comparison between

iRAI-derived relative dose maps and TPS dose distributions. Sagittal and axial slices through the center of the PTV were selected to visualize the fused iRAI–CT images.

Figures 4.2–4.3 show Lesion 1 in the right liver treated with 3DCRT, IMRT, and VMAT, while Figures 4.4–4.5 show Lesions 2–4 treated with VMAT. TPS images display absolute dose distributions, whereas iRAI reconstructions are shown as normalized relative dose maps in the range of 0–1.

For Lesion 1, evaluated with 3DCRT, IMRT, and VMAT delivery techniques, the high-dose region was localized near the planned target region in both sagittal and axial views. The reconstructed iRAI maps showed overall spatial correspondence with the target region and surrounding anatomical structures. Visual differences among 3DCRT, IMRT, and VMAT reflected the plan-specific dose distributions in this configuration, rather than a controlled comparison of delivery technique performance.

For Lesions 2 and 3, located anterior and lateral to the liver, respectively, the fused images showed visually similar spatial patterns between iRAI reconstructions and TPS dose distributions. The PTV location remained identifiable, and the relative positioning of the high-dose region within the abdominal anatomy was generally preserved.

For Lesion 4, positioned in the right kidney, the iRAI images showed reduced signal recovery and mild boundary distortion compared with the TPS dose distribution. These deviations were consistent with partial acoustic shadowing caused by the spine along the acoustic propagation path.

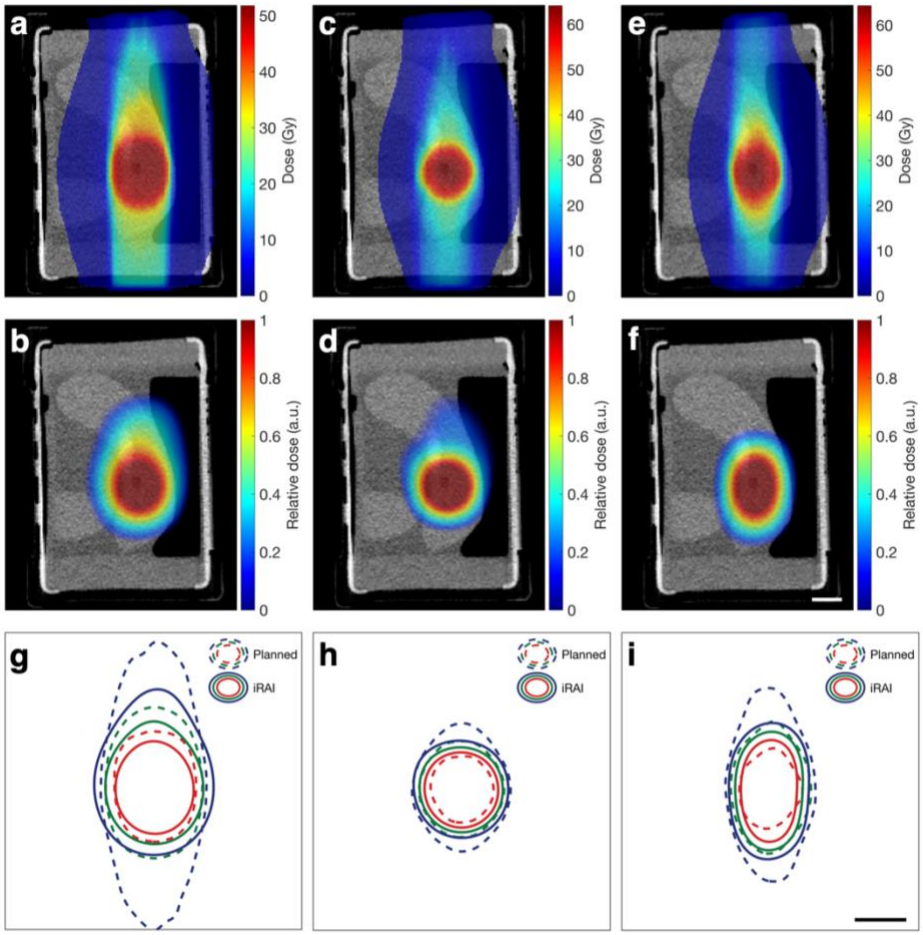


Figure 4.2 Sagittal dose maps and isodose line comparisons between the treatment plan and iRAI for Lesion 1. Sagittal sections are taken through the center of the PTV. (a) Treatment plan dose distribution for 3DCRT. (b) Reconstructed iRAI dose distribution for 3DCRT. (c) Treatment plan dose distribution for IMRT. (d) Reconstructed iRAI dose distribution for IMRT. (e) Treatment plan dose distribution for VMAT. (f) Reconstructed iRAI dose distribution for VMAT. (g–i) Isodose line comparisons (50% blue, 70% green, 90% red) for 3DCRT, IMRT, and VMAT, respectively. Treatment plan contours are shown as dashed lines and iRAI contours as solid lines. Scale bars represent 2 cm.

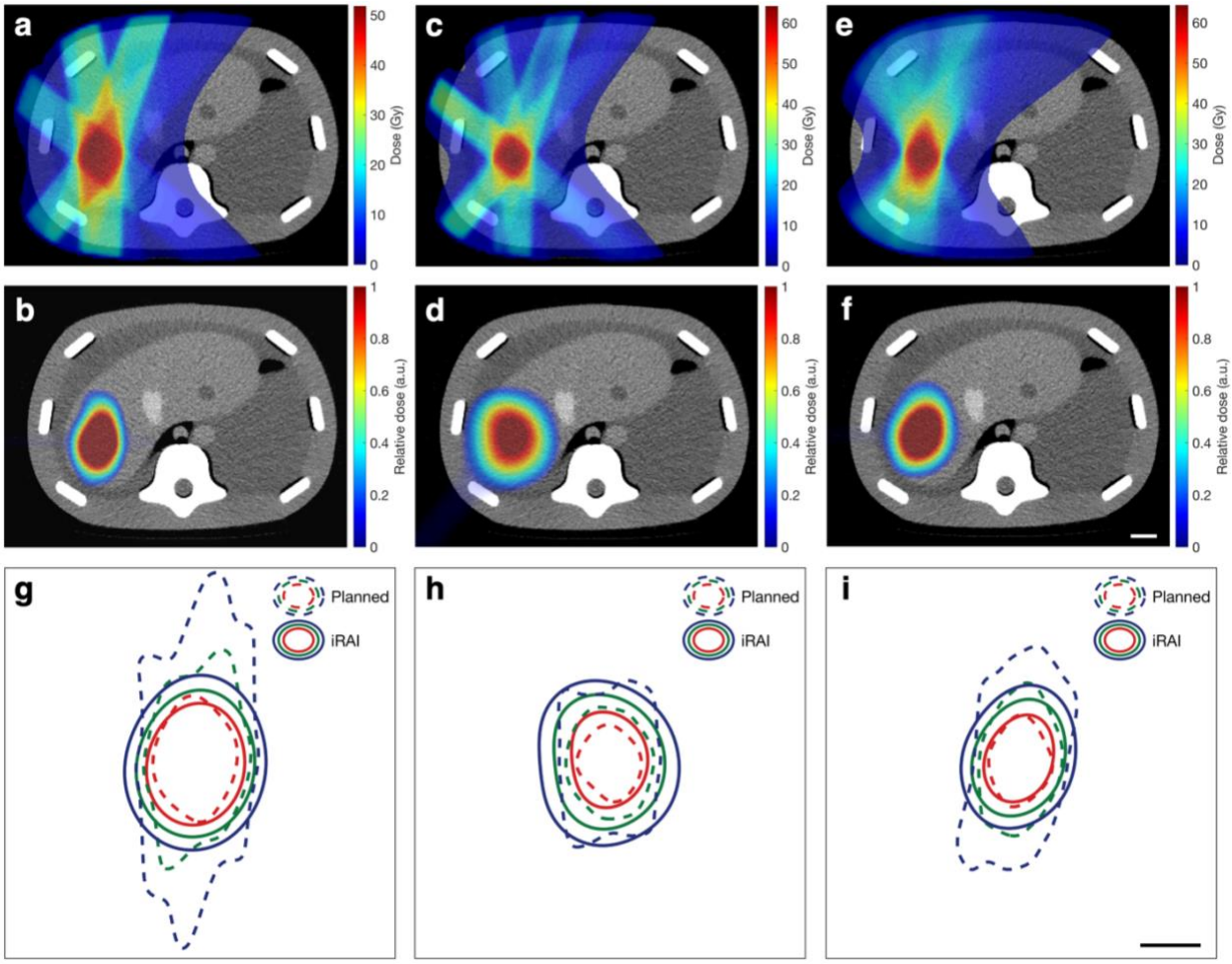


Figure 4.3 Axial dose maps and isodose line comparisons between the treatment plan and iRAI for Lesion 1. Axial sections are taken through the center of the PTV. (a) Treatment plan dose distribution for 3DCRT. (b) Reconstructed iRAI dose distribution for 3DCRT. (c) Treatment plan dose distribution for IMRT. (d) Reconstructed iRAI dose distribution for IMRT. (e) Treatment plan dose distribution for VMAT. (f) Reconstructed iRAI dose distribution for VMAT. (g–i) Isodose line comparisons (50% blue, 70% green, and 90% red) for 3DCRT, IMRT, and VMAT, respectively. Treatment plan contours are shown as dashed lines, and iRAI contours are shown as solid lines. Scale bars represent 2 cm.

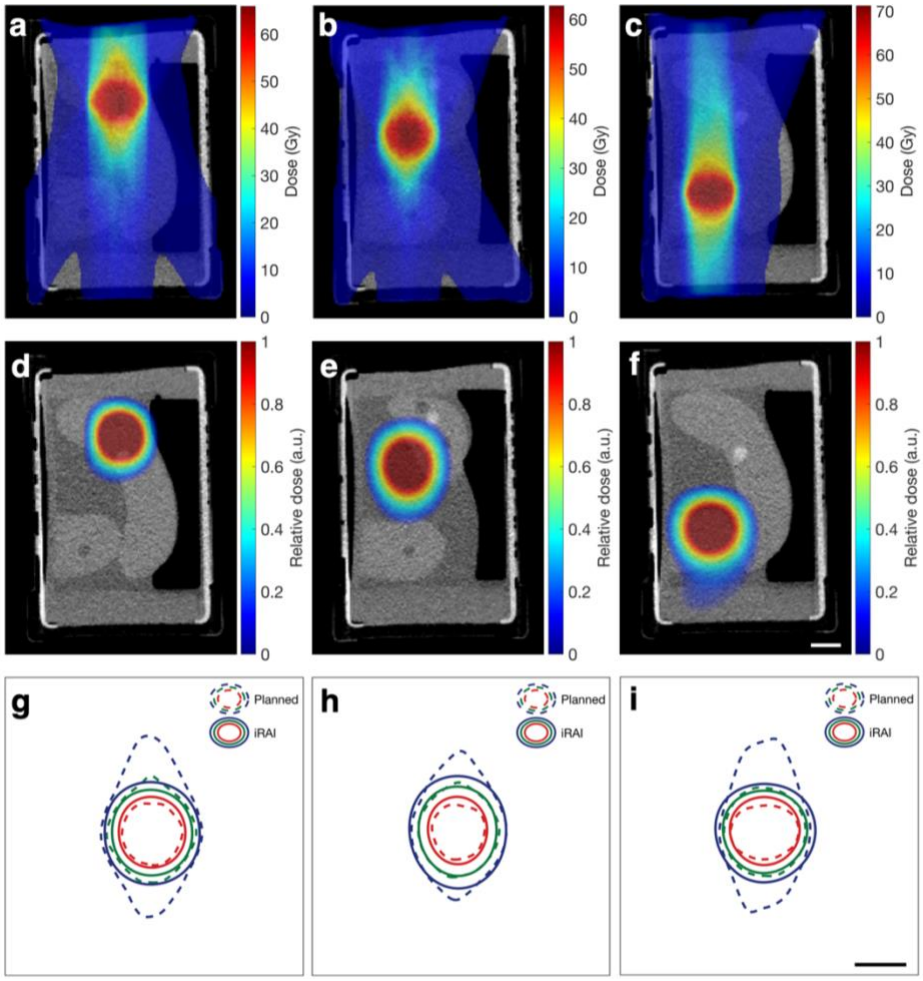


Figure 4.4 Sagittal dose maps and isodose line comparisons between the treatment plan and iRAI for Lesions 2–4. Sagittal sections are taken through the center of the PTV. (a) Treatment plan dose distribution for Lesion 2 (anterior to the liver). (b) Reconstructed iRAI dose distribution for Lesion 2. (c) Treatment plan dose distribution for Lesion 3 (abdominal soft tissue lateral to the liver). (d) Reconstructed iRAI dose distribution for Lesion 3. (e) Treatment plan dose distribution for Lesion 4 (right kidney, adjacent to the spine). (f) Reconstructed iRAI dose distribution for Lesion 4. (g–i) Isodose line comparisons (50% blue, 70% green, and 90% red) for Lesions 2–4, respectively. Treatment plan contours are shown as dashed lines, and iRAI contours are shown as solid lines. Scale bars represent 2 cm.

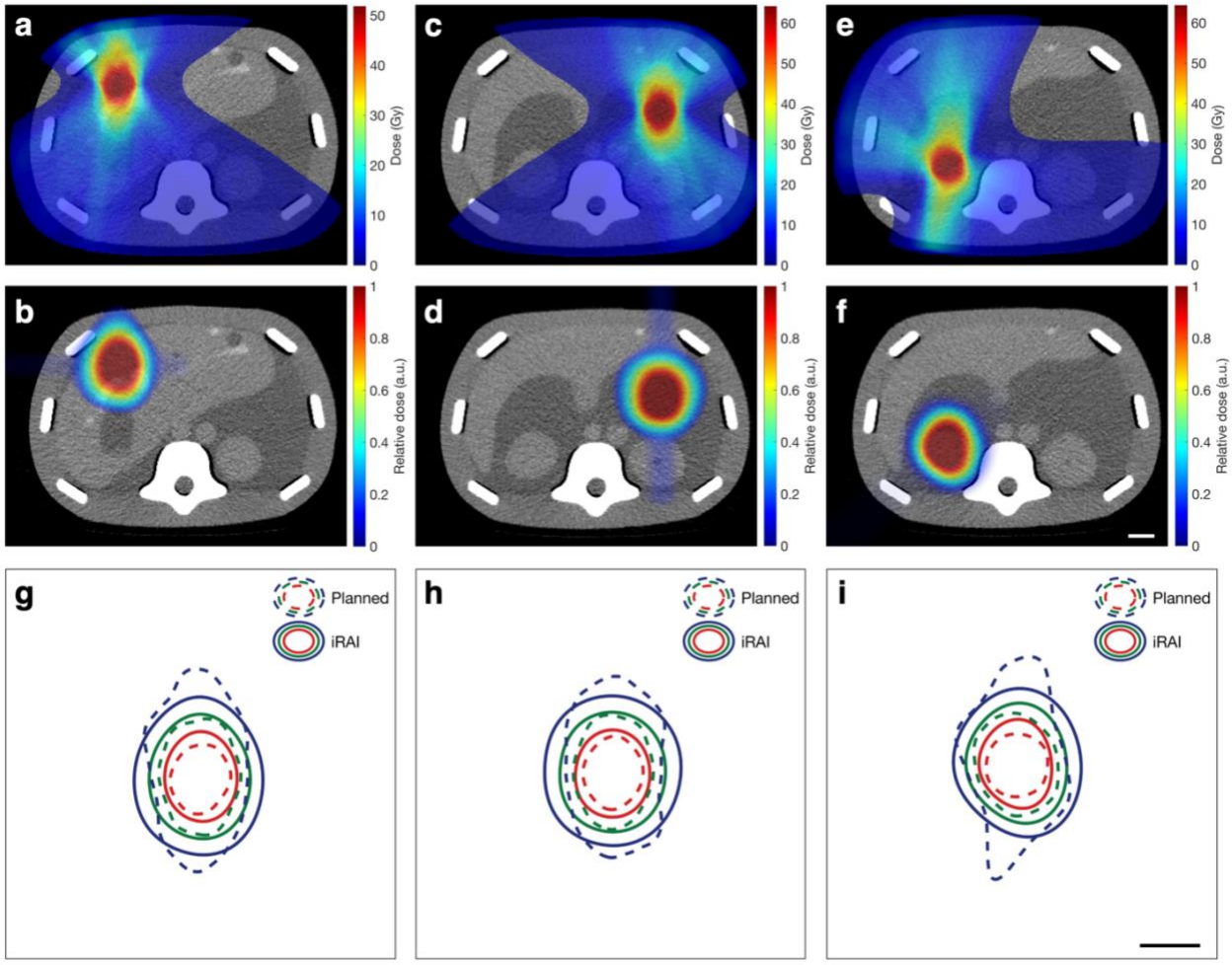


Figure 4.5 Axial dose maps and isodose line comparisons between the treatment plan and iRAI for Lesions 2–4. Axial sections are taken through the center of the PTV. (a) Treatment plan dose distribution for Lesion 2. (b) Reconstructed iRAI dose distribution for Lesion 2. (c) Treatment plan dose distribution for Lesion 3. (d) Reconstructed iRAI dose distribution for Lesion 3. (e) Treatment plan dose distribution for Lesion 4. (f) Reconstructed iRAI dose distribution for Lesion 4. (g–i) Isodose line comparisons (50% blue, 70% green, and 90% red) for Lesions 2–4, respectively. Treatment plan contours are shown as dashed lines, and iRAI contours are shown as solid lines. Scale bars represent 2 cm.

4.3.2 Isodose Line Comparisons Between the Treatment Plan and iRAI

Sagittal and axial isodose maps for Lesion 1 in the right liver treated with 3DCRT, IMRT, and VMAT are shown in Figures 4.2g–i and 4.3g–i. The 90%, 70%, and 50% isodose levels are indicated in red, green, and blue, respectively. Dashed contours correspond to the treatment plan, while solid contours represent the iRAI reconstructions.

Across all three delivery techniques, the iRAI-derived isodose contours showed spatial patterns generally similar to those of the treatment plan. In this specific lesion configuration, the IMRT case showed visually closer contour alignment at the 90% and 70% levels. However, this observation reflects this individual plan configuration and should not be interpreted as a controlled

comparison of delivery technique performance. In both the 3DCRT and VMAT cases, the 50% contours appeared contracted relative to the treatment plan, particularly along the superior–inferior direction. This discrepancy was most pronounced in the peripheral low-dose regions.

Figures 4.4g–i and 4.5g–i present the corresponding sagittal and axial isodose maps for Lesions 2–4, all delivered with VMAT. The same color scheme is used for the three dose levels. For Lesions 2 and 3, located anterior and lateral to the liver, the 90% and 70% contours showed visually similar patterns to the treatment plan in both views. At the 50% level, the iRAI contours exhibited mild contraction and slight irregularities near the dose boundaries.

Larger discrepancies were observed for Lesion 4 in the right kidney. While the 90% contour remained identifiable, the 70% and 50% contours exhibited asymmetric contraction and local distortion. These differences were consistent with acoustic shadowing caused by the spine along the propagation path.

Overall, higher-dose contours showed closer spatial correspondence with the treatment plan than the lower-dose contours, where signal levels were lower and boundary deviations were more apparent.

4.3.3 DVH Comparison Between iRAI and Treatment Plan

Figure 4.6 shows DVHs derived from the treatment plan (solid lines) and iRAI (dotted lines) for the PTV and corresponding OARs in each configuration. Dose values are normalized to the maximum dose of the respective treatment plan, and volume is normalized to the structure volume.

Overall, the DVH curves from iRAI followed the general trends of the treatment plans, although the degree of agreement varied across cases. For the PTV, smaller deviations were observed in Lesion 1 (IMRT), Lesion 1 (VMAT), Lesion 2 (VMAT), and Lesion 3 (VMAT), whereas larger deviations were observed in Lesion 1 (3DCRT) and Lesion 4 (VMAT). The larger discrepancy in Lesion 4 was consistent with reduced signal recovery caused by partial acoustic shadowing from the spine. These differences should be interpreted as case-specific effects related to dose distribution, target location, and acoustic access, rather than as a ranking of delivery techniques.

Table 4.1 summarizes quantitative DVH metrics for the PTV and OARs from both the treatment plan and iRAI across all lesions and delivery techniques. For the PTV, the iRAI-derived DVHs captured the general trend of the high-dose plateau observed in the treatment plans. The

D95 values from iRAI were typically within approximately 1–3 Gy of the treatment plan, while D2 values followed a similar trend and remained within about 2 Gy in most cases. The largest D2 deviation occurred for Lesion 4 (VMAT), consistent with the reduced signal recovery observed in the reconstructed images.

For OARs, deviations were generally larger and more variable than those observed for the PTV. Mean dose differences ranged from less than 1 Gy to more than 4 Gy depending on the configuration. V30 and V20 differences also varied across cases, with larger deviations observed in Lesion 1 (3DCRT) and Lesion 4 (VMAT). Across all configurations, PTV DVHs showed smaller deviations from the treatment plan than the corresponding OAR DVHs. These observations are based on a limited number of phantom configurations and should be interpreted within this experimental scope.

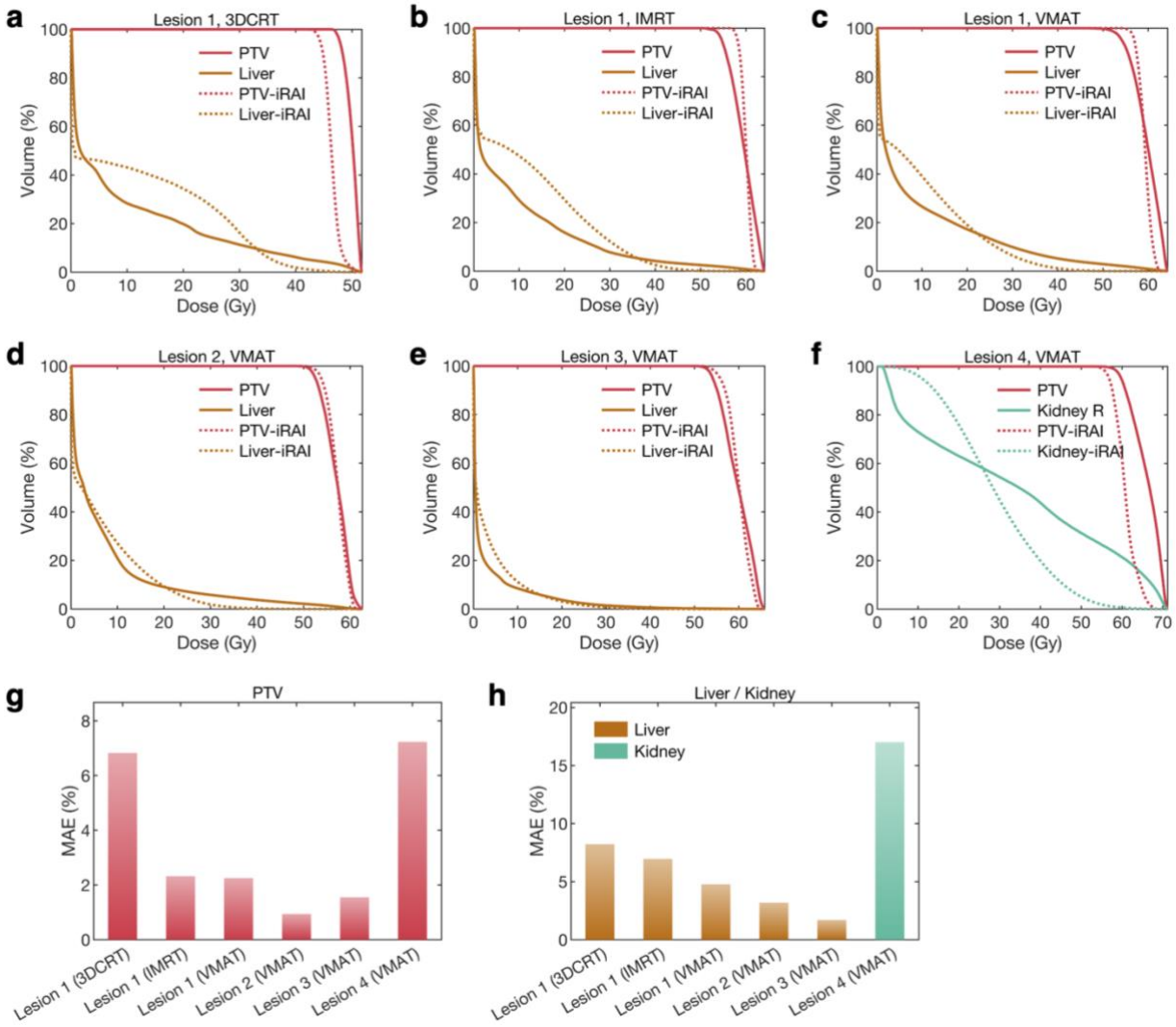


Figure 4.6 DVH comparisons between the treatment plan (solid lines) and iRAI (dotted lines) for the PTV and corresponding OAR (liver or kidney) in each case. a, Lesion 1 in the right liver treated with 3DCRT. b, Lesion 1 treated with IMRT. c, Lesion 1 treated with VMAT. d, Lesion 2 located anterior to the liver (VMAT). e, Lesion 3 located in abdominal soft tissue lateral to the liver (VMAT). f, Lesion 4 in the right kidney (VMAT). Dose is normalized to the maximum value of the corresponding treatment plan, and volume is normalized to the structure volume. g, MAE between treatment plan and iRAI DVHs for the PTV in each case. h, MAE between treatment plan and iRAI DVHs for the OAR in each case.

Table 4.1 DVH metrics for PTV and OARs from TPS and iRAI.

Structure (ROI)	DVH metric	Dose set	Lesion			Lesion	Lesion	Lesion
			3DCRT	IMRT	VMAT		VMAT	
PTV	D95 (Gy)	TPS	47.82	54.65	54.20	52.57	54.08	59.79
		iRAI	44.34	58.13	56.94	53.81	55.78	56.86
		|iRAI−TPS|	3.48	3.47	2.74	1.25	1.70	2.93
	D2 (Gy)	TPS	51.57	63.75	64.00	61.66	65.16	70.80
		iRAI	49.98	61.97	62.02	60.70	64.14	66.76
		|iRAI−TPS|	1.60	1.78	1.98	0.95	1.02	4.04

OAR	Dmean (Gy)	TPS	9.43	8.71	8.98	7.13	2.66	33.86
		iRAI	11.93	11.97	9.29	6.43	3.38	29.26
		|iRAI−TPS|	2.50	3.26	0.32	0.70	0.72	4.60
	V30/V20 (%)	TPS	11.30	7.77	9.89	5.81	1.26	63.09
		iRAI	16.25	12.23	6.39	1.85	0.76	75.95
		|iRAI−TPS|	4.96	4.46	3.50	3.96	0.49	12.87

Metrics: D95, dose to 95% of the PTV volume; D2, dose to 2% of the PTV volume; Mean dose, average dose to the OAR; V30/V20, OAR volume receiving ≥30 Gy (liver, Lesions 1–3) or ≥20 Gy (kidney, Lesion 4); |iRAI − TPS|, absolute difference between iRAI and TPS values.

4.4 Discussion and Conclusions

This chapter evaluated volumetric iRAI dose mapping using an anthropomorphic abdominal phantom with anatomically structured targets and clinically used delivery techniques. The results show that iRAI can localize high-dose regions and show overall spatial correspondence between radiation-induced acoustic signal distributions and planned dose distributions relative to surrounding anatomical structures. Compared with previous studies performed in homogeneous or anatomically simplified environments, this work extends volumetric iRAI evaluation to a more structurally complex setting that better reflects clinically relevant imaging conditions.

The level of agreement varied across configurations. Smaller deviations were observed for target locations with relatively unobstructed acoustic paths, whereas larger deviations appeared in cases with partial acoustic shadowing, such as the kidney lesion adjacent to the spine. In addition, higher-dose regions generally exhibited closer spatial correspondence than lower-dose regions, which is consistent with the higher signal amplitude associated with dose deposition near the prescription level. These findings suggest that iRAI performance depends not only on dose deposition patterns, but also on anatomical structure and acoustic accessibility.

Building on the sensitivity-compensated reconstruction framework developed in the previous chapter, this study demonstrates the feasibility of volumetric relative dose mapping under anatomically structured phantom conditions. The results suggest that sensitivity compensation remains beneficial in more realistic geometries, where acoustic propagation conditions and target accessibility become increasingly complex. At the same time, the current implementation is based on delay-and-sum beamforming and does not explicitly account for heterogeneous acoustic propagation within the imaging medium. Incorporating heterogeneous acoustic modeling into the reconstruction process may further improve reconstruction fidelity and quantitative accuracy, particularly in anatomically complex regions.

Although encouraging agreement was observed between iRAI and planned dose distributions, the current study remains an initial phantom-based evaluation. The experiments were performed using a single anthropomorphic abdominal phantom and a limited number of target configurations. Important clinical factors, including respiratory motion, tissue deformation, setup variability, and patient-specific acoustic heterogeneity, were not incorporated in this study. In addition, the reconstructed iRAI distributions remain normalized representations of deposited dose and do not yet provide independently calibrated absolute dose measurements.

Overall, this study demonstrates the feasibility of volumetric iRAI for visualizing radiation-induced acoustic signal distributions under anatomically structured and clinically relevant phantom conditions. These results provide an initial step toward evaluating iRAI-based dose mapping beyond homogeneous environments and support the continued development of volumetric iRAI for future in vivo radiotherapy dose verification applications.

Chapter 5 Translational Photoacoustic–Ultrasound Imaging Catheter for Crohn's Disease

5.1 Introduction

This chapter explores a translational application of acoustic-based imaging technologies for gastrointestinal disease characterization.

Inflammatory bowel diseases, particularly Crohn's disease (CD), frequently involve pathological changes that extend beyond the mucosal surface. In clinical practice, conventional endoscopy primarily provides visual assessment of the mucosa and lumen but offers limited information about deeper layers of the bowel wall. However, pathological processes such as inflammation, fibrosis, and structural remodeling often occur within the submucosal and muscular layers, which are not accessible through surface visualization alone.

Cross-sectional imaging modalities, including CT and MRI, can provide structural information such as bowel wall thickening and surrounding tissue characteristics. However, these modalities are not available during endoscopic procedures and offer limited sensitivity to the molecular composition of intestinal tissue. As a result, key pathological features that influence treatment decisions, particularly the distinction between inflammation and fibrosis, remain difficult to assess during routine gastrointestinal examinations.

Photoacoustic–ultrasound (PA–US) catheter imaging provides a potential solution by combining molecular contrast with ultrasound-based structural imaging in an intraluminal format. By integrating optical excitation and acoustic detection within a miniaturized balloon catheter, PA–US imaging enables co-registered assessment of tissue composition and morphology during endoscopic examination.

This chapter presents the translational development of a PA–US balloon catheter imaging system, progressing from preclinical validation in a controlled fibrosis model to early human studies in CD.

5.2 Materials and Methods

5.2.1 Imaging System Configuration

The dual-modality PA–US imaging system used in this study is illustrated in Figure 5.1. The platform integrates a research US imaging system (Vantage 256, Verasonics Inc., USA) with a tunable optical parametric oscillator (OPO) laser (Opolette UX1020, Opotek Inc., USA) to enable synchronized PA and US imaging. The Verasonics system was used for signal acquisition, beamforming, and real-time image display, while the laser provided pulsed optical excitation for PA signal generation.

The OPO laser delivered nanosecond pulses with wavelength tunability across the near-infrared spectrum, enabling selection of excitation wavelengths targeting optical absorption of chromophores associated with inflammation and fibrosis. During imaging, the laser operated at a repetition rate of 20 Hz with pulse energies up to approximately 10 mJ. Laser output was coupled into the imaging catheter through a fiber-coupling assembly and delivered via an optical fiber for intraluminal illumination.

To ensure synchronization, the laser trigger output was used as an external timing signal for the Verasonics platform. Each laser pulse initiated a PA acquisition sequence, during which generated acoustic waves were received by the US array embedded in the catheter. Conventional US B-mode imaging was performed after each PA acquisition to provide co-registered anatomical information. US transmissions were scheduled approximately 20 μs after PA signal acquisition to avoid interference between PA and US signals.

This acquisition strategy enabled sequential PA and US imaging within each laser pulse cycle. PA signals provided information on optically absorbing chromophores, while US imaging provided structural context of the gastrointestinal wall. The synchronized acquisition enabled real-time co-registered molecular and anatomical imaging during endoscopic procedures.

The compact integration of the OPO laser with the Verasonics imaging system facilitated flexible configuration and enabled deployment of the PA–US catheter in an endoscopic imaging environment.

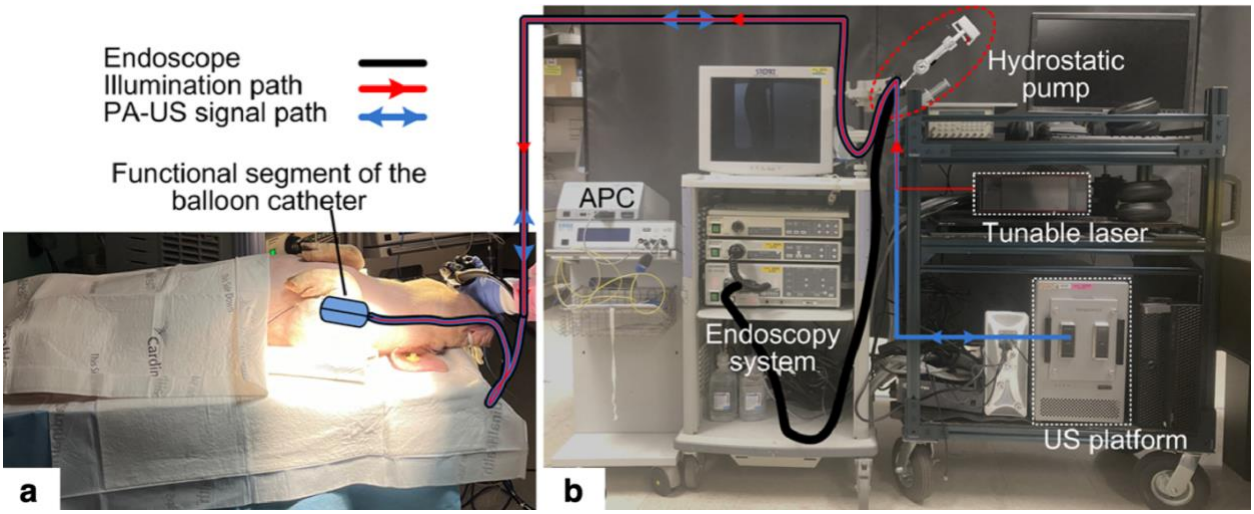


Figure 5.1 Schematic of the dual-modality PA–US imaging system and *in vivo* experimental setup. (a) The endoscopy platform allows insertion of the imaging catheter through the biopsy channel for either APC (animal experiments only) or PA–US imaging. (b) A tunable pulsed laser provides optical excitation for PA imaging, while the Verasonics system acquires PA and US signals, performs image reconstruction, and displays co-registered images in real time.

5.2.2 PA–US Balloon Catheter Design

The balloon catheter architecture is illustrated in Figure 5.2. The design builds upon our previously reported prototype [178] and was further refined to reduce catheter diameter and ensure compatibility with standard clinical endoscopes. The catheter integrates a custom-fabricated 48-element linear US array (Vermon, Tours, France) and an angle-polished multimode optical fiber for PA illumination. The US array has a pitch of 100 µm and a center frequency of approximately 9 MHz, providing a balance between spatial resolution and penetration depth in gastrointestinal tissue.

The flexible catheter shaft has an outer diameter of approximately 2 mm and a length of 2 m, enabling insertion through the biopsy channel of standard endoscopes while maintaining sufficient flexibility for navigation. Optical excitation is delivered through a 600 µm core multimode fiber (FT600EMT, NA ≈ 0.39, Thorlabs, NJ), with the distal tip angle-polished to generate side-firing illumination toward the bowel wall. The fiber is positioned adjacent to the US array to ensure spatial overlap between optical excitation and acoustic detection, maximizing PA signal collection efficiency.

US array and optical fiber are enclosed within a transparent hydrostatic balloon that provides acoustic coupling to the tissue surface. When inflated, the balloon has a diameter of approximately 12 mm and a length of approximately 15 mm, ensuring stable contact with the tissue.

A medical-grade heat-shrink tube (Nordson Medical, USA) encases the US array and optical fiber, providing electrical insulation and mechanical protection. The distal heat-shrink assembly connects proximally to a three-way stopcock that controls balloon inflation and deflation using a hydrostatic pump. During preparation, degassed water is introduced while residual air is evacuated to minimize acoustic artifacts. Figures 5.2b–c show the distal balloon section before and after inflation.

The spatial resolution of the catheter system was characterized using a 200 μm diameter polyethylene wire positioned at the balloon surface, as shown in Figure 5.3a–b. The measured axial and lateral full widths at half maximum were approximately 100–150 μm at the balloon surface.

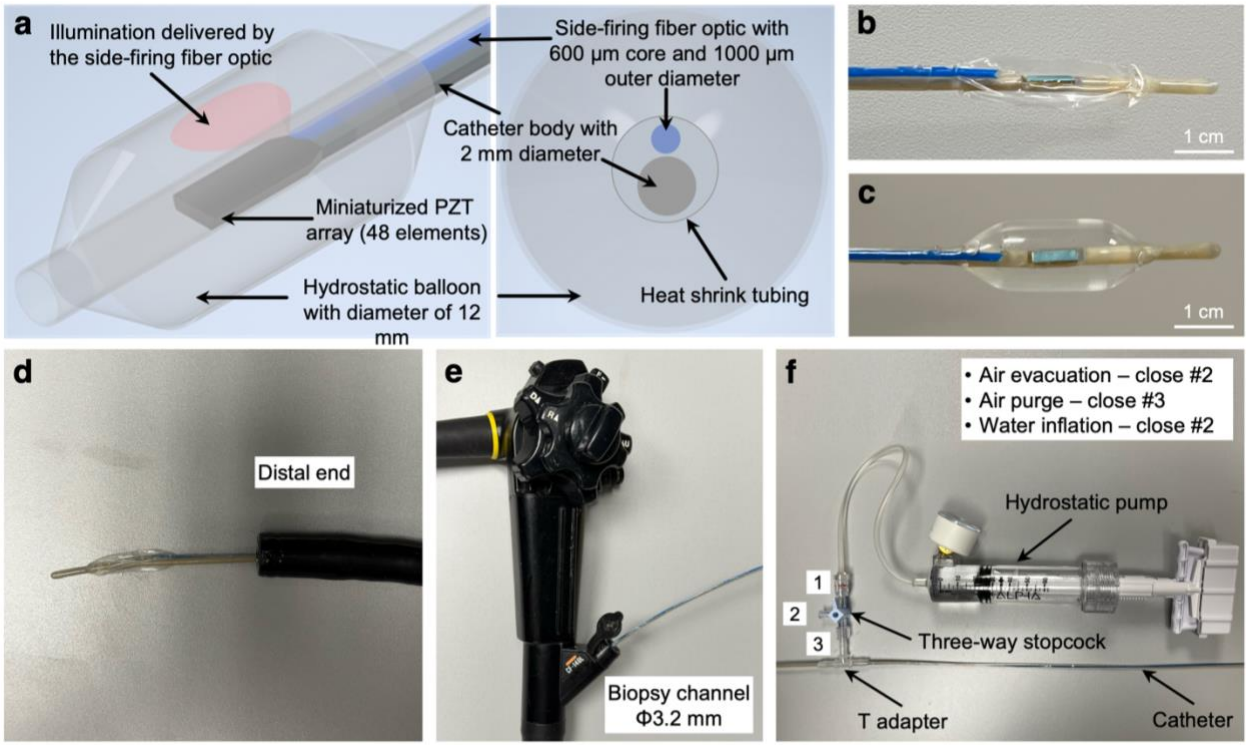


Figure 5.2 Schematics of the water-balloon catheter integrated with a clinical endoscope. (a) Schematic of the balloon section of the catheter with labeled components and dimensions. (b) and (c) Photographs of the distal balloon section before and after inflation, respectively. (d) Photograph showing the catheter extending from the distal end of the endoscope. (e) Photograph of the catheter inserted through the endoscope biopsy channel (3.2 mm in diameter). (f) Illustration of the balloon inflation process using a hydrostatic pump. Markers 1, 2, and 3 indicate the three ports of the three-way stopcock.

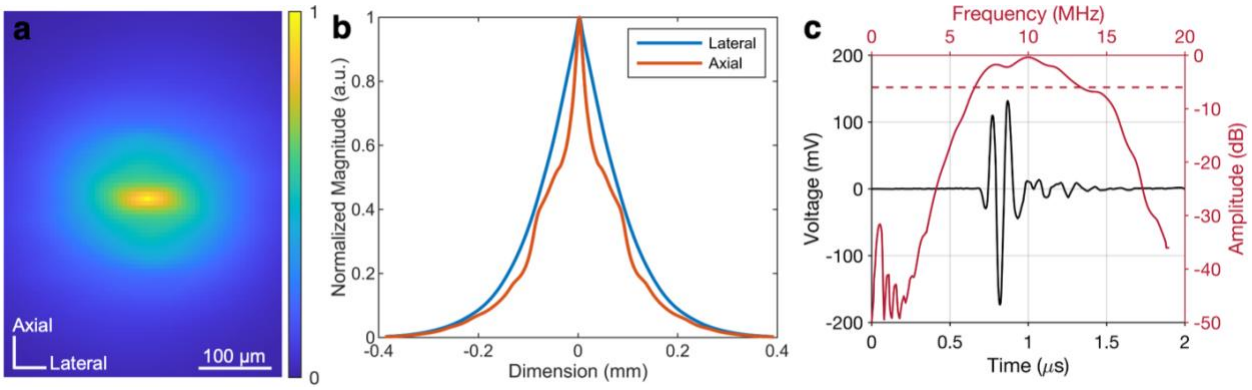


Figure 5.3 Spatial resolution and frequency response of the PA–US catheter. (a) PA image of the cross-section of a 200 µm black polyethylene wire positioned at the balloon surface. (b) Lateral and axial point spread functions at the balloon surface, derived from the image in (a) after deconvolution with the wire cross-sectional profile. The lateral and axial full widths at half maximum (FWHM) are 143 µm and 104 µm, respectively. (c) Representative radiofrequency signal from the catheter transducer (black) and its corresponding frequency spectrum (red), obtained from manufacturer-provided characterization data.

5.2.3 Porcine APC-Induced Esophageal Fibrosis Model

The porcine fibrosis model and representative endoscopic views of the argon plasma coagulation (APC) procedure are illustrated in Figure 5.4. Esophageal strictures were induced using APC, which produces controlled circumferential mucosal injury followed by fibrotic remodeling during healing. This approach generates localized strictures separated by normal esophageal segments, enabling within-animal comparisons.

Female domestic pigs (White Yorkshire × Landrace, 30–50 kg) were acclimated for at least three days prior to experimentation and fasted overnight before anesthesia induction. All procedures were performed using a clinical endoscope (Olympus CF140L).

Full circumferential mucosal lesions approximately 1 cm in length were created using 1–5 s APC bursts at 50 W with an argon flow rate of 0.5 L/min. Three to four lesions were generated per animal and separated by at least 10 cm of untreated esophagus to provide internal controls. Animals were monitored post-procedure and received supportive care, including dietary modification and reflux suppression. Fibrotic remodeling developed at treated sites after a 7–14 day healing interval (Figure 5.4c).

At study completion, animals were euthanized for histological analysis under institutional protocol PRO00011639, in accordance with guidelines from the Institutional Animal Care and Use Committee (IACUC), the American Veterinary Medical Association (AVMA), and the United States Department of Agriculture (USDA).

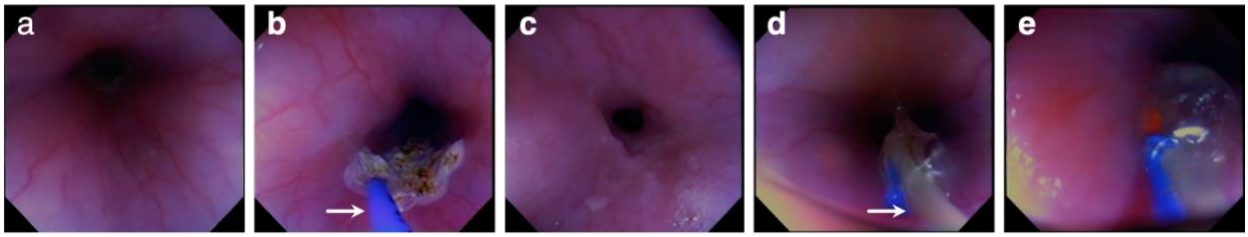


Figure 5.4 Endoscopic images of APC modeling and PA–US imaging procedures. (a) Normal esophageal tissue in the pig. (b) APC procedure, with the white arrow indicating the APC catheter that generates localized thermal coagulation for controlled mucosal injury. (c) The treated site 14 days after APC. (d) Endoscopic view of the balloon catheter (white arrow) inserted into the esophagus prior to inflation. (e) and (f) PA imaging at the target site using 800 nm illumination. The water-filled balloon conforms to the esophageal wall, ensuring effective acoustic coupling.

5.2.4 Spectroscopic PA Imaging

Multi-wavelength PA imaging was performed at 734, 757, 800, 1220, and 1310 nm. The shorter wavelengths target differential absorption of oxyhemoglobin and deoxyhemoglobin, while the longer wavelengths provide increased sensitivity to collagen absorption in fibrotic tissue. For each wavelength, PA frames were acquired sequentially under synchronized laser triggering.

Because PA signal amplitude is proportional to the local optical absorption coefficient, the measured PA signal at wavelength λ can be modeled as a linear combination of contributions from different chromophores:

$$PA(\lambda) = \sum_{i=1}^{N} \epsilon_i\,(\lambda) C_i \tag{12}$$

where $\epsilon_i(\lambda)$ denotes the molar absorption coefficient of chromophore i at wavelength λ, C_i represents its relative concentration, and N is the number of chromophores included in the spectral model. In this study, three chromophores were considered: HbO_2, HbR and collagen.

Based on this model, spectroscopic unmixing was performed using pixel-wise linear least-squares fitting to estimate the relative concentrations of HbO_2, HbR, and collagen [189, 190]. Total hemoglobin (HbT) was calculated as the sum of HbO_2 and HbR.

5.2.5 *In Vivo* Imaging Protocol in Animal and Human Studies

In vivo PA–US imaging was performed using a clinical endoscopic platform in both the porcine fibrosis model and human subjects. The balloon catheter was introduced through the biopsy channel of a standard endoscope and advanced to predefined regions of interest under direct endoscopic visualization. Representative endoscopic views of the APC procedure and catheter-based imaging are shown in Figure 5.4.

In the porcine model, imaging was performed at baseline prior to APC treatment and repeated after the 7–14 day healing interval described in Section 5.2.3. Both APC-treated strictures and untreated control segments within the same animal were examined to enable intra-subject comparisons.

At each imaging location, the balloon catheter (Figure 5.4d) was gradually inflated with degassed water to establish acoustic coupling and controlled contact with the esophageal wall. Multi-wavelength PA acquisition and US imaging were performed sequentially at stationary positions. For strain analysis, US radiofrequency data were continuously recorded during controlled balloon inflation and deflation. Representative PA images acquired at the target site are shown in Figure 5.4e–f. All animal procedures were conducted under the IACUC-approved protocol described in Section 5.2.3 (PRO00011639).

For the clinical translation study, PA–US imaging was performed in patients with CD undergoing clinically indicated ileocolonoscopy at Michigan Medicine under institutional review board (IRB) approval (HUM00233093). Written informed consent was obtained prior to participation. After routine endoscopic inspection, the catheter was positioned at regions of interest identified by the endoscopist, including areas of suspected stricture or inflammation. The same imaging protocol used in the animal study was applied, including multi-wavelength PA acquisition and controlled balloon inflation for strain measurement. To accommodate clinical workflow constraints, PA–US imaging was completed within approximately 15 minutes following routine endoscopic inspection and did not interfere with standard diagnostic or therapeutic procedures. Figure 5.5 shows the endoscopy suite and experimental setup used for the clinical PA–US imaging study.

Representative CD cases were targeted to evaluate the feasibility of the technique in clinically relevant scenarios. These included patients with terminal ileum involvement, one of the most common sites of CD. Postoperative patients with ileal pouch–anal anastomosis (IPAA), commonly referred to as a J pouch, were also included. In this procedure, the terminal ileum is folded into a J-shaped reservoir and connected to the anal canal to restore intestinal continuity after colectomy. Anastomotic narrowing or fibrotic strictures may develop at the pouch outlet or adjacent ileal segments, providing clinically relevant targets for imaging. These scenarios are clinically important because distinguishing inflammatory activity from fibrotic remodeling is critical for guiding treatment decisions.

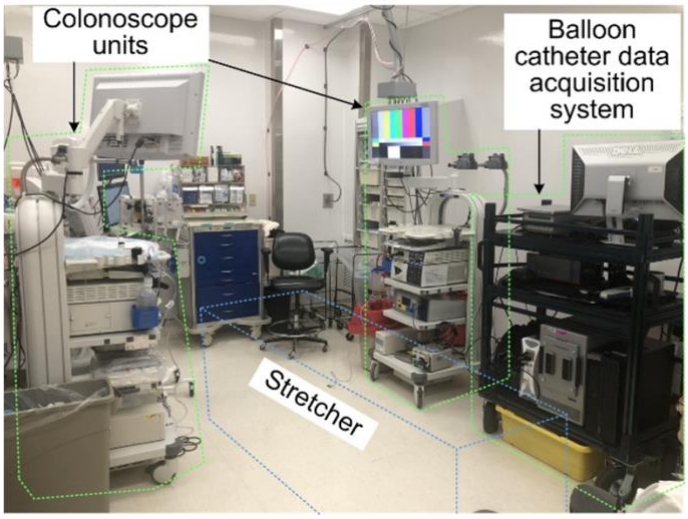


Figure 5.5 Clinical endoscopy suite and experimental setup for *in vivo* PA–US imaging during human endoscopic procedures.

5.2.6 Histological Processing and Evaluation

For the porcine model, the esophagus extending from approximately 1 cm distal to the soft palate to 1 cm proximal to the lower esophageal sphincter was harvested at study completion. Tissue segments corresponding to PA–US imaging locations were dissected, rinsed, photographed, and fixed in 10% neutral buffered formalin. Following fixation, samples were processed for paraffin embedding and sectioning.

Hematoxylin and eosin (H&E) staining was performed to assess inflammatory changes, and Masson's trichrome staining was used to evaluate collagen deposition and fibrotic remodeling. Digital photomicrographs were acquired using a light microscope (Olympus BX51, University of Michigan Microscopy and Image Analysis Laboratory).

Inflammation and fibrosis were independently evaluated by a board-certified veterinary pathologist blinded to the imaging results. Inflammation was assessed on H&E-stained sections, and fibrosis was graded on trichrome-stained sections [191] using a semiquantitative scale from 0 to 4. Detailed scoring criteria are provided in Table 5.1.

For human studies, tissue samples obtained during clinically indicated endoscopic procedures were processed according to standard pathology protocols. Trichrome staining was used to evaluate collagen deposition in regions corresponding to imaged sites when available, with histological interpretation performed by pathology personnel blinded to the imaging findings.

5.2.7 Data Processing

All PA and US radiofrequency data were beamformed offline using a DAS beamforming algorithm implemented in MATLAB (R2022b, MathWorks, USA). The reconstructed PA and US images were inherently co-registered due to synchronized acquisition.

Prior to quantitative analysis, PA signal amplitudes were normalized to account for wavelength-dependent laser energy variations. Spectroscopic analysis was performed on beamformed PA images using pixel-wise linear least-squares fitting across the five excitation wavelengths described. Relative concentrations of HbO_2, HbR and collagen were estimated based on known optical absorption spectra, and HbT was computed as the sum of HbO_2 and HbR.

The resulting parametric maps were overlaid on corresponding US images for anatomical reference. Regions of interest (ROIs) were defined along the bowel wall using co-registered B-mode US images to ensure consistent anatomical localization. Mean chromophore values were extracted within each ROI for comparison across experimental conditions.

Group comparisons were performed using two-sided nonparametric Wilcoxon rank-sum tests [192] due to limited sample sizes and non-normal data distributions. Statistical significance was defined as $p < 0.05$.

5.3 Results

5.3.1 Histological Inflammation and Fibrosis in the Pig APC Model

Blinded histopathological analysis was performed to assess inflammation and fibrosis in normal and APC-treated sections of the pig esophagus (Figure 5.6). APC-treated lesions showed increased inflammation and fibrosis compared to normal esophageal tissue.

Inflammation scores were higher in APC-treated esophageal lesions than in normal, untreated locations (0.1 vs. 2.2, $p < 0.001$). Histological fibrosis showed greater variability but was also higher in APC-treated lesions compared with untreated regions (0.25 vs. 1.89, $p < 0.001$).

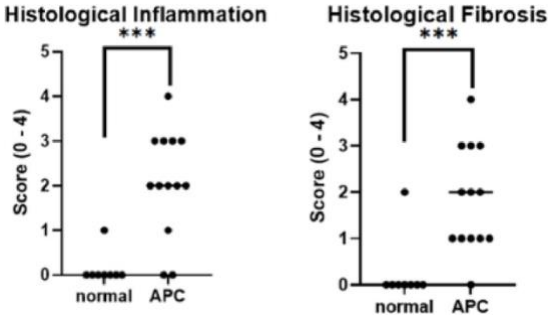


Figure 5.6 Histological scoring of normal (no APC) and APC-treated esophageal segments in the porcine model. Inflammation and fibrosis were evaluated using H&E staining and Masson's trichrome staining, respectively, and graded on a semiquantitative 0–4 scale. Scoring was performed in a blinded manner. Statistical comparisons were conducted using two-sided Wilcoxon rank-sum tests. *** $p < 0.001$.

Table 5.1. Histology scoring system.

Score	Inflammation	Fibrosis
0	Within normal limit	Within normal limit
1	Mild, multifocal inflammation in the lamina propria (<10% area)	Multifocal fibrosis of lamina propria and submucosa (<10% area)
2	Moderate, multifocal to coalescing inflammation in the lamina propria and mild extension to submucosa (10-40% area)	Multifocal to coalescing fibrosis of lamina propria and submucosa (10-40% area); muscularis mucosa and submucosal glands are remaining
3	Severe, massive inflammation in the lamina propria and submucosa (40-70% area)	Widespread fibrosis at the lamina propria and submucosa (40-70% area) with small extension to muscularis externa; muscularis mucosa and submucosal glands area obliterated by fibrosis
4	Severe, transmural inflammation including lamina propria, submucosa, and muscularis externa (>70% area)	Severe, transmural fibrosis including layers of lamina propria, submucosa, and muscularis externa (<70% area); muscularis mucosa, submucosal glands, and segment of muscularis externa are replaced by fibrosis

5.3.2 Measurement Stability and Reproducibility

The consistency of PA measurements across esophageal locations within the same animal is summarized in Figure 5.7. Average multispectral PA signal magnitudes of the esophageal wall were analyzed at baseline (T1) and 14 days after APC treatment (T2). At baseline, PA signal magnitudes measured at different esophageal positions showed minimal variation. Untreated control locations showed signal levels comparable to baseline measurements.

In contrast, APC-treated locations exhibited higher PA signal magnitudes and greater variability. The standard errors of the PA signal magnitudes at 800 nm were 1.21%, 1.91%, and 3.04% of the average magnitudes at baseline, untreated, and APC-treated locations, respectively. At 1310 nm, the corresponding standard errors were 0.77%, 3.05%, and 4.59%.

The root-mean-square differences between measurements at untreated locations and baseline measurements at the same positions were 1.03% of the average signal at 800 nm and 2.33%

at 1310 nm. These results indicate high measurement stability at baseline and untreated locations, with increased signal magnitude and variability at APC-treated sites.

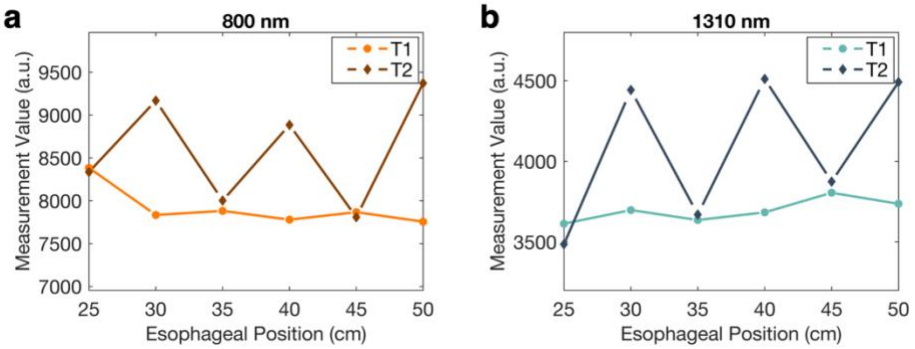


Figure 5.7 Validation of measurement consistency in PA signals acquired with the dual-modality imaging catheter. (a) Average PA signal magnitudes of the esophageal wall at baseline (T1), measured at multiple esophageal positions (25–50 cm). (b) PA signal magnitudes measured 14 days after APC treatment (T2). Positions at 30, 40, and 50 cm were APC-treated, while positions at 25, 35, and 45 cm served as untreated controls.

5.3.3 Structural and Molecular Imaging of the Pig Esophagus Using US and PA

Representative B-mode US and spectrally unmixed PA images of the porcine esophagus are shown in Figure 5.8, including baseline measurements, untreated control locations, and APC-treated locations acquired 14 days after the procedure. B-mode US images show structural changes in the esophageal wall following APC treatment. Compared with baseline and untreated locations, APC-treated regions exhibit increased wall thickness, indicating tissue remodeling associated with the injury and healing process. The treated locations also show elevated echogenicity within the esophageal wall, suggesting changes in tissue composition and mechanical properties consistent with fibrotic remodeling.

Spectroscopic PA images provide complementary molecular information by resolving the spatial distributions of hemoglobin and collagen within the esophageal wall. Hemoglobin signals are observed throughout the mucosal and submucosal layers. Collagen signals are more prominent within deeper layers in treated regions. Compared with baseline and untreated locations, APC-treated areas exhibit higher signal intensity in both hemoglobin and collagen.

Histological sections stained with Masson's trichrome (rightmost column in Figure 5.8) show collagen deposition at APC-treated locations. The trichrome staining reveals substantial collagen deposition within the esophageal wall, particularly in regions corresponding to the PA imaging field of view. These findings are consistent with the spatial distributions of hemoglobin and collagen observed in PA imaging.

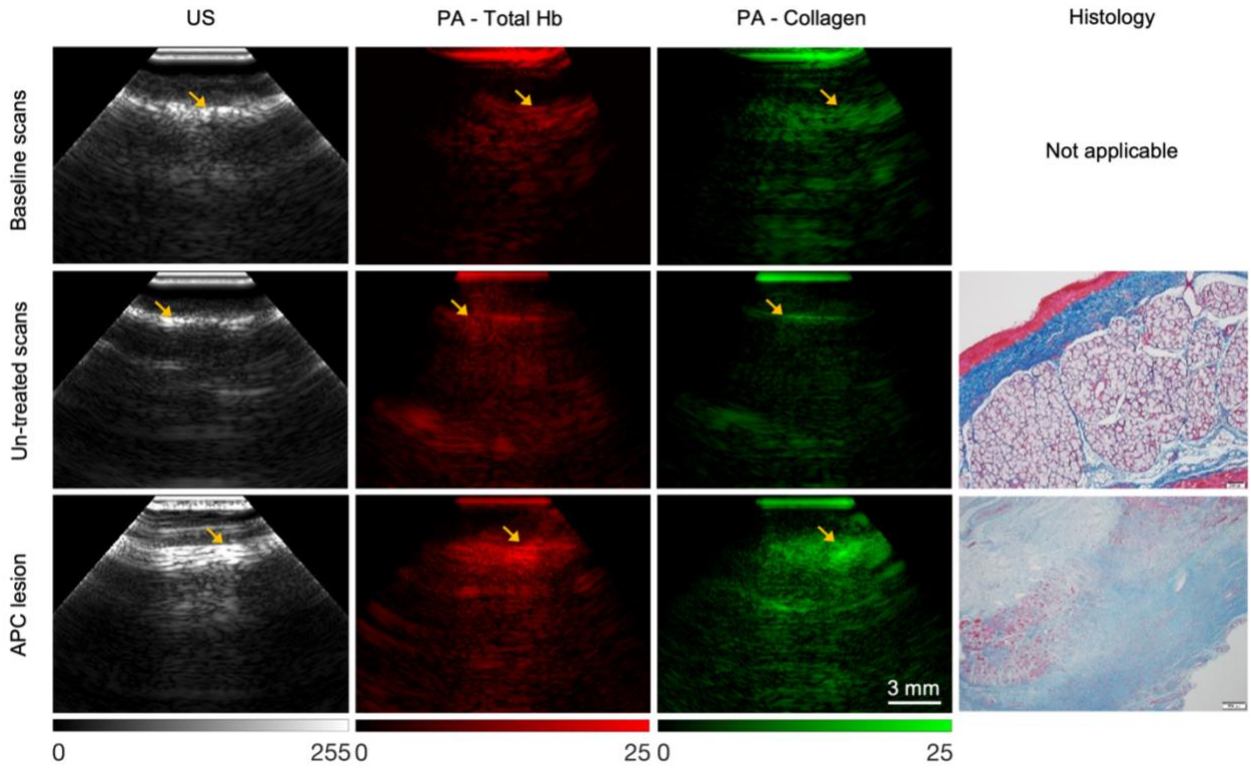


Figure 5.8 Representative US and PA images of the porcine esophagus. (a–c) Conventional B-mode US images of baseline (before treatment), untreated control, and APC-treated locations (14 days after APC), respectively. (d–f) Spectrally unmixed PA images showing relative HbT distributions. (g–i) Spectrally unmixed PA images showing relative collagen distribution. (j–k) Corresponding Masson's trichrome histological sections collected during necropsy. Solid black arrows denote blood vessels, and single white arrows mark normal structural collagen. Double white arrows indicate areas of pathological collagen deposition and transmural fibrosis. Arrows in (a–i) indicate the balloon–tissue interface. Scale bars: 3 mm for US and PA images. Histology scale bars: untreated control = 200 μm, APC lesion = 500 μm.

5.3.4 Quantitative Molecular Analysis

Group-level quantification of tissue chromophore signals derived from spectroscopic PA measurements is summarized in Figure 5.9. Relative HbT and collagen signals did not differ significantly between baseline and untreated control locations. In contrast, APC-treated locations exhibited higher HbT and collagen signals than both baseline and untreated control locations.

Compared with baseline measurements, APC-treated locations showed increases of 3.12 units in HbT signal ($p < 0.001$) and 8.58 units in collagen signal ($p < 0.001$). Relative to untreated control locations, HbT and collagen signals at APC-treated sites were higher by 3.53 units ($p < 0.001$) and 8.18 units ($p < 0.001$), respectively.

APC-treated locations also showed greater variability in HbT and collagen signals compared with baseline and control groups. These findings are consistent with the imaging results shown in Figure 5.8.

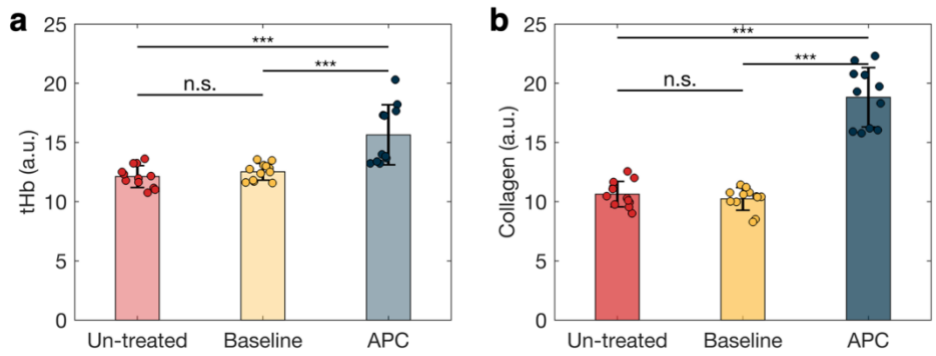


Figure 5.9 Quantitative comparison of chromophore signals derived from spectroscopic PA imaging. (a) Relative HbT signals measured at baseline, untreated control, and APC-treated locations. (b) Relative collagen signals measured in the same groups. Error bars represent mean ± SD across position-level samples, and dots indicate individual measurements. Statistical comparisons were performed using two-sided Wilcoxon rank-sum tests. *** $p < 0.001$, ** $p < 0.01$, * $p < 0.05$, n.s. = not significant.

5.3.5 Feasibility of *In Vivo* Imaging in a Human Subject

Representative images acquired during clinical ileocolonoscopy in a patient with CD are shown in Figure 5.10. Imaging was performed at an anal canal anastomotic stricture distal to a J pouch, as well as at a non-fibrotic and non-inflamed ileal segment proximal to the stricture for comparison. The imaging catheter was introduced through the biopsy channel of a standard clinical endoscope and positioned at the target locations under direct endoscopic visualization.

White-light endoscopic images show the deployment of the PA–US catheter within the intestinal lumen, with the hydrostatic balloon inflated to establish acoustic coupling between the catheter and the bowel wall. This configuration allowed stable contact with the bowel wall during imaging.

US B-mode images delineate the inner and outer boundaries of the bowel wall, providing structural information about the intestinal layers. Both US and PA imaging show penetration through the intestinal wall, enabling visualization of transmural features. PA images provide spectroscopic contrast associated with the molecular composition of the tissue.

Compared with the non-fibrotic ileal segment, the anastomotic stricture location shows higher relative HbT and collagen signals in the spectroscopic PA images. The increased HbT signal is consistent with increased vascularity and inflammatory activity, while the elevated collagen signal is consistent with fibrotic changes at the stricture site.

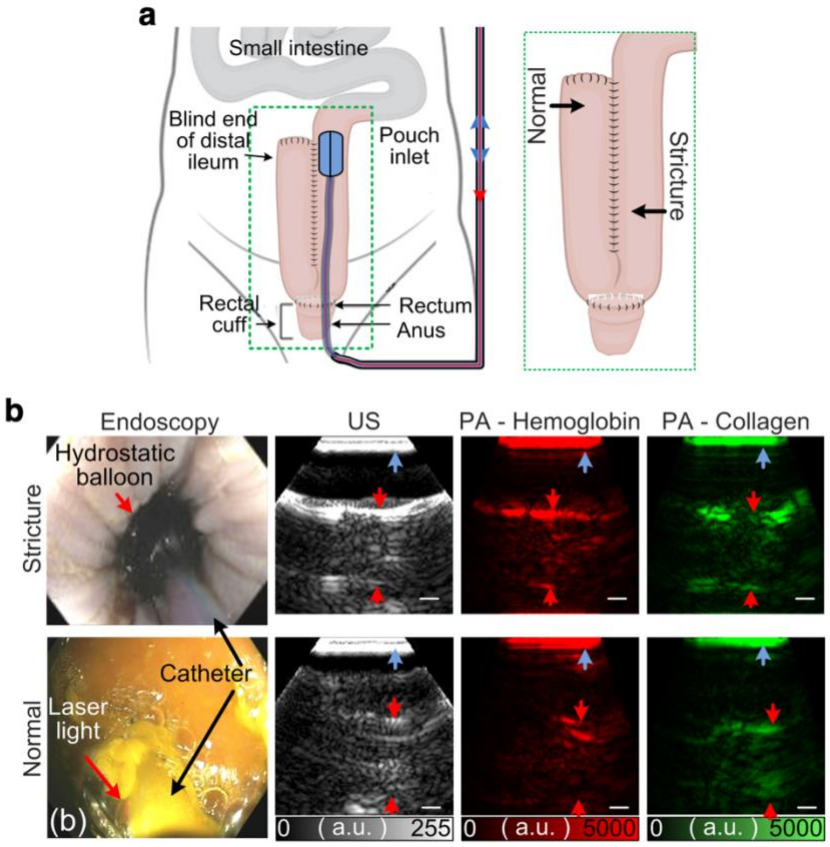


Figure 5.10 *In vivo* PA–US imaging of intestinal tissue in a CD patient. (a) Schematic illustration of the J-pouch anatomy and the location of the anal canal anastomotic stricture. (b) Images acquired at an anal canal anastomotic stricture distal to the J pouch (top row) and from a non-fibrotic, non-inflamed ileal segment proximal to the stricture (bottom row). White-light endoscopic images show the catheter and hydrostatic balloon when fully deployed. In the US and PA images, blue arrows indicate the US transducer array located at the top of the images, and red arrows mark the inner and outer surfaces of the bowel wall. Scale bar: 1 mm.

5.4 Discussion and Conclusions

This study demonstrates that the dual-modality PA–US balloon catheter enables characterization of structural, vascular, and fibrotic changes in the gastrointestinal wall *in vivo*. In the porcine APC model, APC-treated segments showed increased wall thickness, elevated HbT signals, and higher collagen signals compared with untreated controls, with spatial correspondence to histological findings. Baseline and untreated sites showed stable measurements, supporting the reproducibility of the acquisition and processing pipeline.

By combining US morphology with spectroscopic PA contrast, the system provides complementary structural and molecular information beyond what is available with conventional endoscopy or US alone. The balloon catheter design enables stable acoustic coupling and allows controlled mechanical loading of the bowel wall, supporting integration of strain-based assessment with molecular imaging.

In the human case, the PA–US catheter was successfully deployed during routine endoscopy. The imaging results showed sufficient penetration and contrast to visualize the intestinal wall and to differentiate a fibrotic stricture from adjacent non-fibrotic bowel. Although limited to a single case, these findings support the technical feasibility and clinical compatibility of the platform.

Several limitations should be noted. First, spectroscopic analysis provides relative rather than absolute chromophore quantification. Future work may incorporate calibration strategies to improve quantitative accuracy. The current clinical evaluation remains limited, and larger studies are needed to assess diagnostic performance and inter-patient variability.

Overall, this work demonstrates a translational imaging approach for transmural assessment of inflammation and fibrosis in CD. By enabling simultaneous structural, vascular, and molecular characterization of the bowel wall, the proposed PA–US catheter may improve identification of fibrostenotic disease and inform clinical decision-making in CD.

Chapter 6 Conclusions and Future Work

6.1 Key Findings in iRAI Studies

6.1.1 Volumetric iRAI–US Visualization

First, a dual-modality volumetric iRAI–US imaging system was developed to visualize radiation dose deposition co-registered with anatomical structures during radiotherapy. Phantom experiments showed that the system can capture radiation dose deposition aligned with anatomical structures under respiratory motion conditions, with a co-registration error of 0.45 mm. The study further investigated how motion direction, motion speed, motion range, and US imaging frame rate influence the accuracy of dose mapping, both without and with ultrasound-guided motion correction.

In vivo studies further demonstrated real-time volumetric dose-on-anatomy imaging in a rabbit liver model. The results enabled direct observation of spatial misalignment between delivered dose and the intended treatment target, suggesting potential for motion-aware monitoring in adaptive radiotherapy.

6.1.2 Quantitative iRAI via Sensitivity Compensation

Second, a transducer sensitivity compensation method was introduced to address spatially varying detection sensitivity in matrix-array-based iRAI systems. Numerical and phantom studies showed that variations in transducer detection sensitivity can introduce systematic differences in reconstructed iRAI signal amplitude and reduce agreement with the true radiation dose distribution. Incorporating experimentally measured transducer sensitivity into the reconstruction improved the agreement between reconstructed iRAI images and planned dose distributions and produced more uniform signal across the imaging field, supporting a more quantitative interpretation of iRAI measurements.

6.1.3 Dose Mapping Under Clinical Delivery Scenarios

Third, iRAI performance was evaluated in an anthropomorphic abdominal phantom under clinically relevant treatment conditions to assess the influence of delivery methods and target locations on radiation dose mapping. The reconstructed images showed distinct dose deposition patterns across treatment plans and anatomical regions. Dose mapping accuracy was higher for VMAT than for 3DCRT and IMRT. Reconstruction was more reliable in soft tissue with clear acoustic access, while accuracy decreased near bone structures and in deeper targets due to acoustic attenuation and limited detection aperture.

6.2 Key Findings in PA–US Catheter Imaging

A biopsy-channel-compatible PA–US balloon catheter was developed for intraluminal imaging of gastrointestinal tissue. Spectroscopic PA imaging of HbT and collagen enabled *in vivo* differentiation between inflammatory and fibrotic tissue features in a porcine model.

In a human study, the catheter was deployed through the biopsy channel of a standard clinical endoscope, enabling intraluminal imaging within a routine workflow. Imaging of a strictured bowel segment showed elevated HbT and collagen signals compared with a nearby non-fibrotic ileal region. Together, these findings support the feasibility of PA–US imaging for distinguishing inflammation from fibrosis in CD in a clinical endoscopic setting.

6.3 Overall Scientific Contributions

6.3.1 Contributions to iRAI and Radiotherapy Dosimetry

This work advances iRAI toward practical and quantitative radiotherapy applications. It presents, to our knowledge, the first volumetric iRAI–US framework for 3D dose-on-anatomy visualization during treatment. It also marks an initial step toward quantitative iRAI by incorporating transducer sensitivity into the reconstruction framework. In addition, this work begins to systematically examine iRAI performance under different anatomical configurations and radiotherapy delivery methods.

Compared with current clinical dosimetry techniques that rely on indirect measurements or post-treatment verification, iRAI provides real-time volumetric mapping of delivered dose within tissue. With further improvements in reconstruction accuracy and system implementation,

iRAI has the potential to complement existing dosimetry tools and support treatment monitoring and adaptive radiotherapy.

6.3.2 Contributions to Crohn's Disease Diagnosis and Characterization

This work advances PA–US imaging for *in vivo* characterization of inflammation and fibrosis in CD through animal and human studies. The approach enables intraluminal assessment of tissue composition beyond the mucosal surface, providing access to structural and molecular features associated with underlying disease processes. These features are particularly relevant in conditions such as intestinal strictures and postoperative bowel segments, where distinguishing inflammatory activity from fibrotic changes is critical for guiding treatment decisions. Overall, this approach extends endoscopic evaluation by enabling transmural molecular and structural information, offering a complementary imaging strategy to current diagnostic methods.

6.4 Limitations

6.4.1 Limitations of iRAI Studies

First, during beamforming, current approaches generally assume a homogeneous and isotropic acoustic medium. In practice, biological tissues are heterogeneous and layered, introducing scattering, refraction, and attenuation during acoustic propagation [193, 194]. These effects are not yet fully considered in the reconstruction process and can introduce non-negligible errors in the recovered dose distribution.

Second, the present system uses rigid US transducer arrays, which limit acoustic coupling and adaptability to different anatomical geometries. Although coupling media such as water balloons or solid coupling agents were used, the coupling quality remains suboptimal. In addition, the imaging angle is restricted, as the transducer array is typically positioned on only one side of the animal or patient. These constraints can reduce signal detection efficiency.

Third, the current iRAI implementation primarily provides relative dose mapping rather than absolute dose quantification. Clinical radiotherapy applications ultimately require accurate absolute dose measurements, which will require further development of calibration strategies and more quantitative reconstruction methods.

6.4.2 Limitations of the Current PA–US Catheter

First, the current PA–US catheter implementation introduces limitations in optical illumination and acoustic detection. The small catheter size limits optical fiber placement and illumination angles, leading to non-uniform light distribution and reduced optical energy delivery to deeper tissue layers. In addition, acoustic signals are primarily detected from one side of the bowel wall, resulting in a limited detection view.

Second, the present study includes a limited number of endoscopic imaging cases in patients. Larger clinical studies are needed to evaluate diagnostic performance and assess robustness in a larger patient cohort.

6.5 Future Directions

6.5.1 iRAI Future Work

Several directions can further advance the development of iRAI for radiotherapy applications. First, future reconstruction methods should account for acoustic heterogeneity in biological tissues, including effects such as scattering, refraction, and attenuation during wave propagation. Incorporating these properties into beamforming may improve the accuracy of dose reconstruction in realistic anatomical structures.

Second, improved transducer configurations and acoustic coupling strategies may enhance signal detection. Flexible or conformable transducer arrays and multi-angle detection geometries could help address the limited-view problem and improve signal coverage.

Third, future studies should focus on developing quantitative reconstruction methods for absolute dose measurement, which is essential for clinical translation. Developing reliable calibration strategies and integrating iRAI with treatment planning information may further improve the accuracy of dose estimation during radiotherapy.

6.5.2 Future Directions for Endoscopic PA–US Catheter

First, optimization of fiber arrangement and transducer configuration can help improve light delivery uniformity and acoustic detection coverage, which in turn enhances imaging depth and signal quality in deeper intestinal tissue. Second, improved spectroscopic analysis may enable more robust molecular characterization. Enhanced spectral unmixing and calibration methods could improve the quantification of HbT and collagen signals, supporting more reliable assessment

of inflammation and fibrosis. Third, larger clinical studies are needed to evaluate diagnostic performance and clinical utility in CD.

6.6 Concluding Remarks

This dissertation investigated acoustic-based imaging technologies for two biomedical applications: radiotherapy dose monitoring and characterization of CD. Through system development, validation in phantom and animal models, and initial translational studies, this work demonstrates that acoustically generated signals can capture *in vivo* radiation dose deposition and tissue composition not accessible with conventional anatomical imaging. These approaches enable visualization of processes within tissue, including radiation dose deposition during therapy and molecular features associated with inflammation and fibrosis.

For radiotherapy applications, the studies collectively advance iRAI toward more practical dose monitoring. By integrating acoustic detection with ultrasound-based anatomical imaging and improving the quantitative interpretation of iRAI signals, this work provides a framework for visualizing dose deposition relative to anatomy and evaluating performance under clinically relevant conditions. For gastrointestinal applications, the development of an endoscopy-compatible PA–US imaging catheter demonstrates the feasibility of intraluminal molecular imaging during endoscopy. Together, these studies highlight the potential of acoustic-based imaging technologies to provide structural, functional, and molecular information in biomedical imaging. With continued technical development and clinical validation, these approaches may support improved monitoring in radiotherapy and more effective characterization of inflammation and fibrosis in CD.

Bibliography

[1] I. Soerjomataram and F. Bray, "Planning for tomorrow: global cancer incidence and the role of prevention 2020–2070," *Nature reviews Clinical oncology,* vol. 18, no. 10, pp. 663-672, 2021.

[2] H. Fink *et al.*, "Global and regional cancer burden attributable to modifiable risk factors to inform prevention," *Nat. Med.,* pp. 1-10, 2026.

[3] S. A. Raza, "Emerging trends in global cancer epidemiology," vol. 17, ed: MDPI, 2025, p. 1483.

[4] K. Eskandar, "The evolving role of surgery in multimodal cancer treatment: a comprehensive review," *Хирургия и онкология,* vol. 14, no. 4, pp. 55-62, 2024.

[5] Z. Abbas and S. Rehman, "An overview of cancer treatment modalities," *Neoplasm,* vol. 1, pp. 139-157, 2018.

[6] W. Fan, B. Yung, P. Huang, and X. Chen, "Nanotechnology for multimodal synergistic cancer therapy," *Chem. Rev.,* vol. 117, no. 22, pp. 13566-13638, 2017.

[7] V. Ahire *et al.*, "Radiobiology of combining radiotherapy with other cancer treatment modalities," in *Radiobiology textbook*: Springer, 2023, pp. 311-386.

[8] D. Cummings, J. Wong, R. Palm, S. Hoffe, K. Almhanna, and S. Vignesh, "Epidemiology, diagnosis, staging and multimodal therapy of esophageal and gastric tumors," *Cancers (Basel),* vol. 13, no. 3, p. 582, 2021.

[9] E. Filoni, V. Musci, A. Di Rito, R. Inchingolo, R. Memeo, and F. Mannavola, "Multimodal management of colorectal liver metastases: state of the art," *Oncol. Rev.,* vol. 17, 2023.

[10] R. C. Pestana and N. K. Ibrahim, "Cancer treatment modalities systemic and locoregional approaches: Challenges and opportunities of multidisciplinary approaches," *Locoregional Radionuclide Cancer Therapy: Clinical and Scientific Aspects,* pp. 17-37, 2020.

[11] T. Kron, J. Lehmann, and P. B. Greer, "Dosimetry of ionising radiation in modern radiation oncology," *Phys. Med. Biol.,* vol. 61, no. 14, pp. R167-R205, 2016.

[12] B. Mijnheer, S. Beddar, J. Izewska, and C. Reft, "In vivo dosimetry in external beam radiotherapy," *Med. Phys.,* vol. 40, no. 7, p. 070903, 2013.

[13] I. Olaciregui-Ruiz *et al.*, "In vivo dosimetry in external beam photon radiotherapy: Requirements and future directions for research, development, and clinical practice," *Physics and imaging in radiation oncology,* vol. 15, pp. 108-116, 2020.

[14] J. Bertholet *et al.*, "Real-time intrafraction motion monitoring in external beam radiotherapy," *Phys. Med. Biol.,* vol. 64, no. 15, p. 15TR01, 2019.

[15] J. C. Chow and H. E. Ruda, "In vivo dosimetry in radiotherapy: Techniques, applications, and future directions," *Encyclopedia,* vol. 5, no. 1, p. 40, 2025.

[16] M. Esposito *et al.*, "Estimating dose delivery accuracy in stereotactic body radiation therapy: a review of in-vivo measurement methods," *Radiother. Oncol.,* vol. 149, pp. 158-167, 2020.

[17] F. Romano, C. Bailat, P. G. Jorge, M. L. F. Lerch, and A. Darafsheh, "Ultra-high dose rate dosimetry: challenges and opportunities for FLASH radiation therapy," *Med. Phys.,* vol. 49, no. 7, pp. 4912-4932, 2022.
[18] S. D'Alessio, F. Ungaro, D. Noviello, S. Lovisa, L. Peyrin-Biroulet, and S. Danese, "Revisiting fibrosis in inflammatory bowel disease: the gut thickens," *Nature Reviews Gastroenterology & Hepatology,* vol. 19, no. 3, pp. 169-184, 2022.
[19] A. K. Shergill *et al.*, "The role of endoscopy in inflammatory bowel disease," *Gastrointest. Endosc.,* vol. 81, no. 5, pp. 1101-1121. e13, 2015.
[20] C. M. Spiceland and N. Lodhia, "Endoscopy in inflammatory bowel disease: Role in diagnosis, management, and treatment," *World J. Gastroenterol.,* vol. 24, no. 35, p. 4014, 2018.
[21] Q. Fu, R. Zhu, J. Song, H. Yang, and X. Chen, "Photoacoustic imaging: contrast agents and their biomedical applications," *Advanced Materials,* vol. 31, no. 6, p. 1805875, 2019.
[22] L. E. Iannucci, C. S. Dranoff, M. A. David, and S. P. Lake, "Optical imaging of dynamic collagen processes in health and disease," *Frontiers in Mechanical Engineering,* vol. 8, p. 855271, 2022.
[23] J. Weber, P. C. Beard, and S. E. Bohndiek, "Contrast agents for molecular photoacoustic imaging," *Nature methods,* vol. 13, no. 8, pp. 639-650, 2016.
[24] V. Johariya, A. Joshi, N. Malviya, and S. Malviya, "Introduction to cancer," in *Medicinal plants and cancer chemoprevention*: CRC Press, 2023, pp. 1-28.
[25] S. Sriharikrishnaa, P. S. Suresh, and S. Prasada K, "An introduction to fundamentals of cancer biology," in *Optical Polarimetric modalities for biomedical research*: Springer, 2023, pp. 307-330.
[26] S. H. Wani and S. A. Lone, *Cancer: Diseases*. Educreation Publishing, 2018.
[27] S. Sarkar *et al.*, "Cancer development, progression, and therapy: an epigenetic overview," *Int. J. Mol. Sci.,* vol. 14, no. 10, pp. 21087-21113, 2013.
[28] I. Beerman and D. J. Rossi, "Epigenetic control of stem cell potential during homeostasis, aging, and disease," *Cell stem cell,* vol. 16, no. 6, pp. 613-625, 2015.
[29] F. Bray, M. Laversanne, E. Weiderpass, and I. Soerjomataram, "The ever-increasing importance of cancer as a leading cause of premature death worldwide," *Cancer,* vol. 127, no. 16, pp. 3029-3030, 2021.
[30] G. B. o. D. C. Collaboration, "Global, regional, and national cancer incidence, mortality, years of life lost, years lived with disability, and disability-adjusted life-years for 29 cancer groups, 1990 to 2017: a systematic analysis for the global burden of disease study," *JAMA oncology,* vol. 5, no. 12, pp. 1749-1768, 2019.
[31] Z. Burkitbayev *et al.*, "Cancer trends in Central Asia from 1990 to 2021: Analysis of the global burden of disease study. Electron J Gen Med. 2026; 23 (2): em718," vol. 23, ed, 2026, p. 2.
[32] A. Hammond *et al.*, "Hematologic cancers in the SAARC region: current burden in 2022 and projections to 2050," *Blood Global Hematology,* vol. 2, no. 1, p. 100036, 2026.
[33] A. Nadaf *et al.*, "Community Perception of Cancer Awareness and Treatment Modalities in North Karnataka, India-A Cross Sectional Study," *Journal of Advanced Scientific Research,* vol. 17, no. 02, pp. 20-34, 2026.
[34] Y. Chen *et al.*, "Burden of Middle-Aged and Elderly Patients With Non-Hodgkin Lymphoma From 1990 to 2021: A Systematic Analysis Based on the Global Burden of Disease 2021," *Cancer Medicine,* vol. 15, no. 3, p. e71609, 2026.

[35] G. Ferrari Ardicini *et al.*, "Trends and Future Projections of Cancer Prevalence in Patients with Cardiovascular Admissions," *European Heart Journal Open,* p. oeag030, 2026.
[36] Y. Wu *et al.*, "Mapping Burdens and Inequalities of Polycystic Ovary Syndrome in Young Female across 953 Locations 1990 to 2040 with Deep Learning Forecasts," *iScience,* 2026.
[37] P. Marino *et al.*, "Healthy lifestyle and cancer risk: modifiable risk factors to prevent cancer," *Nutrients,* vol. 16, no. 6, p. 800, 2024.
[38] S. M. Sakthisankaran, D. Sakthipriya, and M. Swamivelmanickam, "Health Risks Associated with Tobacco Consumption in Humans: An Overview," *Journal of Drug Delivery & Therapeutics,* vol. 14, no. 5, 2024.
[39] M. Y. Murshid, E. M. Murshid, N. Bukhari, M. Alfayez, T. Salah, and Y. Bahadur, "The rising burden of obesity-linked cancers in Saudi Arabia: a public health review," *Annals of Medicine and Surgery,* vol. 88, no. 3, pp. 2335-2347, 2026.
[40] J. K. Muruganantham and R. Veerabathiran, "An Overview of Diabetes and Cancer Risks: Types and Mechanisms," *Diabetes and Cancer: Association, Mechanism, and Therapeutic Implications,* pp. 1-16, 2026.
[41] R. Raghavan, *Environmental Factors in Carcinogenesis: Exposome-Driven Insights Into Cancer Risk and Prevention: Exposome-Driven Insights Into Cancer Risk and Prevention*. IGI Global, 2025.
[42] M. S. Rahman, S. Suresh, and M. I. Waly, "Risk factors for cancer: Genetic and environment," in *Bioactive components, diet and medical treatment in cancer prevention*: Springer, 2018, pp. 1-23.
[43] C. Zhang, Q. Shao, J. Liu, F. Zhang, Y. Li, and Z. Huang, "Current status and advances in research on the impact and mechanisms of atmospheric pollutants on gastric cancer: a narrative review," *Translational Cancer Research,* vol. 15, no. 2, p. 133, 2026.
[44] K. Ernawati, H. Hasyim, A. R. H. Utomo, D. Budiman, and D. Widiyanti, "Digital Exposome: A Digital Age Approach to Environmental Exposure and Cancer Risk Assessment," in *Cancer Exposomics and Environmental Influences on Carcinogenesis*: IGI Global Scientific Publishing, 2026, pp. 323-350.
[45] Z. U. Din, F. Akhtar, M. Y. Sufyan, and N. A. Sajid, "Risk factors and lifestyle factors in the development and prevention of cancer: A literature review," *Electronic Journal of Medical Research,* vol. 2, no. 1, pp. 13-25, 2026.
[46] K. Hua *et al.*, "Global Insight in Cancer Incidence, Mortality, and Disparities," *International Open Medical Journal (IOMJ),* pp. 32-38, 2026.
[47] Q. Zhu *et al.*, "Global disparities in healthcare resources and cancer burden: a population-based systematic analysis of 171 countries in 2022," *International Journal of Surgery,* vol. 111, no. 11, pp. 7549-7558, 2025.
[48] C. M. Balch *et al.*, "The global cancer crisis: a review of growing burden, deepening inequality and initiatives for prevention and early detection," 2026.
[49] R. Sankaranarayanan, "Screening for cancer in low-and middle-income countries," *Annals of global health,* vol. 80, no. 5, pp. 412-417, 2014.
[50] M. C. Castro, C. M. Turra, and J. Ponmattam, "Trends and Decomposition of Changes in Mortality in Low-and Middle-Income Countries, 1950–2019," *Population and Development Review,* vol. 51, no. 1, pp. 295-321, 2025.
[51] Y.-C. Fu, S.-B. Liang, M. Luo, and X.-P. Wang, "Intratumoral heterogeneity and drug resistance in cancer," *Cancer Cell Int.,* vol. 25, no. 1, p. 103, 2025.
[52] P. Gilson, J.-L. Merlin, and A. Harlé, "Deciphering tumour heterogeneity: from tissue to liquid biopsy," *Cancers (Basel),* vol. 14, no. 6, p. 1384, 2022.

[53] P. Bisoyi, "Malignant tumors–as cancer," in *Understanding Cancer*: Elsevier, 2022, pp. 21-36.
[54] R. Mundel, S. Dhadwal, S. Bharti, and M. Chatterjee, "A comprehensive overview of various cancer types and their progression," *Handbook of oncobiology: from basic to clinical sciences,* pp. 189-205, 2024.
[55] M. Chantoiseau, M. E. M. da Costa, B. Geoerger, N. Gaspar, and A. Marchais, "Fighting sarcomas at the root: The role of mesenchymal stem cells in sarcomagenesis," *Eur. J. Cancer,* p. 115628, 2025.
[56] M. Spalato-Ceruso, N. E. Ghazzi, and A. Italiano, "New strategies in soft tissue sarcoma treatment," *J. Hematol. Oncol.,* vol. 17, no. 1, p. 76, 2024.
[57] X. Wang *et al.*, "Advancements in diagnosis and treatment of cardiac sarcomas: a comprehensive review," *Curr. Treat. Options Oncol.,* vol. 26, no. 2, pp. 103-127, 2025.
[58] M. Biswas, "Pediatric Hematopathology: Bone Marrow Disorders, Leukemias, Lymphomas, and Molecular Diagnostics," *Birupaksha, Pediatric Hematopathology: Bone Marrow Disorders, Leukemias, Lymphomas, and Molecular Diagnostics (September 29, 2025). Biswas, B,* 2025.
[59] H.-S. Choi, B. S. Kim, S. Yoon, S.-O. Oh, and D. Lee, "Leukemic stem cells and hematological malignancies," *Int. J. Mol. Sci.,* vol. 25, no. 12, p. 6639, 2024.
[60] M. P. Mehta and R. Kotecha, "Central Nervous System Tumors: Overview," *Gunderson and Tepper's Clinical Radiation Oncology,* pp. 497-499. e1, 2026.
[61] B. Citgez, B. Yigit, and E. Capkinoglu, "A comprehensive review of de novo oligometastatic breast cancer: Current treatment options, surgical outcomes, and systemic therapy," *Northern Clinics of İstanbul,* vol. 13, no. 1.
[62] L. Pérez-Santiago, D. Huntley Pascual, J. S. Sánchez Lara, M. Huerta, and D. Dorcaratto, "How to Integrate Surgery into the Multidisciplinary Treatment of Liver-Only Metastatic Colorectal Cancer," *Cancers (Basel),* vol. 18, no. 3, p. 489, 2026.
[63] R. Weiser and Y. N. You, "Surgical Principles," in *Gunderson and Tepper's Clinical Radiation Oncology*: Elsevier, 2026, pp. 183-193. e3.
[64] J. Bray, W. Eward, and M. Breen, "Evaluating the relevance of surgical margins. Part one: The problems with current methodology," *Vet. Comp. Oncol.,* vol. 21, no. 1, pp. 1-11, 2023.
[65] F. J. Voskuil *et al.*, "Intraoperative imaging in pathology-assisted surgery," *Nature biomedical engineering,* vol. 6, no. 5, pp. 503-514, 2022.
[66] Z. Liu *et al.*, "Multi-stage mechanisms of tumor metastasis and therapeutic strategies," *Signal transduction and targeted therapy,* vol. 9, no. 1, p. 270, 2024.
[67] Y. Zhang *et al.*, "Thymoma and thymic carcinoma: surgical resection and multidisciplinary treatment," *Cancers (Basel),* vol. 15, no. 7, p. 1953, 2023.
[68] V. Fanotto *et al.*, "Primary tumor resection for metastatic colorectal, gastric and pancreatic cancer patients: In search of scientific evidence to inform clinical practice," *Cancers (Basel),* vol. 15, no. 3, p. 900, 2023.
[69] S. Ghanaati, S. E. Udeabor, A. Winter, R. Sader, and A. Heselich, "Cancer recurrence in operated primary oral squamous cell carcinoma patients seems to be independent of the currently available postoperative therapeutic approach: a retrospective clinical study," *Current oncology,* vol. 32, no. 4, p. 208, 2025.
[70] J. S. Vaidya, "Principles of cancer treatment by radiotherapy," *Surgery (Oxford),* vol. 42, no. 3, pp. 139-149, 2024.

[71] V. Valentini, L. Boldrini, S. Mariani, and M. Massaccesi, "Role of radiation oncology in modern multidisciplinary cancer treatment," *Mol. Oncol.,* vol. 14, no. 7, pp. 1431-1441, 2020.
[72] R. Baskar, K. A. Lee, R. Yeo, and K.-W. Yeoh, "Cancer and radiation therapy: current advances and future directions," *Int. J. Med. Sci.,* vol. 9, no. 3, p. 193, 2012.
[73] R. A. Chandra, F. K. Keane, F. E. Voncken, and C. R. Thomas, "Contemporary radiotherapy: present and future," *The Lancet,* vol. 398, no. 10295, pp. 171-184, 2021.
[74] H. Burstein *et al.*, "Tailoring treatment to cancer risk and patient preference: the 2025 St Gallen International Breast Cancer Consensus Statement on individualizing therapy for patients with early breast cancer," *Ann. Oncol.,* 2025.
[75] P. H. C. M. da Silva *et al.*, "Adjuvant radiotherapy for intermediate-risk early-stage cervical cancer post radical hysterectomy: a systematic review and meta-analysis," *Journal of clinical medicine,* vol. 14, no. 11, p. 4002, 2025.
[76] S. Kaur, P. Mayanglambam, D. Bajwan, and N. Thakur, "Chemotherapy and its adverse effects-A systematic review," *International Journal of Nursing Education and Research,* vol. 10, no. 4, pp. 399-402, 2022.
[77] K. Koper, S. Wileński, and A. Koper, "Advancements in cancer chemotherapy," *Physical Sciences Reviews,* vol. 8, no. 4, pp. 583-604, 2023.
[78] K. Nurgali, R. T. Jagoe, and R. Abalo, "Adverse effects of cancer chemotherapy: Anything new to improve tolerance and reduce sequelae?," vol. 9, ed: Frontiers Media SA, 2018, p. 245.
[79] W. R. Montor, A. R. O. S. E. Salas, and F. H. M. d. Melo, "Receptor tyrosine kinases and downstream pathways as druggable targets for cancer treatment: the current arsenal of inhibitors," *Mol. Cancer,* vol. 17, no. 1, p. 55, 2018.
[80] Y. Yang, S. Li, Y. Wang, Y. Zhao, and Q. Li, "Protein tyrosine kinase inhibitor resistance in malignant tumors: molecular mechanisms and future perspective," *Signal transduction and targeted therapy,* vol. 7, no. 1, p. 329, 2022.
[81] S. Srivastava *et al.*, "Revolutionizing immunotherapy: unveiling new horizons, confronting challenges, and navigating therapeutic frontiers in CAR-T Cell-Based gene therapies," *ImmunoTargets and Therapy,* pp. 413-433, 2024.
[82] A. R. Kumar, A. R. Devan, B. Nair, B. S. Vinod, and L. R. Nath, "Harnessing the immune system against cancer: current immunotherapy approaches and therapeutic targets," *Mol. Biol. Rep.,* vol. 48, no. 12, pp. 8075-8095, 2021.
[83] A. Haslam, J. Gill, and V. Prasad, "Estimation of the percentage of US patients with cancer who are eligible for immune checkpoint inhibitor drugs," *JAMA network Open,* vol. 3, no. 3, p. e200423, 2020.
[84] D.-R. Wang, X.-L. Wu, and Y.-L. Sun, "Therapeutic targets and biomarkers of tumor immunotherapy: response versus non-response," *Signal transduction and targeted therapy,* vol. 7, no. 1, p. 331, 2022.
[85] M. B. Lustberg, N. M. Kuderer, A. Desai, C. Bergerot, and G. H. Lyman, "Mitigating long-term and delayed adverse events associated with cancer treatment: implications for survivorship," *Nature Reviews Clinical Oncology,* vol. 20, no. 8, pp. 527-542, 2023.
[86] S. Ngo *et al.*, "Chronic sequelae of immune-related adverse events," *Expert Opin. Drug Saf.,* no. just-accepted, 2026.
[87] K. Gayathri, S. K. Karunya, P. Saranraj, M. K. D. Jothinathan, J. Arish, and A. M. Cardoso, "Immunotherapy and Targeted Molecular Therapies for Parkinson's Disease in Under-

Resourced Settings," in *Evolution and Innovation in Parkinson's Disease Therapies in Under-Resourced Settings*: IGI Global Scientific Publishing, 2026, pp. 141-174.
[88] S. M. Ahmed and B. A. Abdalla, "Update on glioblastoma: Biology, clinical management and emerging therapeutic strategies," *World Academy of Sciences Journal,* vol. 8, no. 2, pp. 1-8, 2026.
[89] H. Zhu *et al.*, "Global radiotherapy demands and corresponding radiotherapy-professional workforce requirements in 2022 and predicted to 2050: a population-based study," *The Lancet Global Health,* vol. 12, no. 12, pp. e1945-e1953, 2024.
[90] K. E. Lichter *et al.*, "Quantification of the environmental impact of radiotherapy and associated secondary human health effects: a multi-institutional retrospective analysis and simulation," *The Lancet Oncology,* vol. 25, no. 6, pp. 790-801, 2024.
[91] D. Schaue and W. H. McBride, "Opportunities and challenges of radiotherapy for treating cancer," *Nature reviews Clinical oncology,* vol. 12, no. 9, pp. 527-540, 2015.
[92] D. A. Jaffray, F. Knaul, M. Baumann, and M. Gospodarowicz, "Harnessing progress in radiotherapy for global cancer control," *Nature cancer,* vol. 4, no. 9, pp. 1228-1238, 2023.
[93] M. Abdel-Wahab *et al.*, "Radiotherapy and theranostics: a lancet oncology commission," *The lancet oncology,* vol. 25, no. 11, pp. e545-e580, 2024.
[94] T. A. Tali and F. Amin, *Comprehensive Care In Oncology*. BlueRose Publishers Pvt Ltd, 2026.
[95] W. Wei *et al.*, "Ionizing radiation: molecular mechanisms, biological effects, and therapeutic targets," *Molecular Biomedicine,* vol. 7, no. 1, p. 3, 2026.
[96] A. K. Parchur and P. Yadav, "Innovative approaches in precision radiation oncology," vol. 13, ed: Frontiers Media SA, 2026, p. 1776567.
[97] Y. Yan *et al.*, "Innovative approaches in precision radiation oncology: advanced imaging technologies and challenges which shape the future of radiation therapy," *Frontiers in Medicine,* vol. 12, p. 1686593, 2025.
[98] Y. Jiao, F. Cao, and H. Liu, "Radiation-induced cell death and its mechanisms," *Health Phys.,* vol. 123, no. 5, pp. 376-386, 2022.
[99] G. G. Dhakad, G. D. Patil, A. C. Nikum, and S. P. Shirsat, "Review on radiation therapy on cancer," *Research journal of Pharmacology and Pharmacodynamics,* vol. 14, no. 1, pp. 4-12, 2022.
[100] S. Z. Marković and M. D. Mojović, "Biological Effects of Ionizing Radiation," *Hospital Pharmacology: International Multidisciplinary Journal,* vol. 12, no. 1, 2025.
[101] A. H. Elgazzar, "Ionizing radiation: Biologic effects and essential cell and tissue biology," in *Synopsis of Pathophysiology in Nuclear Medicine*: Springer, 2023, pp. 9-36.
[102] M. Liu *et al.*, "Condensins regulate resection–dependent DNA double–strand break repair pathways in replicated chromatin," *Nucleic Acids Res.,* vol. 54, no. 4, p. gkag076, 2026.
[103] S. M. Gasser, "The Double Face of Base Excision Repair: Preventing and Triggering Double-Strand Breaks," *Bioessays,* vol. 48, no. 1, p. e70092, 2026.
[104] Y. Wang *et al.*, "Research progress on the role and mechanism of DNA damage repair in germ cell development," *Front. Endocrinol. (Lausanne),* vol. 14, p. 1234280, 2023.
[105] H. Kobayashi and S. Imanaka, "Mitochondrial DNA damage and its repair mechanisms in aging oocytes," *Int. J. Mol. Sci.,* vol. 25, no. 23, p. 13144, 2024.
[106] N. M. Vainshelbaum *et al.*, "Role of the circadian clock “death-loop” in the DNA damage response underpinning cancer treatment resistance," *Cells,* vol. 11, no. 5, p. 880, 2022.

[107] C. Ma and E. Gurkan-Cavusoglu, "A comprehensive review of computational cell cycle models in guiding cancer treatment strategies," *NPJ Systems Biology and Applications,* vol. 10, no. 1, p. 71, 2024.
[108] J. R. Hubenak, Q. Zhang, C. D. Branch, and S. J. Kronowitz, "Mechanisms of injury to normal tissue after radiotherapy: a review," *Plast. Reconstr. Surg.,* vol. 133, no. 1, pp. 49e-56e, 2014.
[109] M. Chen *et al.*, "The impact of overall treatment time on outcomes in radiation therapy for non-small cell lung cancer," *Lung Cancer,* vol. 28, no. 1, pp. 11-19, 2000.
[110] M.-C. Vozenin, J. Bourhis, and M. Durante, "Towards clinical translation of FLASH radiotherapy," *Nature Reviews Clinical Oncology,* vol. 19, no. 12, pp. 791-803, 2022.
[111] M. Webster *et al.*, "New approaches in radiotherapy," *Cancers (Basel),* vol. 17, no. 12, p. 1980, 2025.
[112] F. De Benetti, "Image Analysis for Personalized Cancer Diagnosis and Radiation Therapy using Anatomy, Physiology, and Physics," Technische Universität München, 2025.
[113] K. C. Ohaegbulam and M. Heard, "The Shaping of Contemporary Radiation Oncology (2005–2015): A Focus on Clinical Practice and Technological Advancements," *125 Beams and the Rise of Radiation Therapy: The People, Landmark Discoveries, and Innovations that Shaped a Field,* pp. 159-176, 2026.
[114] C. Algranati, "Technological advances in external beam radiotherapy. Study of new treatment strategies," 2025.
[115] V. Sundaram, D. Khanna, and M. Palanisamy, "Evaluation of dose rate and gantry speed variations in volumetric modulated Arc therapy optimization algorithms for a modern linear accelerator," *Radiological Physics and Technology,* pp. 1-16, 2026.
[116] A. C. Kraan and A. Del Guerra, "Technological developments and future perspectives in particle therapy: A topical review," *IEEE Transactions on Radiation and Plasma Medical Sciences,* vol. 8, no. 5, pp. 453-481, 2024.
[117] A. J. Deisher, J. E. Johnson, and M. G. Herman, "Radiation Physics: Charged Particle Therapy," in *Gunderson and Tepper's Clinical Radiation Oncology*: Elsevier, 2026, pp. 157-167. e3.
[118] L. J. Verhey, "Immobilizing and positioning patients for radiotherapy," in *Seminars in radiation oncology*, 1995, vol. 5, no. 2: Elsevier, pp. 100-114.
[119] M. Sonier, "Adaptive radiotherapy treatment corrections to account for patient-specific systematic soft tissue deformations: prostate, lung, and head and neck cancer," University of British Columbia, 2021.
[120] I. Vergalasova and J. Cai, "A modern review of the uncertainties in volumetric imaging of respiratory-induced target motion in lung radiotherapy," *Med. Phys.,* vol. 47, no. 10, pp. e988-e1008, 2020.
[121] L. A. Dawson and M. B. Sharpe, "Image-guided radiotherapy: rationale, benefits, and limitations," *The lancet oncology,* vol. 7, no. 10, pp. 848-858, 2006.
[122] J. De Los Santos *et al.*, "Image guided radiation therapy (IGRT) technologies for radiation therapy localization and delivery," *International Journal of Radiation Oncology* Biology* Physics,* vol. 87, no. 1, pp. 33-45, 2013.
[123] S. Wang, O. P. Serrano, Y. Chen, S. Ye, Q. Wei, and L. Xing, "Image-guided radiation therapy (IGRT) of cancer," in *Cancer Theranostics, Second Edition*: Elsevier, 2026, pp. 223-248.
[124] P. Wohlfahrt and S. Schellhammer, "In-Room Systems for Patient Positioning," *Image-Guided High-Precision Radiotherapy,* p. 91, 2022.

[125] J. Buckley *et al.*, "Anatomical deformation due to horizontal rotation: towards gantry-free radiation therapy," *Phys. Med. Biol.,* vol. 64, no. 17, p. 175014, 2019.
[126] D. J. Hawkes *et al.*, "Tissue deformation and shape models in image-guided interventions: a discussion paper," *Med. Image Anal.,* vol. 9, no. 2, pp. 163-175, 2005.
[127] J. Talapko *et al.*, "Health effects of ionizing radiation on the human body," *Medicina,* vol. 60, no. 4, p. 653, 2024.
[128] R. K. Ahirwar and A. K. Meena, *Applied Physiology*. Academic Guru Publishing House, 2025.
[129] Y. Wu *et al.*, "Current research status of respiratory motion for thorax and abdominal treatment: a systematic review," *Biomimetics,* vol. 9, no. 3, p. 170, 2024.
[130] S. Jiang, Y. Yang, S. Gu, J. Li, and Y. Hou, "Bridge geometric shape measurement using LiDAR–camera fusion mapping and learning-based segmentation method," *Buildings,* vol. 15, no. 9, p. 1458, 2025.
[131] A. Lagudi, U. Severino, L. Barbieri, and F. Bruno, "A Practical Methodology for Accuracy and Quality Evaluation of Structured Light Systems in Automotive Inspection," *Machines,* vol. 13, no. 7, p. 576, 2025.
[132] L. Boldrini *et al.*, "MRI-guided stereotactic body radiation therapy for very elderly patients with primary lung cancer: a retrospective analysis of safety and efficacy profiles," *Radiol. Med.,* vol. 130, no. 10, pp. 1625-1632, 2025.
[133] S. Taylor *et al.*, "Image guidance and interfractional anatomical variation in paediatric abdominal radiotherapy," *Br J Radiol,* vol. 96, no. 1146, p. 20230058, 2023.
[134] J. Wulff, K. Zink, and I. Kawrakow, "Efficiency improvements for ion chamber calculations in high energy photon beams," *Med. Phys.,* vol. 35, no. 4, pp. 1328-1336, 2008.
[135] D. P. Fontenla, R. Yaparpalvi, C.-S. Chui, and E. Briot, "The use of diode dosimetry in quality improvement of patient care in radiation therapy," *Med. Dosim.,* vol. 21, no. 4, pp. 235-241, 1996.
[136] S. G. Ju, Y. C. Ahn, S. J. Huh, and I. J. Yeo, "Film dosimetry for intensity modulated radiation therapy: dosimetric evaluation," *Med. Phys.,* vol. 29, no. 3, pp. 351-355, 2002.
[137] P. Alvarez, S. Kry, F. Stingo, and D. Followill, "TLD and OSLD dosimetry systems for remote audits of radiotherapy external beam calibration," *Radiation measurements,* vol. 106, pp. 412-415, 2017.
[138] J. Takatsu *et al.*, "Appropriate Frequency of EPID Calibrations to Ensure the Dosimetric Accuracy of EPID-based Pretreatment Quality Assurance," *Radiation Physics and Chemistry,* p. 113570, 2025.
[139] I. Oraiqat *et al.*, "An ionizing radiation acoustic imaging (iRAI) technique for real-time dosimetric measurements for FLASH radiotherapy," *Med. Phys.,* vol. 47, no. 10, pp. 5090-5101, 2020.
[140] S. Hickling, P. Léger, and I. El Naqa, "Simulation and experimental detection of radiation-induced acoustic waves from a radiotherapy linear accelerator," in *2014 IEEE International Ultrasonics Symposium*, 2014: IEEE, pp. 29-32.
[141] N. H. Ba Sunbul *et al.*, "A simulation study of ionizing radiation acoustic imaging (iRAI) as a real-time dosimetric technique for ultra-high dose rate radiotherapy (UHDR-RT)," *Med. Phys.,* vol. 48, no. 10, pp. 6137-6151, 2021.
[142] H. Lei *et al.*, "Toward in vivo dosimetry in external beam radiotherapy using x-ray acoustic computed tomography: a soft-tissue phantom study validation," *Med. Phys.,* vol. 45, no. 9, pp. 4191-4200, 2018.

[143] L. CarsonPaul and E. NaqaIssam, "Dual-modality X-ray-induced radiation acoustic and ultrasound imaging for real-time monitoring of radiotherapy," *BME frontiers,* 2020.
[144] W. Zhang *et al.*, "Real-time, volumetric imaging of radiation dose delivery deep into the liver during cancer treatment," *Nat. Biotechnol.,* vol. 41, no. 8, pp. 1160-1167, 2023.
[145] K. C. Cuneo *et al.*, "Clinical pilot study of ionizing radiation acoustic imaging (iRAI) for real-time visualization of radiation therapy dose delivery in cancer patients," *International Journal of Radiation Oncology* Biology* Physics,* 2025.
[146] L. Petagna *et al.*, "Pathophysiology of Crohn's disease inflammation and recurrence," *Biol. Direct,* vol. 15, no. 1, p. 23, 2020.
[147] G. Pasternak *et al.*, "Crohn's disease: basic characteristics of the disease, diagnostic methods, the role of biomarkers, and analysis of metalloproteinases: a review," *Life,* vol. 13, no. 10, p. 2062, 2023.
[148] M. Imbrizi *et al.*, "A Developmental Perspective on the Intestinal Microbiota in Crohn's Disease," *Int. J. Mol. Sci.,* vol. 27, no. 5, p. 2144, 2026.
[149] R. Sferra, A. Vetuschi, G. Latella, A. Cappariello, and S. Pompili, "Inflammatory bowel disease and extracellular matrix: when victim becomes double agent," *Inflamm. Res.,* vol. 75, no. 1, p. 61, 2026.
[150] D. Penninck[1] and M.-A. d'Anjou, "Gastrointestinal tract," *Atlas of small animal ultrasonography,* p. 259, 2015.
[151] R. Yantiss and R. Odze, "Diagnostic difficulties in inflammatory bowel disease pathology," *Histopathology,* vol. 48, no. 2, pp. 116-132, 2006.
[152] G. G. Kaplan, "The global burden of inflammatory bowel disease: from 2025 to 2045," *Nature Reviews Gastroenterology & Hepatology,* vol. 22, no. 10, pp. 708-720, 2025.
[153] B. Veauthier and J. R. Hornecker, "Crohn's disease: diagnosis and management," *Am. Fam. Physician,* vol. 98, no. 11, pp. 661-669, 2018.
[154] I. S. Al-Dabbagh, "Comprehensive Insight into Crohn's Disease: Diagnosis, Clinical Presentation, Complications and Treatment"," *Journal of the College of Basic Education,* vol. 1, no. وقائع المؤتمر العلمي لكلية التربية الأسا, pp. 65-82, 2025.
[155] R. K. Mowlah and J. Soldera, "Risk and management of post-operative infectious complications in inflammatory bowel disease: A systematic review," *World J. Gastrointest. Surg.,* vol. 15, no. 11, p. 2579, 2023.
[156] F. Rieder and C. Fiocchi, "Mechanisms of tissue remodeling in inflammatory bowel disease," *Dig. Dis.,* vol. 31, no. 2, pp. 186-193, 2013.
[157] J. M. Park, J. Kim, Y. J. Lee, S. U. Bae, and H. W. Lee, "Inflammatory bowel disease–associated intestinal fibrosis," *Journal of pathology and Translational Medicine,* vol. 57, no. 1, pp. 60-66, 2023.
[158] F. Rieder and C. Fiocchi, "Intestinal fibrosis in IBD—a dynamic, multifactorial process," *Nature reviews Gastroenterology & hepatology,* vol. 6, no. 4, pp. 228-235, 2009.
[159] F. Rieder and C. Fiocchi, "Intestinal fibrosis in inflammatory bowel disease—Current knowledge and future perspectives," *Journal of Crohn's and Colitis,* vol. 2, no. 4, pp. 279-290, 2008.
[160] M. Iacucci, G. Santacroce, M. Yasuharu, and S. Ghosh, "Artificial intelligence–driven personalized medicine: transforming clinical practice in inflammatory bowel disease," *Gastroenterology,* 2025.
[161] I. Kremenevski, O. Sander, M. Sticherling, and M. Raithel, "Paradoxical reactions to biologicals in chronic inflammatory systemic diseases," *Deutsches Ärzteblatt International,* vol. 119, no. 6, p. 88, 2022.

[162] N. K. Klemm and J. D. Feuerstein, "A practical guide to dilating inflammatory bowel disease strictures," *Expert Rev. Gastroenterol. Hepatol.,* vol. 19, no. 4, pp. 377-387, 2025.
[163] F. Rieder, E. M. Zimmermann, F. H. Remzi, and W. J. Sandborn, "Crohn's disease complicated by strictures: a systematic review," *Gut,* vol. 62, no. 7, pp. 1072-1084, 2013.
[164] J. Burisch and P. Munkholm, "The epidemiology of inflammatory bowel disease," *Scand. J. Gastroenterol.,* vol. 50, no. 8, pp. 942-951, 2015.
[165] J. H. Yoo, S. Holubar, and F. Rieder, "Fibrostenotic strictures in Crohn's disease," *Intestinal research,* vol. 18, no. 4, pp. 379-401, 2020.
[166] S. Kumar *et al.*, "Diagnostic performance of sonographic activity scores for adult terminal ileal Crohn's disease compared to magnetic resonance and histological reference standards: experience from the METRIC trial," *Eur. Radiol.,* vol. 34, no. 1, pp. 455-464, 2024.
[167] S. M. Hong and D. H. Baek, "Diagnostic procedures for inflammatory bowel disease: laboratory, endoscopy, pathology, imaging, and beyond," *Diagnostics,* vol. 14, no. 13, p. 1384, 2024.
[168] E. Eggermont *et al.*, "Ulcerative colitis: moving beyond the mucosal dogma," *The Lancet Gastroenterology & Hepatology,* vol. 11, no. 2, pp. 163-174, 2026.
[169] J. Alfredsson, C. S. Wallem, M. Östling, H. de la Croix, E. Bexe-Lindskog, and M. J. Wick, "Tissue layer-resolved proteome landscape of Crohn's disease strictures highlights potential drivers of fibrosis progression," *JCI insight,* 2026.
[170] A. Athanasakos *et al.*, "Inflammatory bowel disease—the role of cross-sectional imaging techniques in the investigation of the small bowel," *Insights into Imaging,* vol. 6, no. 1, pp. 73-83, 2015.
[171] D. Bettenworth *et al.*, "Assessment of Crohn's disease-associated small bowel strictures and fibrosis on cross-sectional imaging: a systematic review," *Gut,* vol. 68, no. 6, pp. 1115-1126, 2019.
[172] M. Fraquelli *et al.*, "Role of US in detection of Crohn disease: meta-analysis," *Radiology,* vol. 236, no. 1, pp. 95-101, 2005.
[173] J. Rimola *et al.*, "Magnetic resonance for assessment of disease activity and severity in ileocolonic Crohn's disease," *Gut,* vol. 58, no. 8, pp. 1113-1120, 2009.
[174] L. Lin and L. V. Wang, "Photoacoustic imaging," in *Optical Imaging in Human Disease and Biological Research*: Springer, 2021, pp. 147-175.
[175] P. Beard, "Biomedical photoacoustic imaging," *Interface focus,* vol. 1, no. 4, pp. 602-631, 2011.
[176] Y. Zhu *et al.*, "Identifying intestinal fibrosis and inflammation by spectroscopic photoacoustic imaging: an animal study in vivo," *Biomedical optics express,* vol. 9, no. 4, pp. 1590-1600, 2018.
[177] H. Lei *et al.*, "Characterizing intestinal strictures of Crohn's disease in vivo by endoscopic photoacoustic imaging," *Biomedical optics express,* vol. 10, no. 5, pp. 2542-2555, 2019.
[178] Y. Zhu *et al.*, "Prototype endoscopic photoacoustic-ultrasound balloon catheter for characterizing intestinal obstruction," *Biomedical optics express,* vol. 13, no. 6, pp. 3355-3365, 2022.
[179] E. R. Cohen, "An introduction to error analysis: The study of uncertainties in physical measurements," *Measurement Science and Technology,* vol. 9, no. 6, p. 022, 1998.
[180] H. Kim and J. Jeong, "Non-contact measurement of human respiration and heartbeat using W-band Doppler radar sensor," *Sensors,* vol. 20, no. 18, p. 5209, 2020.

[181] D. Brunet, E. R. Vrscay, and Z. Wang, "On the mathematical properties of the structural similarity index," *IEEE Transactions on Image Processing,* vol. 21, no. 4, pp. 1488-1499, 2011.
[182] M. Hussein, P. Rowshanfarzad, M. A. Ebert, A. Nisbet, and C. H. Clark, "A comparison of the gamma index analysis in various commercial IMRT/VMAT QA systems," *Radiother. Oncol.,* vol. 109, no. 3, pp. 370-376, 2013.
[183] G. R. Harris *et al.*, "Hydrophone measurements for biomedical ultrasound applications: A review," *IEEE transactions on ultrasonics, ferroelectrics, and frequency control,* vol. 70, no. 2, pp. 85-100, 2022.
[184] L. Zhao, L. Tang, Y. Liu, Z. Sun, Q. Liu, and C. Bi, "Passive directivity detection of acoustic sources based on acoustic Luneburg lens," *The Journal of the Acoustical Society of America,* vol. 154, no. 2, pp. 594-601, 2023.
[185] K. K. Shung, M. Smith, and B. M. Tsui, *Principles of medical imaging*. Academic Press, 2012.
[186] T. L. Szabo, *Diagnostic ultrasound imaging: inside out*. Academic press, 2013.
[187] C.-W. Cheng and I. J. Das, "Treatment plan evaluation using dose–volume histogram (DVH) and spatial dose–volume histogram (zDVH)," *International Journal of Radiation Oncology* Biology* Physics,* vol. 43, no. 5, pp. 1143-1150, 1999.
[188] R. Drzymala *et al.*, "Dose-volume histograms," *International Journal of Radiation Oncology* Biology* Physics,* vol. 21, no. 1, pp. 71-78, 1991.
[189] T. Hirasawa *et al.*, "Spectral-differential-based unmixing for multispectral photoacoustic imaging," *Applied Optics,* vol. 57, no. 10, pp. 2383-2393, 2018.
[190] S. Tzoumas and V. Ntziachristos, "Spectral unmixing techniques for optoacoustic imaging of tissue pathophysiology," *Philosophical Transactions of the Royal Society A: Mathematical, Physical and Engineering Sciences,* vol. 375, no. 2107, 2017.
[191] F. Asgharzadeh, R. Bargi, M. Hosseini, M. Farzadnia, and M. Khazaei, "Cardiac and renal fibrosis and oxidative stress balance in lipopolysaccharide-induced inflammation in male rats," *ARYA atherosclerosis,* vol. 14, no. 2, p. 71, 2018.
[192] H. Murakami, "The power of the modified Wilcoxon rank-sum test for the one-sided alternative," *Statistics,* vol. 49, no. 4, pp. 781-794, 2015.
[193] J. C. Bamber, "Ultrasonic properties of tissues," in *Ultrasound in medicine*: CRC Press, 2020, pp. 57-88.
[194] J. Bamber, "Attenuation and absorption," *Physical principles of medical ultrasonics,* vol. 2, pp. 93-166, 1986.